Unsteady Response of a Two-Dimensional Hydrofoil Subject to High Reduced Frequency Gust Loading

by

Elizabeth Ann Horwich
A.B. Dartmouth College (1991)

Submitted to the Department of Ocean Engineering
and the Department of Aeronautics and Astronautics
in partial fulfillment of the requirements for the degrees of

Master of Science in Ocean Engineering
Master of Science in Aeronautics and Astronautics

at the

MASSACHUSETTS INSTITUTE OF TECHNOLOGY

June 1993

Author ....
Department of Ocean Engineering
May 14, 1993

Certified by ....
Justin E. Kerwin
Professor of Naval Architecture
Thesis Supervisor

Read by ....
Eugene E. Covert
Professor of Aeronautics and Astronautics
Thesis Reader

Accepted by ....
Professor A. Douglas Carmichael
Chairman, Committee on Graduate Students
Department of Ocean Engineering

Accepted by ....
Professor Harold Y. Wachman
Chairman, Committee on Graduate Students
Department of Aeronautics and Astronautics

Unsteady Response of a Two-Dimensional Hydrofoil Subject to High Reduced Frequency Gust Loading

by

Elizabeth Ann Horwich

Submitted to the Department of Ocean Engineering
on May 7, 1993, in partial fulfillment of the
requirements for the degrees of
Master of Science in Ocean Engineering
and
Master of Science in Aeronautics and Astronautics

Abstract

Marine propeller blades are subject to a time-varying velocity as they pass through the wake of the ship; the inflow is a convected wave that imposes gust loading on the blade. Experiments have been conducted at the MIT Variable Pressure Water Tunnel to determine the boundary layer and surface pressure response of an isolated two-dimensional hydrofoil subject to steady loading and to transverse gust loading at high reduced frequencies. The results of this and future experiments will be used to provide a basis for modifying the classical Kutta condition used in unsteady potential flow models, and will provide a database for validation of boundary-element method and Navier-Stokes computational fluid dynamic codes.

Steady flow measurements at $Re = 1.36 \times 10^6$ and $Re = 3.78 \times 10^6$ reveal well developed boundary layers over the hydrofoil, with flow separation within the last 5% of the chord on the suction side. Unsteady flow measurements at $Re = 3.78 \times 10^6$ and reduced frequency $k = 3.6$ detail the structure of the gust velocity through the boundary layer. Considerable phase shifting occurs over the boundary layer thickness; on the suction side, a phase reversal occurs at positions near the trailing edge. The standard deviation of velocity also contains time dependence in some regions of the dowstream boundary layers.

Surface pressure measurements at $Re = 3.78 \times 10^6$ and reduced frequency $k = 3.6$ record the existence of large harmonic components over the chord. A survey of surface pressure response at fixed reduced frequency, varying pitching frequency and freestream speed, suggests that the source of the higher harmonics is mechanical and not hydrodynamic. Further investigations of this are recommended.

Thesis Supervisor: Justin E. Kerwin
Title: Professor of Naval Architecture

Acknowledgments

The experimental results presented in this thesis are the products of a large group effort: a large effort by a large group of extremely talented people. I feel very lucky to have participated in such an exciting study, and am grateful to those who guided my work. Professor Justin Kerwin and Dr. David Keenan developed and implemented the original concept; their expertise has been invaluable. Dr. Charles Mazel provided considerable skill in the development of the software and hardware for data collection. Special thanks go to Mr. Matthew Knapp for his dedication and for his sense of humor, which made the most trying circumstances enjoyable. I am also grateful to Professor Eugene Covert for his encouragement and advice.

This project is supported by the Office of Naval Research contract number N00014-89-J-3194, monitored by Dr. James Fein. My studies at MIT have been funded by the Office of Naval Research Graduate Fellowship Program, administered by the American Society for Engineering Education.

Contents

List of Figures

List of Tables

Chapter 1

Introduction

1.1 Purpose

The purpose of this research is to provide highly detailed flow field measurements around an isolated two-dimensional hydrofoil section subject to steady loading and unsteady vertical gust loading at high reduced frequencies. The results of this experiment will be used to provide a basis for examining the classical Kutta condition to determine if modification is needed for use in unsteady potential flow models. Furthermore, experimental results will provide a database for validation of boundary-element method and Navier-Stokes computational fluid dynamics codes. This portion of the research covers the results of the steady flow investigation at two Reynolds numbers and the results of the unsteady flow investigation at one Reynolds number, reduced frequency combination.

1.2 Background

The most basic and well-developed tools for analysis of fluid flows over complex surfaces are two-dimensional inviscid methods. When viscous effects are confined to a thin shear layer, the bulk of the fluid is essentially inviscid. Rather than solve the fully nonlinear Navier-Stokes equations with a no-slip boundary condition on the body, instead we neglect the viscous effects in the shear layer and reduce the system of nonlinear partial differential equations to Euler's equation. Moreover, if the fluid domain is incompressible and irrotational we can write the velocity vector as the gradient of a potential, and the continuity equation becomes Laplace's equation, a linear partial differential equation. The mathematical simplifications are considerable. We then solve Laplace's equation with a flow-tangency boundary condition, later correcting the potential flow solution for the effects of viscosity.

Solving Laplace's equation for a steady flow field about a lifting surface with only the condition of flow-tangency on the body surface gives a nonphysical result: the fluid velocity at the trailing edge is infinite. In reality the fluid leaves the trailing edge smoothly. If we posit this as a new condition on the flow field, then another variable must be introduced: the circulation of the hydrofoil. The addition of a new variable requires a new boundary condition for the system of equations to be well-posed. In order to find the magnitude of the circulation for steady flow over a lifting surface with a sharp trailing edge, the so-called Kutta condition is well established: just enough circulation is present so that the velocity at the trailing edge is finite. In steady flow this is equivalent to requiring that, at the trailing edge, the pressure is continuous, that is, the loading tends to zero; that the shedding of vorticity tends to zero; and that the stagnation streamline emanating from the trailing edge bisects the wedge angle of the foil. In any of these forms, the Kutta condition is sufficient to determine the unique solution for the circulation.

It must be kept in mind that the assumption of smooth tangential flow at the trailing edge is a mathematical imposition on the problem. This assumption effectively removes the effects of viscosity from the problem; although in the unsteady start-up phase the action of viscosity is important, once the steady-state motion has been reached, viscosity can be explicitly ignored but implicitly incorporated into a single condition. But in real life small amounts of curvature at the trailing edge do not affect the physical fact that in steady flow the stagnation streamline bisects the wedge angle. And certainly for a well-rounded trailing edge viscous effects cannot be neglected in this way; the location of the rear stagnation point and thus the circulation is indeterminate and cannot be found without considering the action of viscosity.

For unsteady flow, the problem of imposing a closure condition at the trailing edge is complicated further. For attached flow the stagnation point is still located at the trailing edge, but the changes in bound vorticity require an equal and opposite shedding of free vorticity, thus violating the equivalent conditions of no shed vorticity and stagnation streamline bisection of the wedge angle. But since a free vortex sheet cannot sustain a load across it, the classical Kutta condition can be formulated in the unsteady case as a condition of zero load at the trailing edge. Again, this is only valid if there is weak viscous-inviscid interaction.

Many experiments have been set up to study unsteady loading on an airfoil, yet no consistent patterns emerges; indeed, even at low amplitudes and frequencies the Kutta condition has not been adequately validated. Measurements of surface pressures as the trailing edge is approached do show a tendency to zero loading, but the agreement of measured phase with theoretical analyses is poor. In some experiments, the condition of zero loading seems to be applicable over a viscous region around the trailing edge and not necessarily at the trailing edge itself. Although unsteady loading variations in the trailing edge region may not significantly affect the magnitude of the unsteady lift, the unsteady moment may be significantly altered. Also, phase lag variations in this region are particularly important with regard to noise generation. Hence the proper theoretical modelling of the time-variant trailing edge condition is an important task.

If viscous effects are considerable, often the shear layers can be modelled as a region separate from the inviscid flow; the shear layer solution is used to modify the inviscid solution and vice versa until a converged solution is obtained. The numerical scheme, known as an interacting viscid/inviscous solver, is computationally inexpensive compared to trying to solve the full Navier-Stokes equations. But these solvers are generally formulated for a few specific applications such as steady flow in diffusers, over foils, and so forth. If a solution is desired for any flow regime over any surface geometry, one must solve the fully nonlinear Navier-Stokes equations, a task that requires several orders of magnitude higher computational cost than inviscid or interacting viscous/inviscid schemes. Furthermore, as the Kutta condition is necessary to determine a unique solution to the inviscid fluid flow equations, a turbulence model for the Reynolds stresses is required to solve the Navier-Stokes equations. At present this is the main source of inaccuracy in Navier-Stokes solvers.

1.3 Theory

1.3.1 Important Parameters in Unsteady Viscous Flows

Experimental studies are characterized by physical parameters that define the situation at hand. The measure of inertial to viscous effects is the Reynolds number based on chord length,

$$Re = \frac{U\,c}{\nu}$$

where c is the chord length, U is the freestream velocity, and ν is the kinematic viscosity of the fluid. In potential flow theory, in the limit as viscosity is vanishingly small, the Reynolds number is infinite. In reality the character of the shear layer depends on the Reynolds number. External flows over aircraft wings, ships, automobiles, and so forth generally have Reynolds numbers in the millions and higher.

A measure of the relative unsteadiness of a flow is the reduced frequency. The reduced frequency is the ratio of the rate of convection to the rate of oscillation,

$$k = \frac{\omega\,c}{2\,U}$$

where $c/2$ is the semi-chord, ω is the frequency of oscillation, and U is the freestream velocity. If we consider a wave of wavelength λ being convected with the freestream, then

$$k = \frac{2\,\pi\,f\,c}{2\,\lambda\,f} = \frac{\pi}{\lambda}\,c$$

So the reduced frequency is also a measure of how many waves are present over the chord at any given time; if $k = \pi$, then exactly one wave acts on the airfoil. It is apparent that a low reduced frequency corresponds to long waves and quasi-steady flow and that a high reduced frequency corresponds to short waves and acoustic phenomena.

Other parameters of interest concern the geometry of the airofil. Thin airfoil theory requires that the ratios of camber to chord and thickness to chord, and the angle of attack (in radians) of the airfoil are small, that is, much less than one. Furthermore, the ratio of the gust magnitude to the freestream velocity must also be small. In order for the viscous layers to remain attached to the foil surface, these criteria also hold.

1.3.2 Features of Potential Flow

The Navier-Stokes equations fully describe the motion of any fluid flow around a body. But these nonlinear partial differential equations are very difficult to solve, except in a few very simple situations. When viscous effects are confined to a thin shear layer adjacent to the body, the rest of the fluid is essentially inviscid. Furthermore, if the fluid domain is irrotational then we can write the velocity vector as the gradient of a potential, and the continuity equation becomes Laplace's equation, a linear partial differential equation:

$$\vec{V} = \nabla\phi \Rightarrow \nabla \cdot \vec{V} = \nabla \cdot \nabla\phi = \nabla^2\phi = 0 \tag{1.1}$$

One thing to note about Laplace's equation is that it is not explicitly time-dependent; the time dependence is incorporated into the boundary conditions and not the equation itself. The velocity potential ϕ and the velocity $\vec{V}$ are uniquely determined by the instantaneous boundary conditions, that is, the velocity responds instantaneously to any change in the boundary conditions: there is no time lag in reaching equilibrium.

This is not true for the pressure distribution, and hence the forces and moments acting on the body. Upon the assumptions of ideal, irrotational flow, the momentum equations can be integrated to become the Bernoulli equation [13, p. 71-72]:

$$\frac{p}{\rho} + \frac{1}{2}|\nabla\phi|^2 + \frac{\partial\phi}{\partial t} = F(t) \tag{1.2}$$

Thus in order to determine the forces and moments acting on a body in an unsteady potential flow field, one must be able to predict both the magnitude and the time dependence of the pressure distribution.

1.3.3 The Gust Problem

Linearized two-dimensional airfoil theory consists of solving Laplace's equation for a perturbation velocity field induced by the airfoil, $\nabla\phi = (u, v)$ which satisfies certain requirements. The perturbation potential must vanish far away from the airfoil, i.e., at infinity. Boundary conditions include a kinematic boundary condition on the foil surface, a suitable Kutta condition at the trailing edge, and a dynamic boundary condition on the vortex wake. Linearized airfoil theory requires that the slope of the foil surface be sufficiently small that the foil surface and the wake can be taken to lie along a straight line. Thus the kinematic boundary condition is applied along a cut of chord length aligned with the x axis and the dynamic boundary conditon is applied downstream of the cut and also along the x axis. Furthermore, in order to use linearized theory, the magnitude of the unsteady velocity must be small relative to the freestream velocity.

Consider[1] a stationary thin airfoil located in the xz plane on the x axis and encountering a region of vertical velocity described by $W(x, z = 0, t) = Re\{W_0\, e^{i(\omega t - kx)}\}$, where k is the reduced frequency; the gust is being convected with the freestream velocity U. If $w_s(x, t)$ is the vertical coordinate of the foil surface, and the total velocity potential is $\nabla\Phi = (u + U, w + W)$ then the kinematic boundary condition requires that

$$\begin{aligned} \frac{D(z - z_s)}{Dt} &= \frac{\partial(z - z_s)}{\partial t} + (u + U)\frac{\partial(z - z_s)}{\partial x} + (w + W)\frac{\partial(z - z_s)}{\partial z} \\ &= -(u + U)\frac{\partial z_s}{\partial x} + w + W \\ &= 0 \end{aligned} \tag{1.3}$$

If we apply this on the linearized foil surface, i.e., at z = 0, and remove second-order

---

[1] The following is a condensed version of presentations found in Newman, J.N. [10, p.220-230], and Bisplinghoff, R.L., Ashley, H., and Halfman, R.L. [1, p.251-293].

terms, then the vertical velocity on the airfoil is

$$w(x,0,t) \;=\; -U\frac{\partial z_s}{\partial x} - W(x,0,t) \tag{1.4}$$

The horizontal velocity components on the upper and lower sides of the vortex sheet are represented by a bound vortex sheet on the x-axis, given by $u(x,0^{\pm},t) = \mp\gamma(x,t)$.

Next consider the dynamic boundary condition on the wake. The linearized pressure in the fluid is obtained from Bernoulli's equation,

$$p - p_{\infty} \;=\; -\rho\left(\frac{\partial\phi}{\partial t} - u\,U\right) \tag{1.5}$$

The difference between the pressure above and below the wake must be zero since the wake cannot sustain a force,

$$\Delta p = p^{+} - p^{-} = -\rho\left[\frac{\partial\phi^{+}}{\partial t} - \frac{\partial\phi^{-}}{\partial t} - U\left(u^{+} - u^{-}\right)\right] = 0 \tag{1.6}$$

Differentiating this with respect to x and substituting in $u(x,0^{\pm},t) = \mp\gamma(x,t)$, we find that

$$\frac{\partial\gamma(x,t)}{\partial t} - U\frac{\partial\gamma(x,t)}{\partial x} = 0 \tag{1.7}$$

the general solution of which is

$$\gamma(x,t) = \gamma(x - Ut) \tag{1.8}$$

Thus the vorticity in the wake is convected with the freestream velocity.

Now consider the flow right at the trailing edge. From Kelvin's theorem, the wake vortex element shed from the trailing edge during a small time interval dt has a circulation equal and opposite to the corresponding change in airfoil circulation:

$$\gamma_w(x_{TE},t)\,dx \;=\; -\frac{d\Gamma}{dt}dt \tag{1.9}$$

Since the fluid moves with speed U then $dx = U dt$ and

$$U\gamma_w(x_{TE}, t) \; = \; -\frac{d\Gamma}{dt} \tag{1.10}$$

This relates the vorticity shed at the trailing edge to the rate of change of Γ. Further in the wake, a vortex element at a point x was shed previously, at a time $\frac{x-x_{TE}}{U}$ earlier. Thus,

$$U\gamma_w(x, t + \frac{x - x_{TE}}{U}) \; = \; -\frac{d\Gamma}{dt} \tag{1.11}$$

The rate of change in airfoil circulation is cast into the wake at the trailing edge and is convected downstream.

Using the kinematic boundary condition (eqn 1.4), the dynamic boundary condition (1.6), and a suitable Kutta condition at the trailing edge to remove the analytic square-root singularity, one can solve for the forces and moments on a two-dimensional airfoil subject to a vertical gust described by $W(x, 0, t) = W_0 \, e^{i\omega t}$. In 1941 W.R. Sears solved this problem by writing the vertical gust velocity as a series of Bessel functions of the first kind in the transformed coordinate $x = \frac{c}{2} \, cos(\theta)$ [17]. He found the unsteady lift to be equal to the steady lift at an effective gust angle of attack multiplied by a complex function S(k), appropriately called the Sears function (figure 1-1):

$$C_L(t) = 2\,\pi \; Re \; \left[\alpha_0 \, e^{i\omega t} \, S(k)\right] \tag{1.12}$$

$$where \;\; S(k) = \frac{2\,i/\pi\,k}{H_1^{(2)}(k) \, + \, iH_0^{(2)}(k)} \tag{1.13}$$

$$and \;\; \alpha_0 \; = \; \frac{W_0}{U} \tag{1.14}$$

At each instantaneous angle of attack, the unsteady lift is less than the steady lift would be at the same angle of attack; also, there is a phase lag between the lift and the angle of attack.

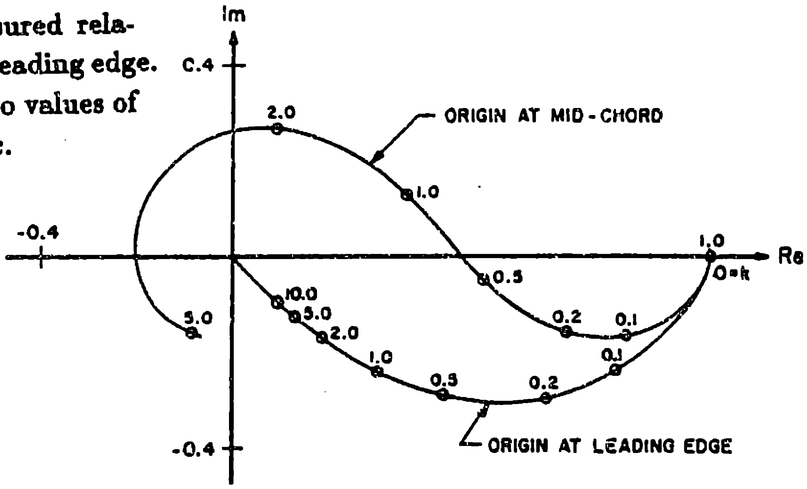

Phase of gust measured relative to midchord or leading edge. Circles correspond to values of reduced frequency k.

Figure 1-1: Sears function versus reduced frequency

1.3.4 Boundary Layer Separation

In 1935 Howarth [6] showed that the counterpart of the Kutta condition for airfoils with rounded trailing edge in steady flow is that equal and opposite fluxes of vorticity are shed from the separation points, where the wake begins. In 1956 Sears [18] extended Howarth's criterion to unsteady flow. The argument is quite elegant.

Consider a two-dimensional thin airfoil with rounded trailing edge and with boundary layer separation at points A and B on the upper and lower surfaces, respectively. In the boundary layer approximation, the vorticity flux at these two points is

$$\int_0^\delta \zeta\,(u - u_{sep})\,dy \;=\; \int_0^\delta \frac{\partial u}{\partial y}\,u_{rel}\,dy \tag{1.15}$$

where u_{sep} is the velocity of the movement of the separation point along the wall, and δ is the boundary layer thickness. Integrating this gives

$$\int_0^\delta \frac{\partial u}{\partial y}\,u_{rel}\,dy = \frac{1}{2}u_e^2 - u_{sep}u_e \tag{1.16}$$

Where u_e is the velocity at the edge of the boundary layer. Taking the difference between the upper and lower surfaces, and remembering Kelvin's theorem,

$$\left[\,\frac{1}{2}u_e^2 \;-\; u_{sep}\,u_e\,\right]_B^A \;=\; -\frac{\partial \Gamma}{\partial t} \tag{1.17}$$

In steady flow, both u_{sep} and $\partial\Gamma/\partial t$ are zero, and the Howarth criterion applies: the edge velocity at the two points of boundary layer separation on either side of the foil are equal. In unsteady flow, and for airfoils with sharp trailing edge, the locations of the separation points A and B are at the trailing edge; also, $u_{sep} = 0$. If the total velocity is written as the sum of a mean undisturbed speed and a perturbation, $u = U + u'$, where $U \sim \mathcal{O}(1)$ and $u' \sim \mathcal{O}(\epsilon)$, ϵ denoting the order of magnitude of the ratios of camber/chord, thickness/chord, and angle of attack of the airfoil (in radians), then

$$\begin{aligned} -\frac{\partial\Gamma}{\partial t} &= \left[\frac{1}{2}u_e^2\right]_B^A \\ &= U\left(u'_{e_A} - u'_{e_B}\right) \\ &= U\gamma_w(x_{TE}, t) \end{aligned} \tag{1.18}$$

This is the same as equation (1.10), which was reached using a classical inviscid analysis: the airfoil and its wake are represented as a bound and free vortex sheet, respectively, with the condition that the rate of vortex shedding at the trailing edge is related to the rate of change of circulation, in order that total circulation is conserved. Equation (1.18) then defines the vortex strength at the trailing edge. By considering inviscid and viscous analyses together, it is clear that the vorticity produced in the boundary layers is the same as the rate of change of vortex shedding from the time-varying bound vortex sheet, and that the net vorticity of the viscous wake is the same as the strength of the free vortex sheet.

For airfoils with boundary layer separation operating in unsteady conditions, equation (1.17) still serves to define the relationship between the rate of change of circulation and the vorticity flux into the wake, but the location of the separation points and their movement must also be considered. No longer are the inviscid and viscous models so easily separable. The circulation cannot be known without knowledge of the separation behaviour, a formidable task. Moore, Rott, and Sears independently proposed as conditions for unsteady separation the simultaneous vanishing of the shear and the velocity at a point within the boundary layer and in a frame of reference moving with the separation point [19, p. 282]. Thus locating the point of unsteady separation requires following the fluid in a Lagrangian frame of reference.

1.4 Research History

Numerous experiments have been performed to validate classical unsteady airfoil theory and to validate the zero-loading formulation of the Kutta condition. At low reduced frequencies quantitative agreement has been found between experimental results and thin airfoil theory predictions. At reduced frequencies higher than about 0.5, however, both the magnitude and the phase of the pressure differential at the trailing edge vary significantly from theory.

Commerford and Carta [2] studied the effects of unsteady gusts induced by the vortex sheet of a transverse cylinder positioned upstream and below a symmetric airfoil. At Reynolds number $Re = 8.2 \times 10^4$ and reduced frequency $k = 3.9$, they found that the surface pressure distribution did have a chordwise variation in phase angle, but that for every angle of attack studied the pressure tended to zero at the trailing edge.

Satyanarayana and Davis [14] measured the pressure differential near the trailing edge of a symmetric airfoil pitching about its quarterchord. The experiments were done at Reynolds number $Re = 5.6 \times 10^5$ and the reduced frequency range was from $k = 0.05$ to $k = 1.2$. They discovered that as the reduced frequency increased, the magnitude of the unsteady pressure differential nearing the trailing edge also increased beyond that predicted by linear theory; furthermore, the phase angles agreed with theory up to $k = 0.8$ but lagged the predicted value at higher reduced frequencies.

Ho and Chen [5] studied the streamline pattern emanating from a plunging symmetric airfoil at varying angle of attack. The reduced frequencies studied ranged no higher than $k = 1.0$. They calculated the location of the phase-averaged stagnation streamline by integrating the phase-averaged velocity components around a rectangular grid within a quarter-chord downstream of the trailing edge. Data was taken no closer than 5% chord length downstream of the airfoil edge. For reduced frequencies

$k < 0.51$ and angle of attack less than 7.5 degrees, the stagnation streamline left the trailing edge tangential to the chordline of the plunging airfoil, in accordance with the steady Kutta condition. But for reduced frequencies near 1.0, the inclination of the stagnation streamline did not follow the instantaneous angle of attack at all.

Lorber and Covert [9] considered the variation in surface pressures on a symmetric airfoil due to a rotating elliptical cylinder located below and aft of the airfoil. Thus the perturbation caused by the cylinder was felt most strongly in the trailing edge region. Experiments were performed with Reynolds number $Re = 3.0 \times 10^5$ to $Re = 1.0 \times 10^6$ and reduced frequencies from $k = 0.5$ to $k = 6.4$. The unsteady velocity produced by the rotating cylinder without the airfoil in the wind tunnel was measured in the plane of the chord. The measured upwash distributions were used with classical airfoil theory to predict unsteady pressure differences on the fixed airfoil. Later, with the airfoil in place, the surface pressures on the airfoil were measured. Difference pressure amplitudes approached zero at the trailing edge position. The fluctuating difference pressure amplitude and phase were found to be in qualitative agreement with predictions based on the measured upwash of the elliptic cylinder, except near the trailing edge, where the measured phase differed significantly from the prediction.

Poling and Telionis [11] conducted experiments on both a pitching airfoil and a fixed airfoil mounted in the wake of the pitching airfoil. For both, the phase-averaged stagnation streamlines were found. The pitching airfoil operated at Reynolds number $Re = 2.0 \times 10^4$ and reduced frequency $k = 2.4$. Its stagnation streamline was found to be approximately tangent to one of the two sides of the wedge formed at the trailing edge. Measurements were taken around the fixed airfoil at Reynolds number $Re = 1.0 \times 10^4$ and reduced frequency $k = 3.9$. The streamline pattern in the immediate vicinity of the fixed airfoil's trailing edge deviated significantly from the direction of the flow around it. The thickness of the boundary layer at the trailing edge was approximately 2% of the chord length; thus the region immediately downstream is fully viscous. Within a distance of 5% of the chord length from the trailing edge, the streamlines displayed large curvatures, implying the presence of strong crossflow pressure gradients. Aft of 5% of the chord length from the trailing edge, the streamlines aligned themselves with the inviscid flow. The authors posited that the finite-thickness viscous layer could sustain a pressure discontinuity and that at high reduced frequencies the zero-loading condition is not applicable.

Finally, Liu, Wo, and Covert [8] studied the phase-averaged streamlines aft of the fixed airfoil in the setup of Lorber and Covert. At a Reynolds number $Re = 1.25 \times 10^5$ and reduced frequency $k = 2$, the ensemble-averaged streamlines were found to remain within the triangle defined by the extension of the upper and lower surfaces of the airfoil, and to leave the trailing edge smoothly.

Chapter 2

Experimental Technique

2.1 Experimental Concept

The purpose of the Flapping Foil Experiment is to determine the response of a two-dimensional hydrofoil subject to vertical gusts at a high reduced frequency. A large stationary hydrofoil is mounted in the test section on the centerline of the tunnel. Upstream there are two small hydrofoils symmetrically offset from the centerline that are driven to pitch in phase, as seen in figure 2-1. Because the upstream foils flap in phase, their vortex sheets create a vertical gust along the centerline of the tunnel.

2.2 The Water Tunnel

The MIT Variable Pressure Water Tunnel is a closed-loop tunnel driven by a single impeller connected to a 75 horsepower motor. The pressure in the tunnel can be varied for cavitation experiments and the like by a vacuum pump. The vacuum pump is also used to deaerate the tunnel. The entire water tunnel has a square profile two stories high. The test section, which is at the top of the loop, is four feet long and has a cross-section twenty inches square. Maximum velocity of the water is about 30 feet/second. Upstream of the test section is a 5:1 contraction section fitted with a honeycomb mesh with cell size of 0.71 inches, and a wake screen to promote flow uniformity. The test section has removable Plexiglass windows on all four sides for

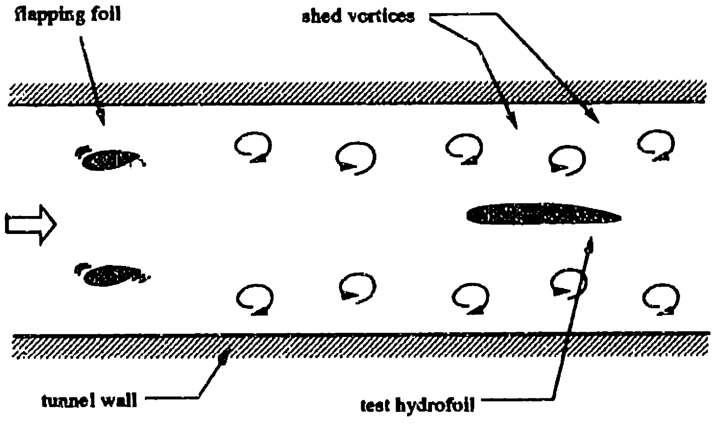

Figure 2-1: Experimental concept

ease of assembling and viewing experiments. Two of the windows have been machined specifically to accomodate this experiment.

Instantaneous velocities are measured in a nonintrusive manner using a laser Doppler velocimeter (LDV). Velocity is measured by detection of the Doppler shift of light scattered by a neutrally-buoyant seed particle in the flow. The intersection of two light beams creates an interference fringe pattern. When seed particles in the water pass through the fringe pattern, the scattered light is collected in a photodetector that detectes the modulation of light intensity at the Doppler frequency. Knowing the wavelength of the incoming laser beams, the half-angle of the beams exiting the focussing lens, and the Doppler frequency, the particle velocity normal to the fringe spacing is determined. The recording of a velocity datum is a random occurrence; it is termed an "event." The LDV used at the MIT Water Tunnel is a three watt argon-ion Lexel Model 95 laser. A two-component system is used for horizontal and vertical velocity measurements in the freestream and wake areas. Nominal measurement volume of the beams measuring streamwise velocity is 53 $\mu m \times 610\ \mu m$, and of the beams measuring vertical velocity is 56 $\mu m \times 645\ \mu m$. A single-component fiber-optic probe set in a rotating mount is used for shear layer measurements: the probe is rotated so that it measures velocity tangent to the hydrofoil surface. Nominal measurement volume of the fiber-optic probe is 100 $\mu m \times 1.1\, mm$. Both laser systems sit on a table and traverse system that can be moved to within 0.01 mm.

The nominal water speed in the tunnel, hereafter called "freestream velocity," is measured by a differential pressure cell in the contraction section.

Before the experiment was assembled in the water tunnel, surveys of the turbulence intensity in the empty test section were done using a TSI conical hot film probe, model 1231W. The LDV was also used as a cross-check on the hot film results. The turbulence intensity was found not to vary with impeller rpm, but is stronger in a 5 inch by 5 inch area in the center of the tunnel. This is because the honeycomb mesh in the contraction section has a 6 inch x 6 inch section removed so that a propeller shaft can be advanced into the test section. The shaft was fully retracted for this experiment. The longitudinal turbulence intensity was found to be 1%.

Also measured in the empty test section were the boundary layers formed on the tunnel walls. The increasing thickness of the boundary layers causes approximately a 1% acceleration of the flow through the test section. This has been confirmed by Pitot-static pressure measurements at one upstream and one downstream location. Throughout the test section, the flow is very uniform over the height and span, to ±0.5% of freestream velocity.

2.3 Description of Experimental Apparatus

The test hydrofoil is a NACA 16 thickness form with maximum thickness $t_o/c = 8.84\%$ and maximum camber $f_o/c = 2.576\%$ with a beveled anti-singing trailing edge modification. Its chord length is 18 inches. Mounted in the test section, it has an angle of attack that can be set by hand. Once mounted in the tunnel, the angle of attack is measured to within 0.05 degrees and was found not to change over the course of the experiment. The measurement of the angle of attack is done by zeroing the laser beam crossing at the leading and trailing edges of the test foil: the vertical and horizontal distances from leading to trailing edges are repeatable to 0.1 mm. The test foil is made of aluminum and has been finished with an anodized coat to prevent

suction side	*pressure side*
0.388	0.389
0.612	0.611
0.810	0.784
0.972	0.972

Table 2.1: Locations of pressure taps

oxidation. It has a boundary layer tripping mechanism on both suction and pressure side $x/C = 0.105$, where x is measured along the nose-tail line. The trips consist of a single row of epoxy cylinders of height 0.008 inches and diameter 0.05 inches. They were placed by laying a strip of tape of thickness 0.008 inches with holes punched from it on the foil surface and coating the tape surface with epoxy. Once the epoxy had cured, the tape was removed to leave behind a uniform row of cylinders. The test hydrofoil has twelve pressure taps of 0.031 inch diameter drilled normal to the foil centerline. These taps lead to 0.219 inch diameter pressure probe holes drilled through the hydrofoil and out through the test section window opposite the LDV. With the boundary layer trips in place, the forwardmost taps are unusable. The locations of usable pressure taps is listed in table 2.1.

The pressure sensors used are cylindrical transducers with 0.187 inch diameter, Sensotec BP331BL Model H, mounted at the ends of stainless steel tubing, with the transducer wiring led inside. These probes are then inserted into the sleeves drilled in the hydrofoil and are held in place by four O-rings. The O-rings also prevent water leakage and eliminate vibrations (figure 2-2). The Helmholtz resonance frequency in the cavity was calculated to be 1723 Hz, well beyond the frequency range of the testing encountered. In order to prevent air entrapment in the cavity, water was allowed to run though the probe sleeves while the probes were inserted.

The pressure transducers were calibrated before and after a given data run. For static calibration, the vacuum pump is used to lower the static pressure in the water tunnel; the transducers are placed in the test hydrofoil and calibrated against static pressure taps flush mounted before and after the test section. Over the course of

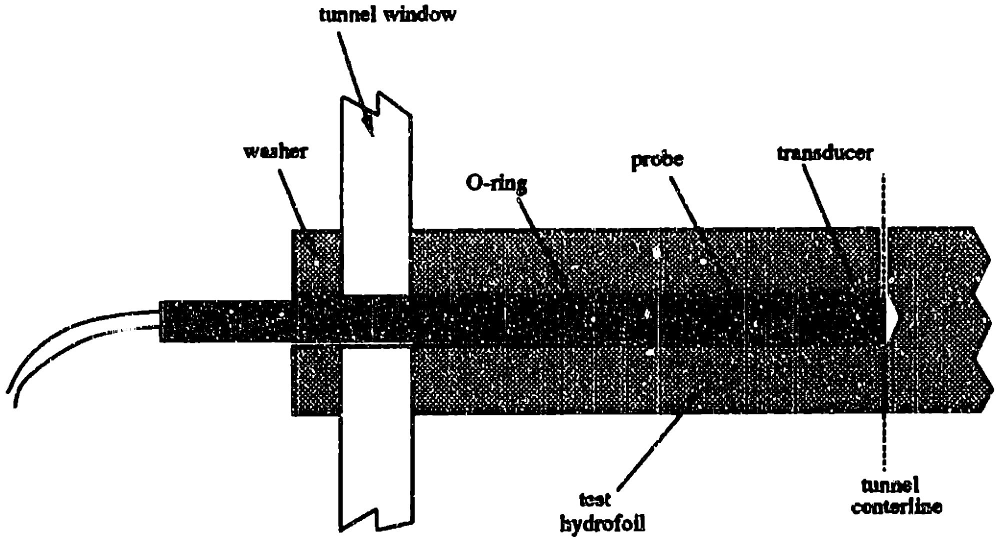

Figure 2-2: Pressure transducers in the test foil

data-taking, no offset drift occurred. In order to determine the dynamic calibration, a method develeped by Hilten, Lederer, and Sethian [4] is used: the transducers are mounted at the base of a hydrostatic column which is then placed on a 100-lb. electrodynamic shaker (figure 2-3). The vibration of the shaker creates a periodic pressure variation at the transducer. If the acceleration of the shaker is $\ddot{y} = -\omega^2 Y sin\, \omega t$ then the pressure at the transducer is

$$p(t) = \rho \left(g - \omega^2 Y sin\, \omega t\right) H \tag{2.1}$$

Pressures measured were compared to readings from an accelerometer mounted on the base of the hydrostatic column. The transducers were found to have constant response up to 100 Hz before and after data-taking.

The upstream flapping foils are NACA 0025 thickness forms with chord length of 3 inches. Extending from each spanwise end are 1 inch diameter shafts positioned so that the flappers rotate about midchord. The flappers are made of anodized aluminum. They are connected by a linkage to an eccentric plate which allows the flappers to rotate through four, six, or eight degrees. In this experiment, the flappers pitched through ± 6 degrees. The eccentric plate and a flywheel are belted to a

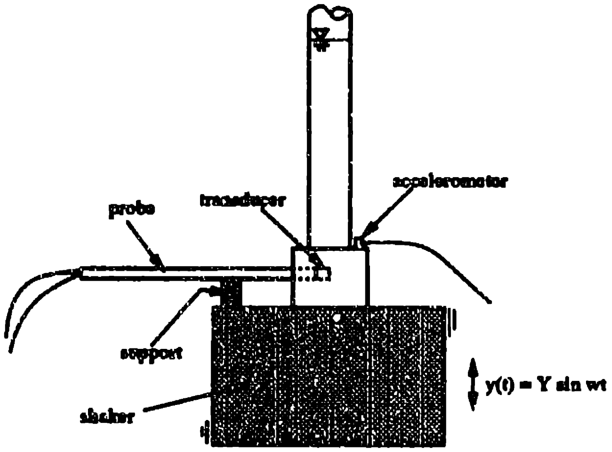

Figure 2-3: Dynamic calibration of pressure transducer

pulley driven by a 2 horsepower motor. A thirteen-bit shaft encoder records the angular position of the flappers in their cycle. The error associated with maintaining the pitch rate of the flappers is less than 0.8%.

A tunnel survey was performed in order to confirm the two-dimensionality of the gust as it convects downstream and passes the large test hydrofoil. Velocities were measured across the span of the tunnel at two vertical locations 0.95 inches aft of the trailing edge of the test foil. The gust structure is maintained through the test section (figure 2-4), but the magnitude of the gust was found to be reduced over a span of about 3 inches on the side of the tunnel opposite the mechanism that drives the flappers. Unsteady data were taken well away from that area.

2.4 Experimental Procedure

The coordinate system has its origin at the trailing edge of the test hydrofoil, with x positive in the upstream direction and z positive in the upward vertical direction. In order to measure velocities closer to the foil surface, the fiber-optic probe was shimmed in its mount so that its beams no longer entered perpendicular to the window. The shim was 0.24 degrees for suction side measurements and 0.49 degrees for pressure

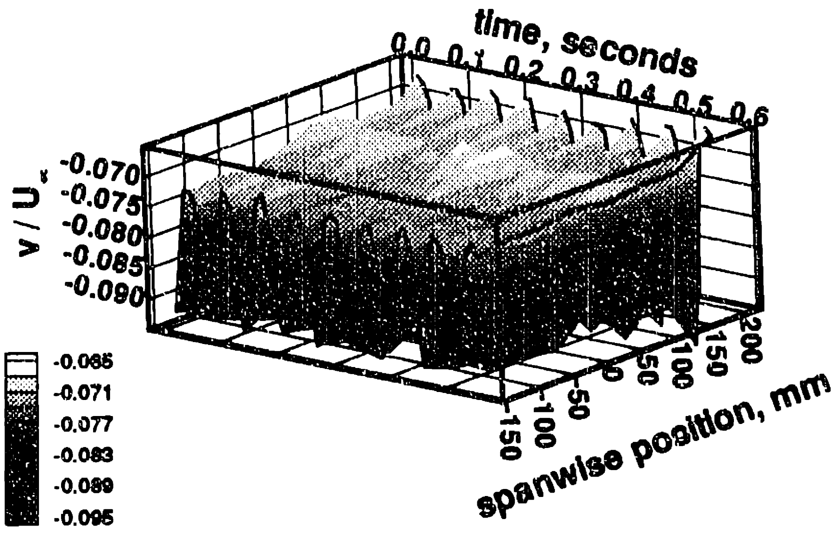

Figure 2-4: Gust structure behind hydrofoil, $x/C = -0.0525$, $z/C = 0.1094$

side measurements. Rotation of the shimmed probe causes a maximum change in the vertical location of the beams' crossing of 0.005 mm.

2.4.1 Steady Flow Measurements

In standard running mode, 250 laser events are averaged for one data point. Any event lying outside of ± 3 standard deviations is then rejected and the remaining data are reaveraged.

For steady flow measurements, data were taken at two operating conditions: $Re = 1.36 \times 10^6$ and $Re = 3.78 \times 10^6$.

Velocity and pressure data were taken in three nested "boxes" bounding the stationary test foil (figure 2-5). These traverses were between the wakes of the flapping foils and the test foil, and along vertcal faces upstream and downstream of the test foil. For the steady flow case, streamwise and vertical velocity was measured at 200 locations circumscribing a 1.14 square foot area; for the unsteady flow case, velocities were measured at 39 locations circumscribing the same area. Static and total pressure were measured along the two vertical faces using a Pitot-static probe. These

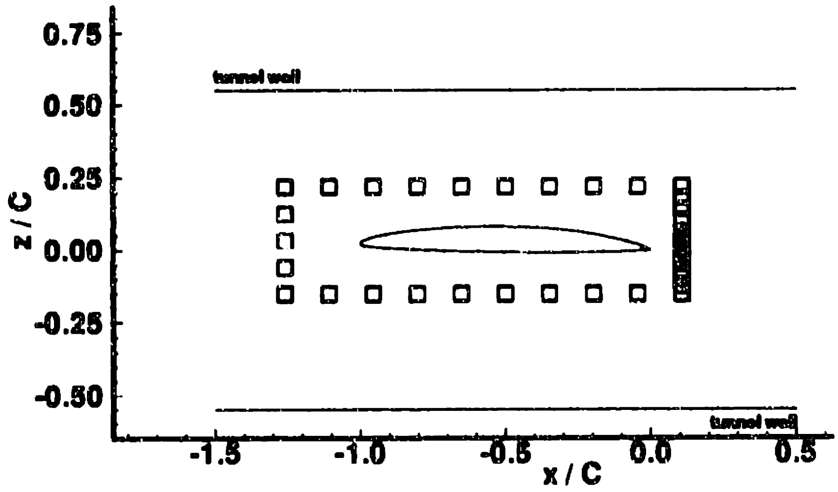

Figure 2-5: Location of bounding boxes

"boxes" provide data for momentum integrations for lift and drag, and as input for CFD codes.

Boundary layer velocity data were taken in nine x/C locations on the suction side and seven x/C locations on the pressure side (table 2.2). For each of these cuts the single-component fiber-optic probe was rotated so that the beam intersection lay tangent to the foil surface in order to measure tangential velocity. The slope of the hydrofoil was culled from the vertices that were used to manufacture the piece. The table on which the laser sits was programmed to move in 0.025-micron steps along a line extending normal to the foil surface, thus preserving the local coordinate system. Again, about 250 "events" were averaged for one data point.

Two sets of wake data were taken. One set continues the measurement of velocities parallel to the slope of the hydrofoil surface at the trailing edge: the fiber-optic beams were left in their rotated position for wake traverses and tangential velocity (u_t) data were taken along normal traverses as before. The second set measures, where possible, the streamwise (u) and vertical (w) velocities along a vertical traverse. The locations of data measurement and components of velocity measured are listed in table 2.3.

Surface pressure measurements were taken at eight x/C locations: four on the

suction side	*pressure side*
0.388	**0.389**
0.612	**0.611**
0.700	**0.759**
0.810	
0.900	**0.900**
0.950	
0.972	**0.972**
0.990	**0.990**
1.000	**1.000**

Table 2.2: Locations of steady boundary layer velocity measurements

suction side		*pressure side*	
x/C	type of velocity data	x/C	type of velocity data
1.01	$u_t; w$	1.01	$u_t; w$
1.025	$u_t; w$	1.025	$u_t; w$
1.05	$u_t; u, w$	1.05	$u_t; w$
1.10	u, w		
1.20	u, w		

Table 2.3: Location and type of wake velocity measurements

suction side and four on the pressure side. Pressure data was obtained by averaging 1000 samples of data over one second. This was repeated numerous times at each tap location.

2.4.2 Unsteady Flow Measurements

Unsteady data was ensemble-averaged in the following way: a 13-bit shaft encoder records the angular position of the flappers in their ±6 degree rotation. An entire flapper cycle consists of the flapper moving from zero, to -6 degrees, to zero, to +6 degrees: a single harmonic of the driving frequency. This cycle is broken down into 180 parts or "bins." Any time a laser event occurs or a surface pressure is measured, the information is collected and sorted according to where the flappers were in their rotation, that is, the information is placed in a bin corresponding to when it occurred during the flapper cycle. By filling all the bins with enough data an equivalent flap is reconstructed. In this experiment, 88 repetitions of 512 angle-correlated velocity readings were obtained. The average number of points per bin was 250, with no bin having less than 200. Within each bin, means and standard deviations are computed; points farther than three standard deviations are rejected and the remaining points are reaveraged. Since the flapper cycle is a single harmonic and there are 180 bins per cycle, the Nyquist frequency is the nintieth harmonic of the driving frequency.

Unsteady velocity data were taken in three nested "boxes" bounding the stationary test foil. These traverses were between the wakes of the flapping foils and the test foil, and along vertcal faces upstream and downstream of the test foil. Streamwise and vertical velocity was measured at 39 locations circumscribing a 1.14 square foot area. Mean static and total pressure were measured along the two vertical faces using a Pitot-static probe. These "boxes" are used as input for CFD codes.

Boundary layer velocity data were taken in six x/C locations on the suction side and two x/C locations on the pressure side (table 2.4). For each of these cuts the single-component fiber-optic probe was rotated so that the beam intersection lay tangent to the foil surface in order to measure tangential velocity.

Unsteady surface pressure measurements were taken at eight x/C locations: four

suction side	*pressure side*
0.388	
0.612	
0.900	
0.972	0.972
0.990	
1.000	1.000

Table 2.4: Locations of unsteady boundary layer velocity measurements

on the suction side and four on the pressure side. Pressure data was obtained by ensemble-averaging 11 batches of 4096 bursts of data. The 180 bins that divide an equivalent flapper period tended to fill evenly.

Chapter 3

Experimental Results: Steady Flow

With the use of the experimental technique previously described, velocity fields and surface pressures about the test hydrofoil were measured at two Reynolds' numbers: $Re = 1.36 \times 10^6$ and $Re = 3.78 \times 10^6$. The angle of attack of the test foil was 1.18 degrees.

3.1 Bounding Box Data

The flow field through the test section was measured around the bounding boxes described previously. Day to day the freestream velocity varied by less than 1% at both operating conditions. Conservation of mass was found to hold through the box to within 0.6% of the total flux through the upstream face. Figures 3-1 through 3-4 show the measured velocity through the test section in the middle of the three nested bounding boxes for the high Reynolds number case. The average standard deviation of streamwise velocity excluding the wake regions is 0.023, and of vertical velocity is 0.012. The wake region of the test foil is well defined. Vertical velocity measurements show irregularities in that region, about $\pm 2\% \, z/C$, because the speed is nearly zero; in that region the standard deviation of vertical velocity is 0.094 and of streamwise velocity is 0.119. The wake regions are also well defined in the pressure traverse, figures 3-5 and 3-6. The acceleration of the flow field due to the presence of the test foil is apparent in the variations in $(C_p)_{stat}$ along the tunnel vertical coordinate.

The lift and drag of the test hydrofoil were computed by a momentum integral around the bounding box. The results can be found in table 3.1.

	$Re = 1.36 \times 10^6$	$Re = 3.78 \times 10^6$
C_L	0.493	0.466
C_D	0.0103	0.0101

Table 3.1: Measured lift and drag coefficients, steady flow

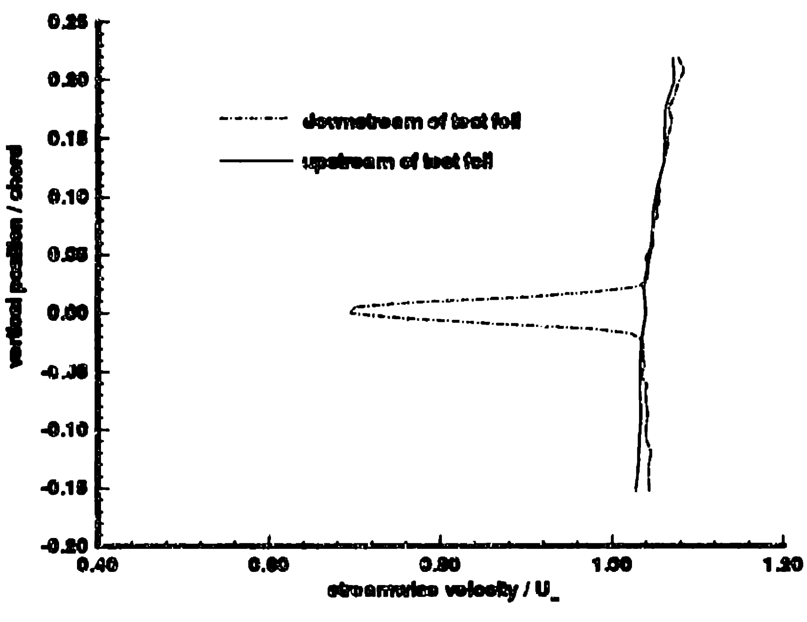

Figure 3-1: Streamwise velocity around middle bounding box

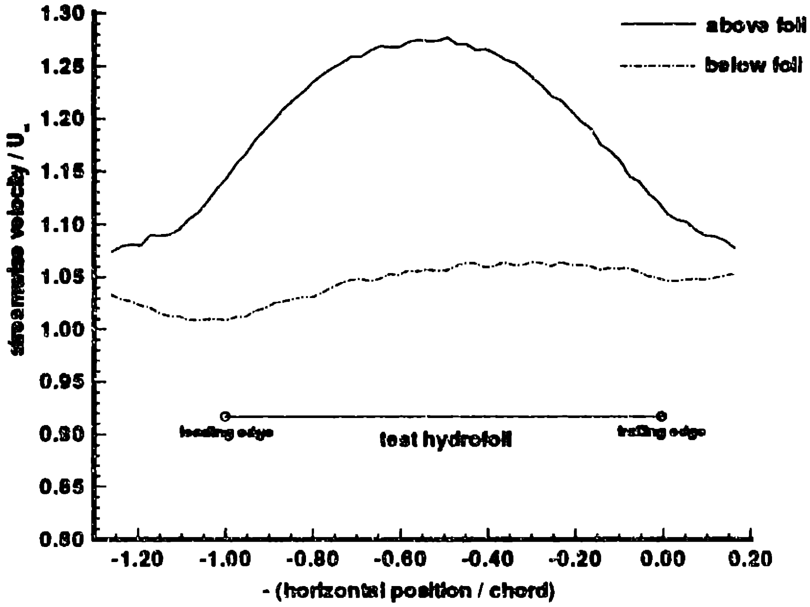

Figure 3-2: Streamwise velocity around middle bounding box

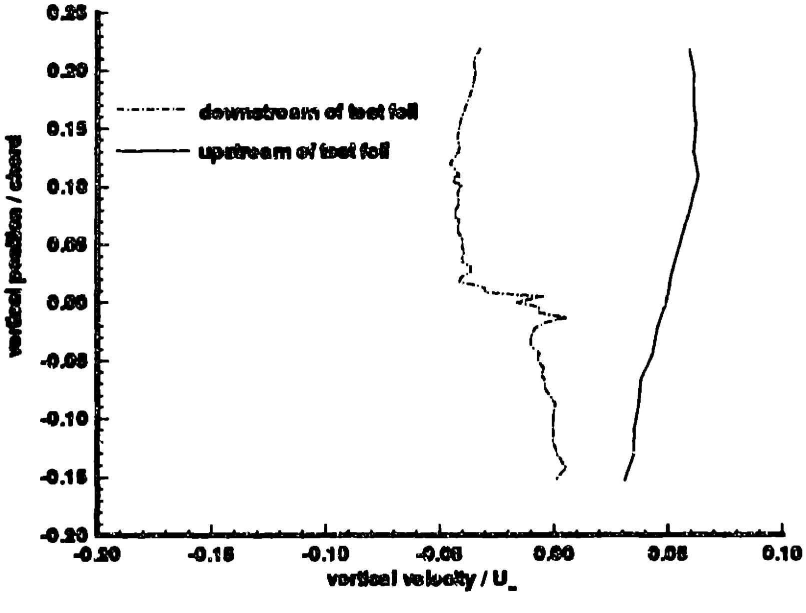

Figure 3-3: Vertical velocity around the middle bounding box

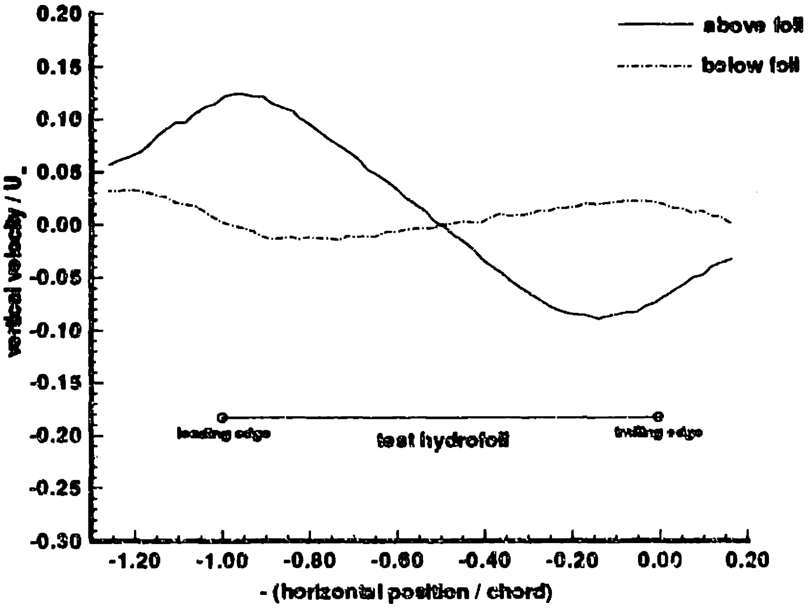

Figure 3-4: Vertical velocity around the middle bounding box

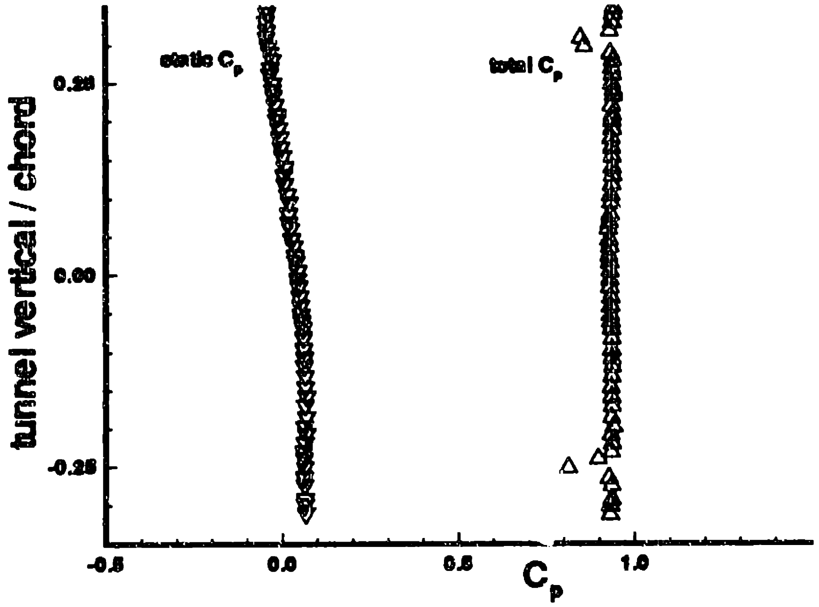

Figure 3-5: Pressure along upstream face of bounding box, $Re = 3.78 \times 10^6$

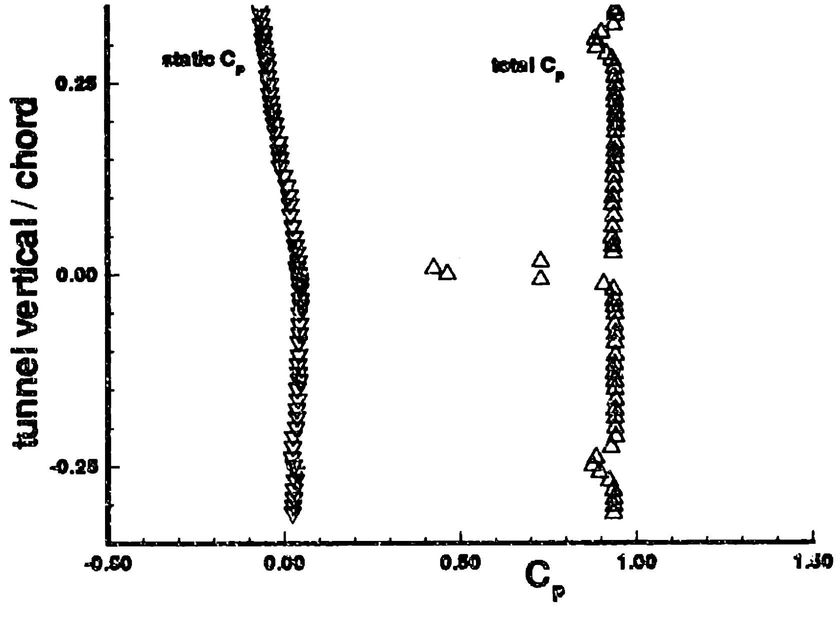

Figure 3-6: Pressure along downstream face of bounding box, $Re = 3.78 \times 10^6$

3.2 Boundary Layer Measurements

Boundary layer velocities were measured at nine suction side locations and eight pressure side locations. Velocities were measured at approximately 150 normal height locations per cut. The exact location of the foil surface was then determined by considering the data obtained in the viscous sublayer: in that region, velocity is linear with distance from the surface, and a line was fit to the data to extrapolate the surface height in the tunnel coordinate system, which has its origin at the test foil trailing edge. When inadequate data were measured in the sublayer, the surface height in the tunnel coordinate system was taken in relation to surrounding boundary layer cuts and the hydrofoil geometry. The actual location of the foil surface is known to within 0.1 millimeters.

The reduced data can be seen for the low Reynolds number case in figures 3-7 and 3-8. Difficulties were encountered around $x/C = 0.8$: the laser beams do not form an adequate sampling volume near the hydrofoil surface. In this area is one of two bolts extending from the foil through the tunnel window, holding the foil in place. It is thought that there is a compression of the window in this area and that the beams are being redirected as they pass through it. The lack of data near the surface can be seen at the $x/C = 0.810$ cut, where after the first three points, no data were measured until much farther out in the boundary layer.

The data for the high Reynolds number case can be seen in figures 3-9 and 3-10. Again, difficulties were encountered on the suction side; no measurements were taken at $x/C = 0.810$, and at $x/C = 0.700$ data could not be taken until far out into the boundary layer.

For both operating conditions, the flow has separated between $x/C = 0.950$ and $x/C = 0.972$. The edge velocity at the trailing edge on the pressure side is $u/U_\infty = 0.991$; on the suction side, the edge velocities at $x/C = 0.950$ and $x/C = 0.972$ are $u/U_\infty = 1.033$ and $u/U_\infty = 0.986$, respectively. Pronounced flow reversal is visible at the trailing edge.

The standard deviation of velocity through the boundary layer is a measure of turbulent activity: more turbulent regions have higher standard deviations; similarly, the magnitude of the standard deviation drops off to freestream values at the edge of the boundary layer. Along the pressure side of the test hydrofoil (figure 3-11), this behavior is well pronounced: the standard deviation is higher close to the foil surface and slowly decreases toward the edge of the boundary layer. On the suction side, this pattern breaks down towards the trailing edge: by $x/C = 0.900$, there is a more volatile region somewhat above the foil surface (figure 3-12). This region grows as it moves downstream (figure 3-14). This is another indication that separation is occurring: the separated flow has very little speed and has intense turbulent activity, with a layer of smoother reversed flow along the surface.

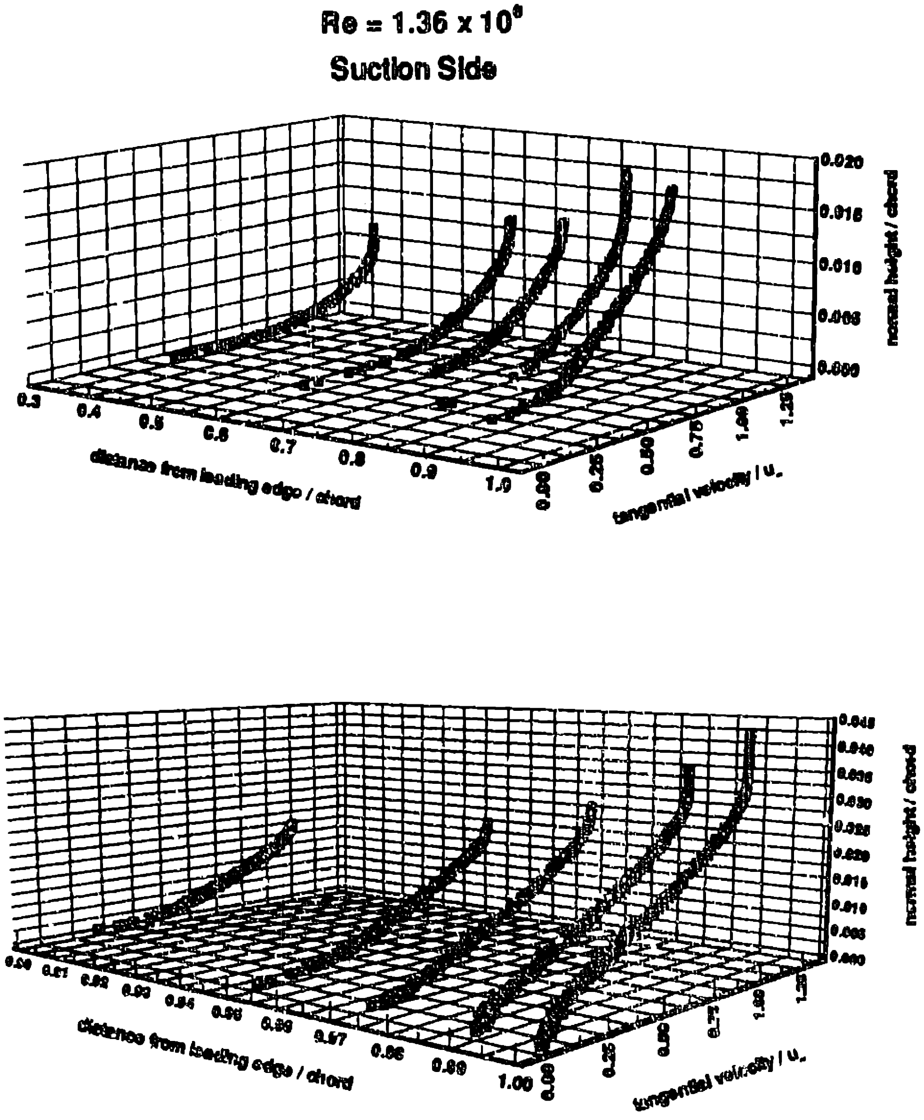

Figure 3-7: Boundary layer velocity profiles, suction side

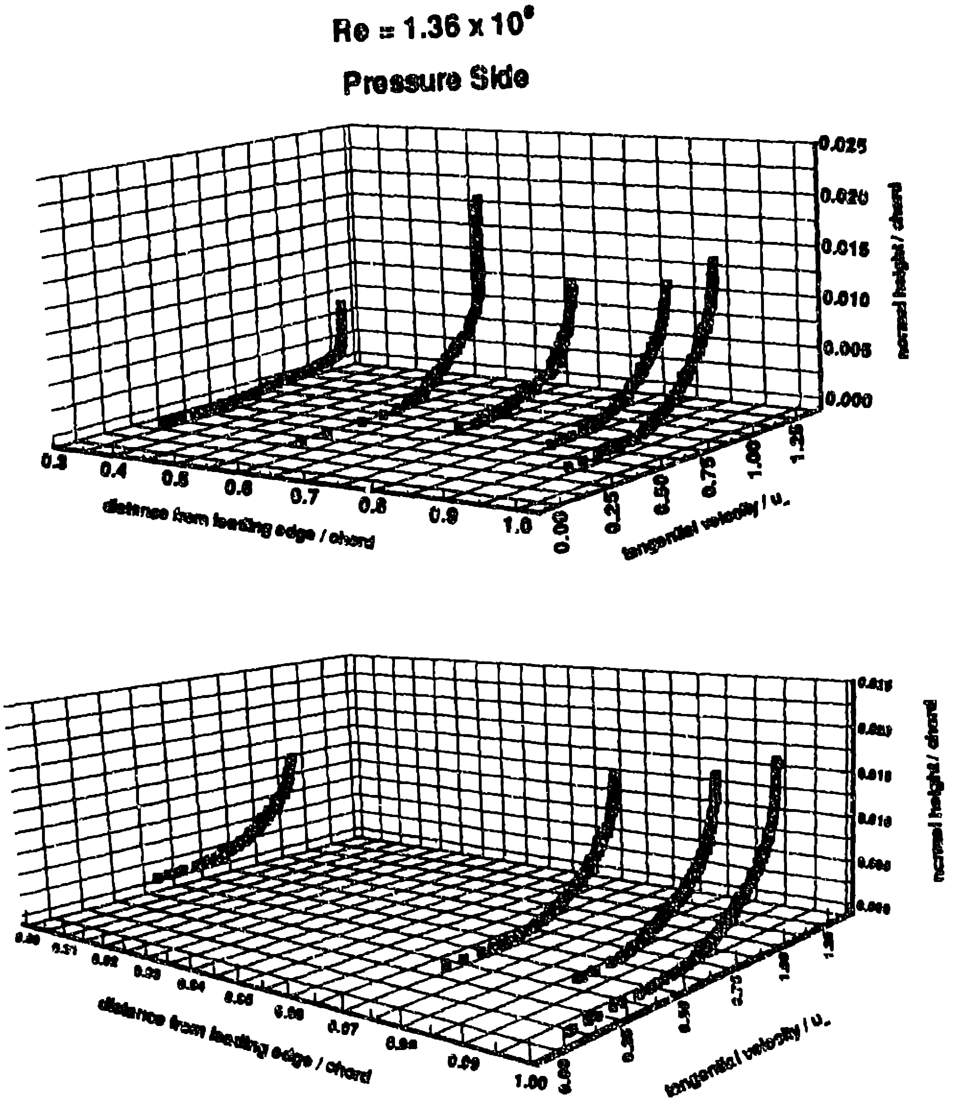

Figure 3-8: Boundary layer velocity profiles, pressure side

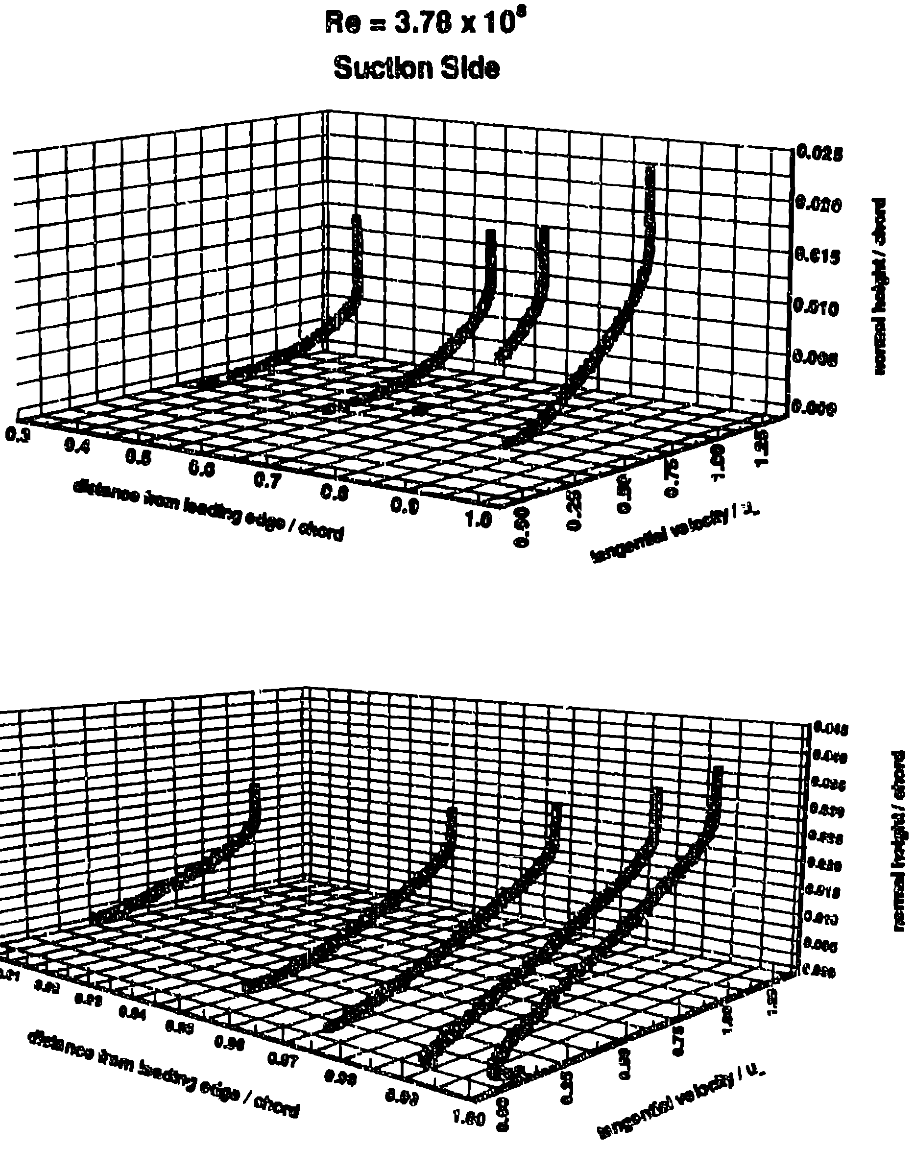

Figure 3-9: Boundary layer velocity profiles, suction side

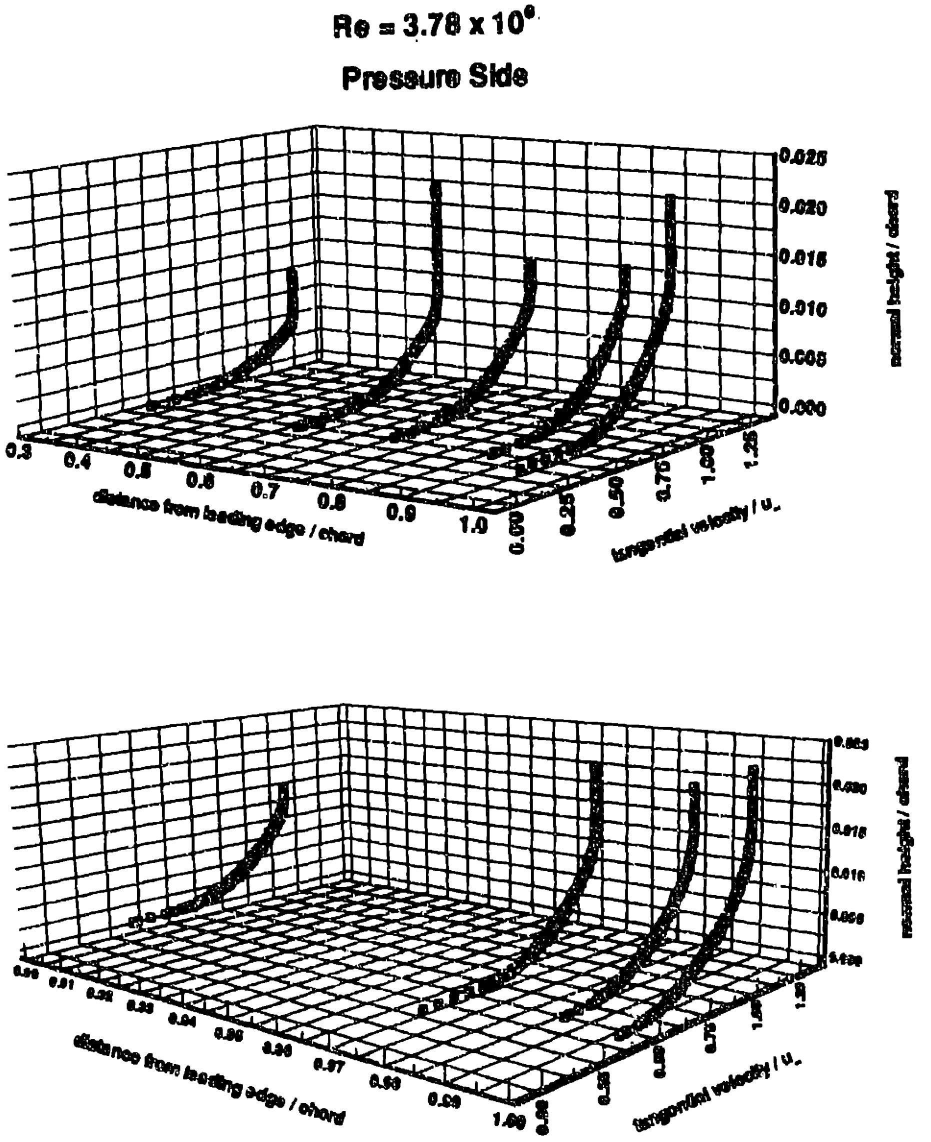

Figure 3-10: Boundary layer velocity profiles, pressure side

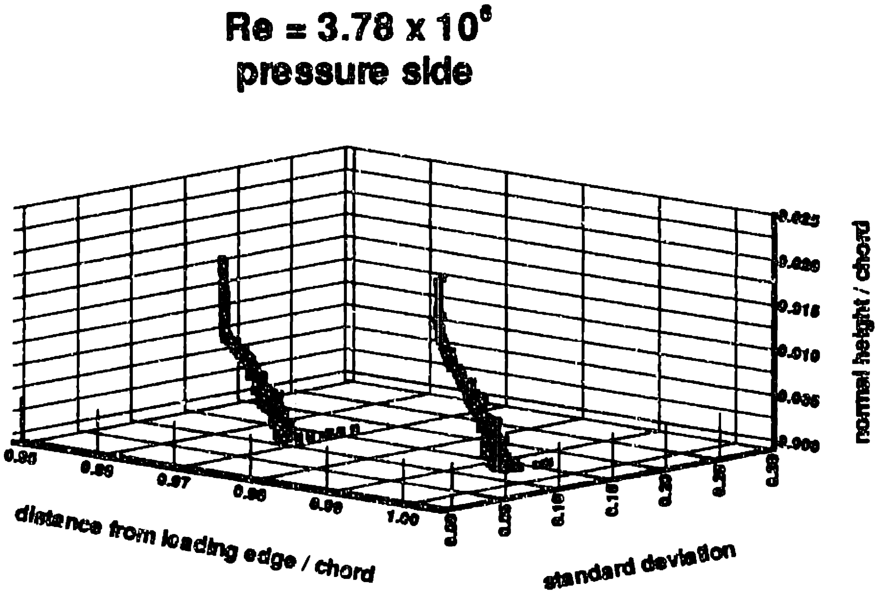

Figure 3-11: Standard deviation of velocity, pressure side

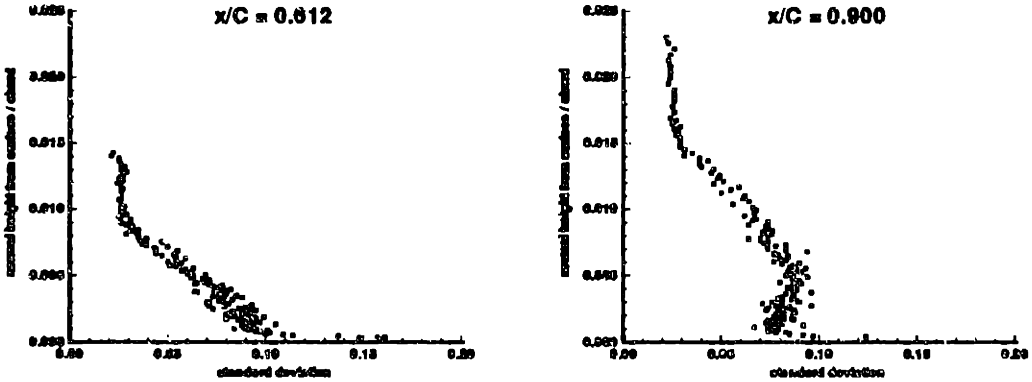

Figure 3-12: Standard deviation of velocity, suction side

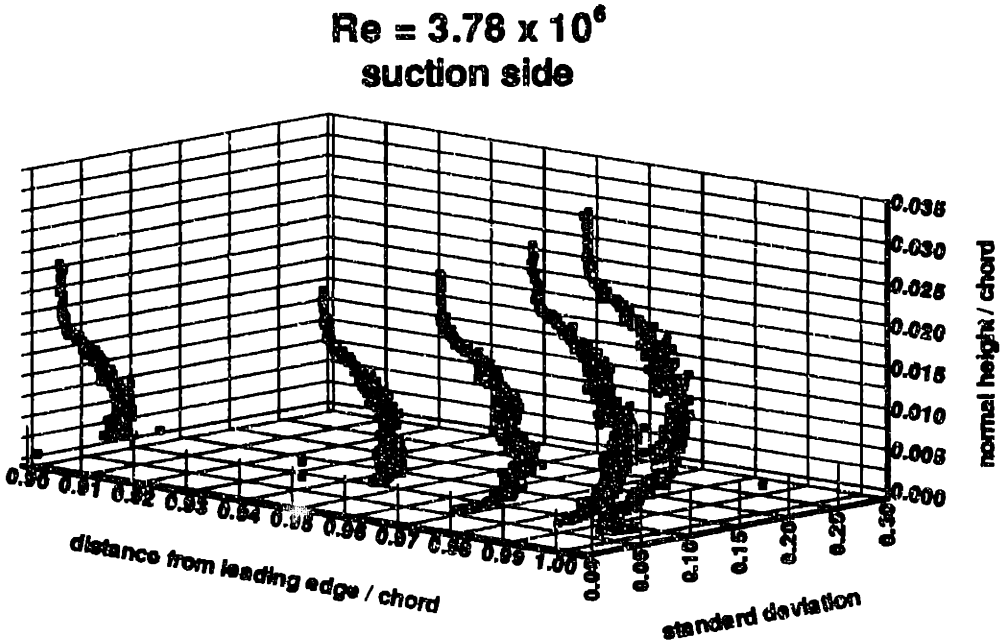

Figure 3-13: Standard deviation of velocity, suction side

3.3 Wake Measurements

Two types of wake measurements were taken. In one set, tangential and vertical velocities were measured along traverses normal to the hydrofoil surface at the trailing edge. This was done because the hydrofoil itself would block laser beams oriented to measure velocity along a vertical traverse too close to the trailing edge. The data is shown in figures 3-14 through 3-17. Here, the distances are measured along the normal traverse from the vertical location of the trailing edge. In the other set of measurements, streamwise and vertical velocities were measured along vertical traverses further aft of the trailing edge. This data is shown in figures 3-18 and 3-19. Here, the distances are measured along the tunnel vertical from the vertical location of the trailing edge. The relative angle of the flow in the wake is shown in figures 3-20 and 3-21. It is clear that the predominant direction of the flow above the foil is not aligned with the direction of the foil surface near the trailing edge; the flow has separated in some region just upstream of the trailing edge.

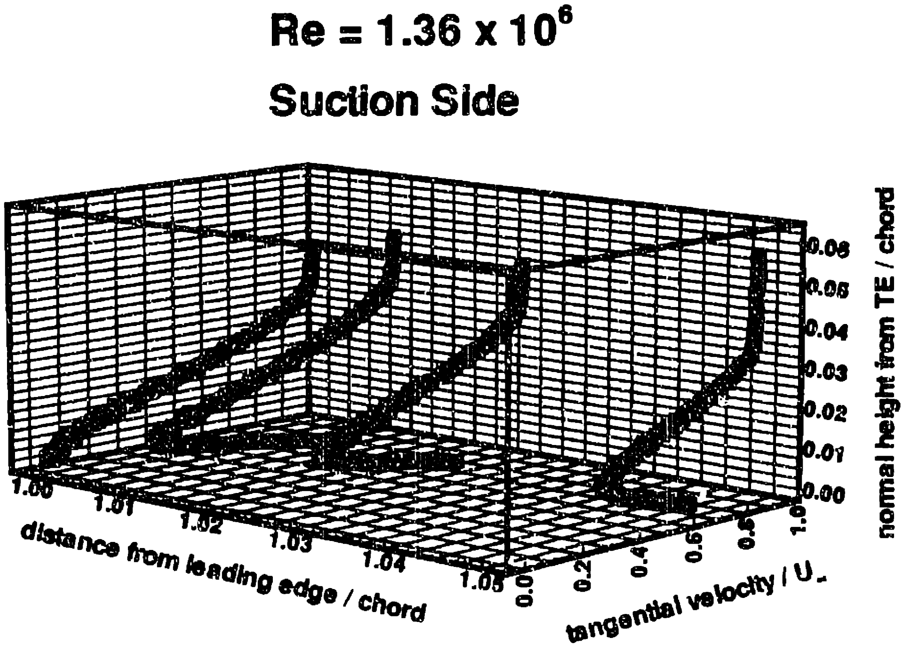

Figure 3-14: Tangential velocities in the wake, suction side

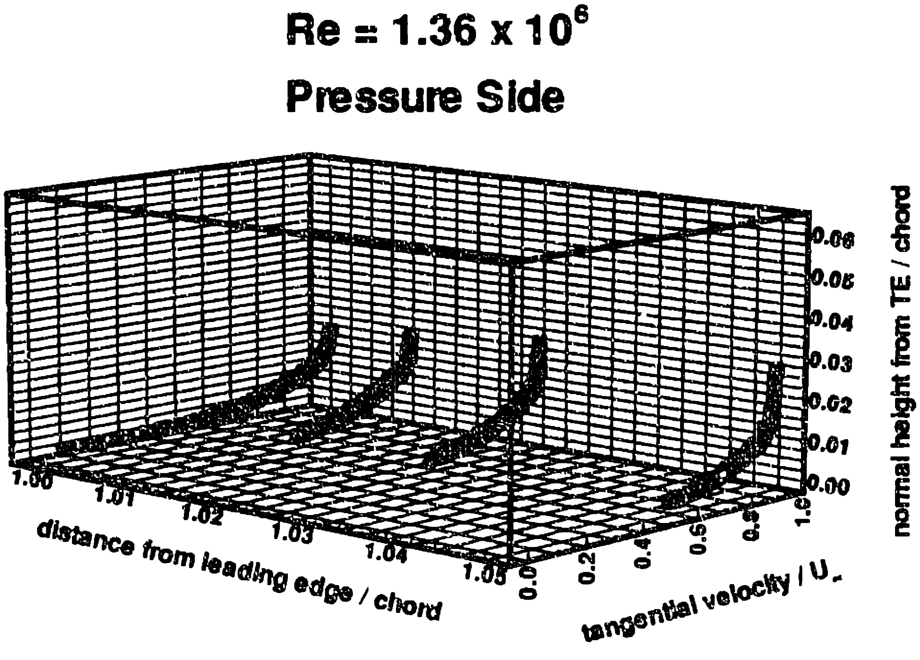

Figure 3-15: Tangential velocities in the wake, pressure side

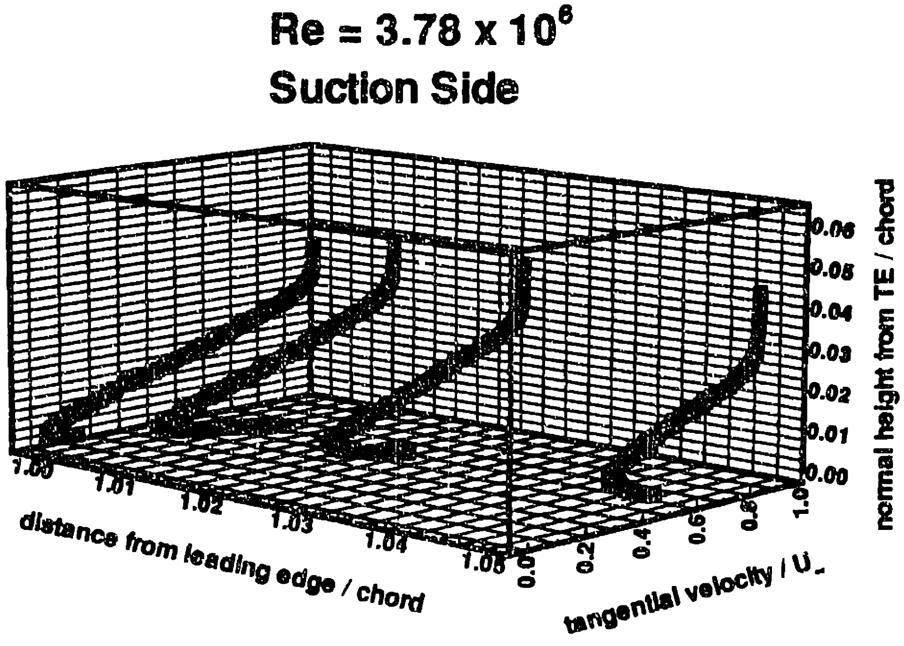

Figure 3-16: Tangential velocities in the wake, suction side

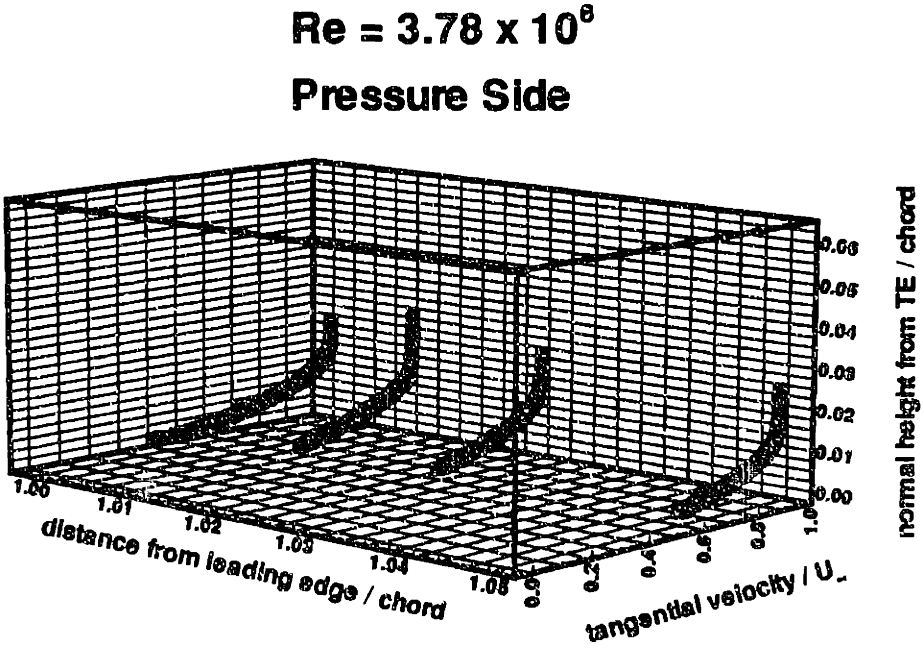

Figure 3-17: Tangential velocities in the wake, pressure side

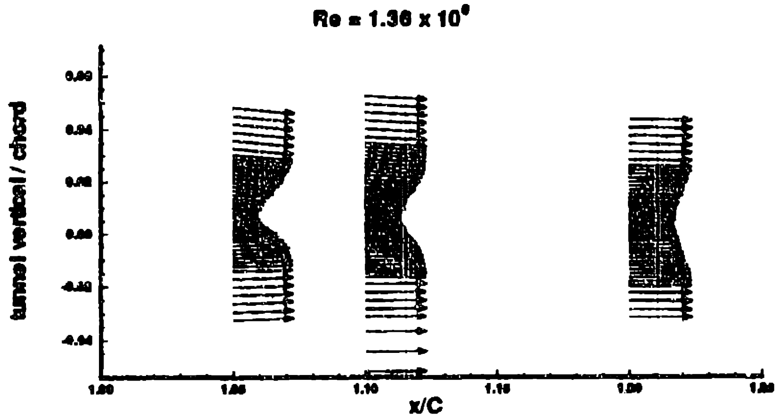

Figure 3-18: Velocity field in the wake, $Re = 1.36 \times 10^6$

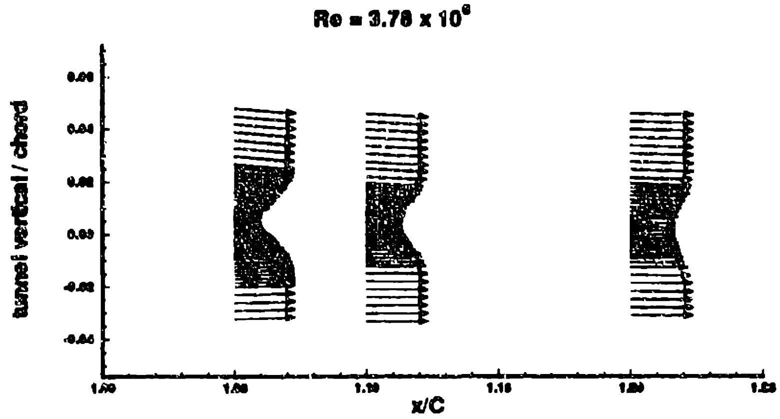

Figure 3-19: Velocity field in the wake, $Re = 3.78 \times 10^6$

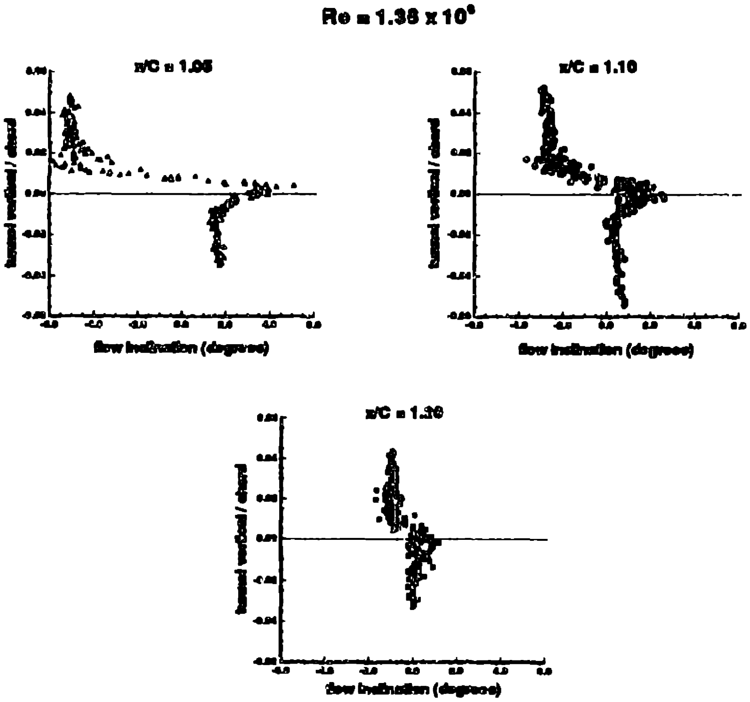

Figure 3-20: Flow inclination in the wake, $Re = 1.36 \times 10^6$

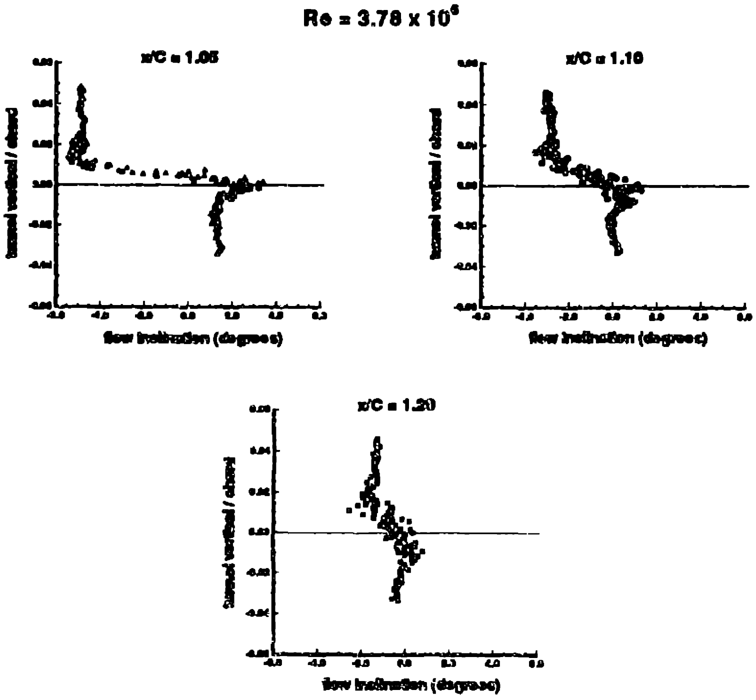

Figure 3-21: Flow inclination in the wake, $Re = 3.78 \times 10^6$

3.4 Surface Pressure Measurements

Surface pressure measurements were taken at four suction side and four pressure side locations. In processing the data, the hydrostatic pressure due to the difference in elevation between the two surfaces of the hydrofoil was removed. As a check, the pressure coefficient was calculated from the edge velocity at the locations of boundary layer measurements,

$$\begin{aligned} C_p &= 1 - \left(\frac{q}{U_\infty}\right)^2 \\ &\approx 1 - \left(\frac{U_e}{U_\infty}\right)^2 \end{aligned} \tag{3.1}$$

where q is the magnitude of the total velocity vector. The approximation of the total velocity being equal to the edge velocity breaks down in separated regions, which are characterized by large increases in the normal velocity. This is shown for the case of $Re = 3.78 \times 10^6$ in figure 3-22. The largest difference in C_p occurs, as expected, near the trailing edge on the upper surface. Elsewhere there is a constant shift of $\Delta C_p \sim 0.046$. The data can be seen in figures 3-23 and 3-24.

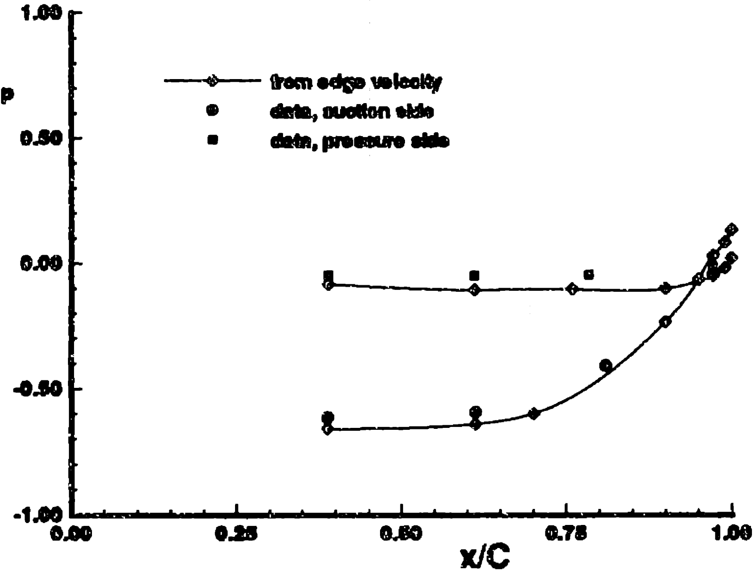

Figure 3-22: Surface pressure given by edge velocity distribution

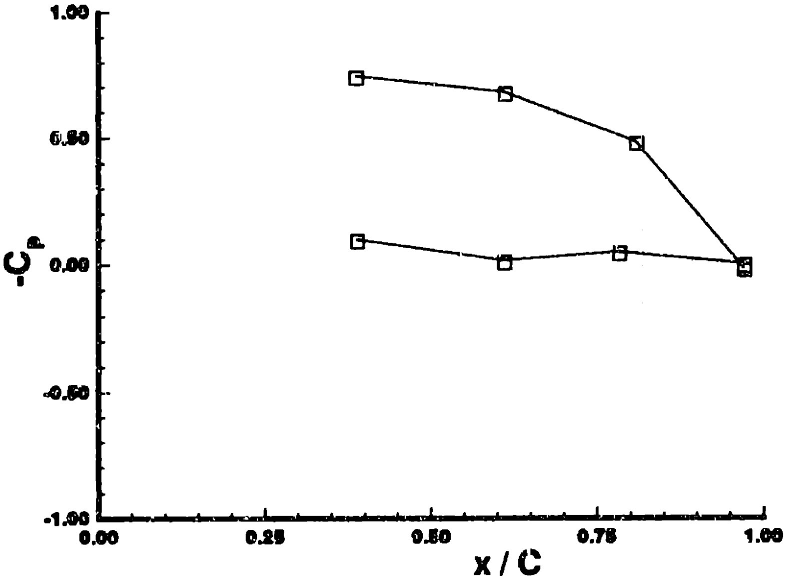

Figure 3-23: Surface pressure along chord, $Re = 1.36 \times 10^6$

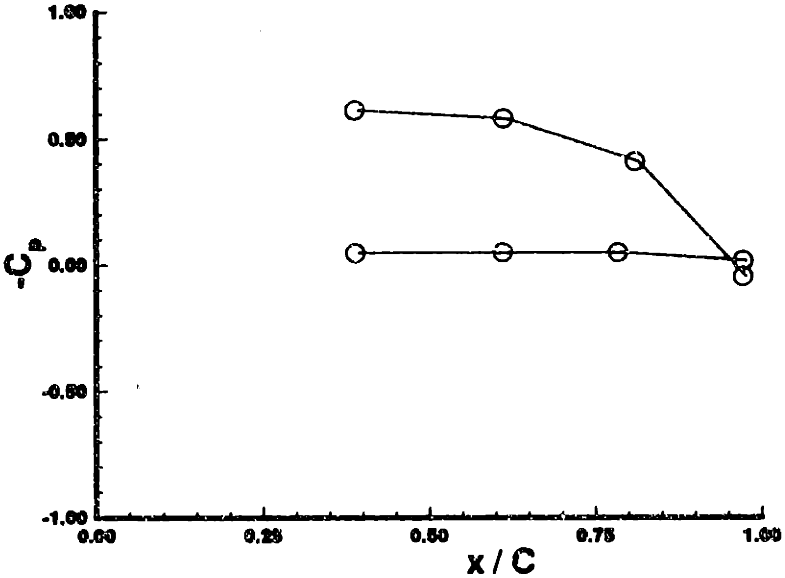

Figure 3-24: Surface pressure along chord, $Re = 3.78 \times 10^6$

Chapter 4

Experimental Results: Unsteady Flow

With the use of the experimental technique described previously, velocity fields and surface pressures about the test hydrofoil were measured at Reynolds number $Re = 3.78 \times 10^6$ and reduced frequency $k = 3.6$. The angle of attack of the test foil was 1.34 degrees.

4.1 Bounding Box Data

The flow field through the test section was measured around the bounding boxes described previously. The freestream velocity was found to be constant to within 0.1% over the course of data-taking. Conservation of mass was found to hold to within ±2.5% of the total flux though the 1.14 square foot box per flapper period (figure 4-1). This larger mass flux error is due to the coarse spacing of data collection points. Figure 4-2 shows the vertical velocity measured along the middle bounding box just in front of the test hydrofoil leading edge. The velocity is a clean first harmonic gust with small standard deviation over the flapper cycle, confirming that the two upstream flapping foils are creating a small perturbation in accordance with linear theory. Along the upstream face of the bounding box, the mean standard deviation of the streamwise velocity is 0.0286, and of the vertical velocity is 0.0157.

In the wake region of the test hydrofoil, the standard deviation climbs to 0.0962 for the streamwise velocity and 0.0791 for the vertical velocity. The mean static and total pressure coefficients were measured with a Pitot-static tube along the vertical faces of the bounding box. Extreme fluctuations in the wake region of the test hydrofoil prevented reliable data gathering between $\pm 0.01\, z/C$ (figures 4-3, 4-4). The width of the wakes from the upstream flappers has widened in the unsteady flow, as can be seen by the loss of well-defined wake areas in the pressure traverses. The wake now contains the wide vortex street emanating from the flappers.

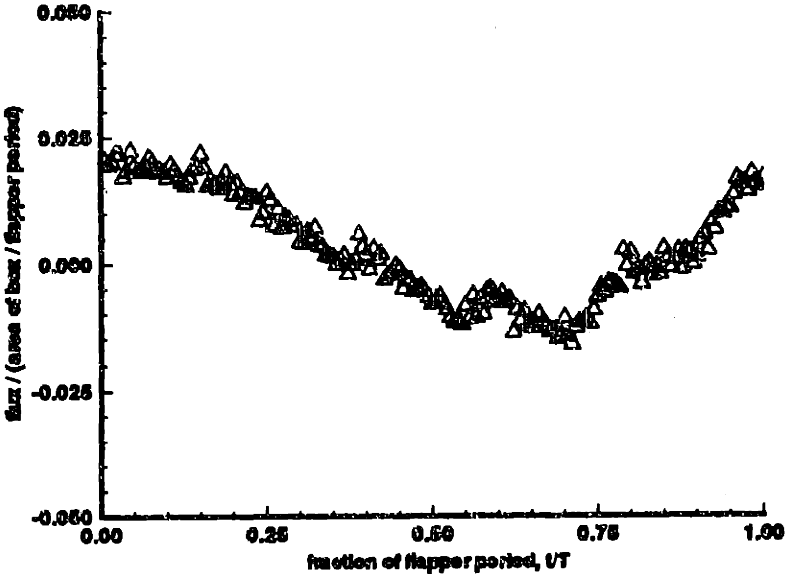

Figure 4-1: Unsteady flux through the bounding box

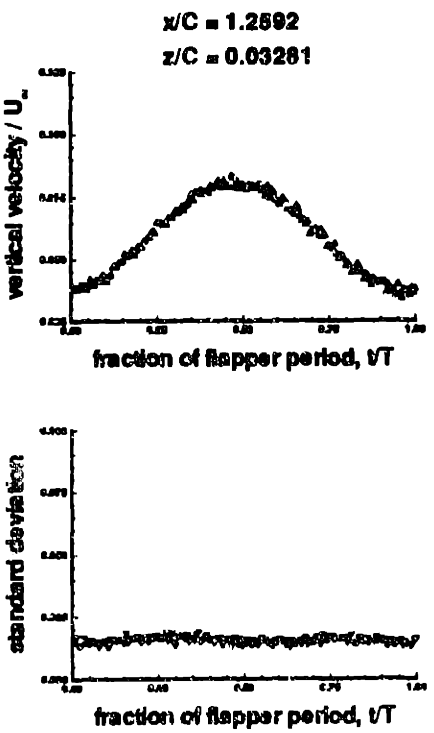

Figure 4-2: Vertical velocity ahead of leading edge of test foil

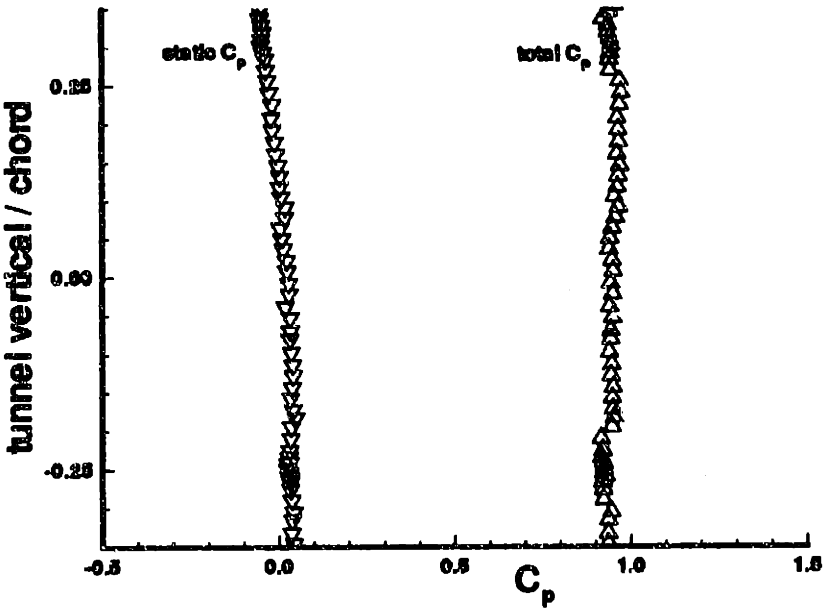

Figure 4-3: Pressure along upstream face of bounding box

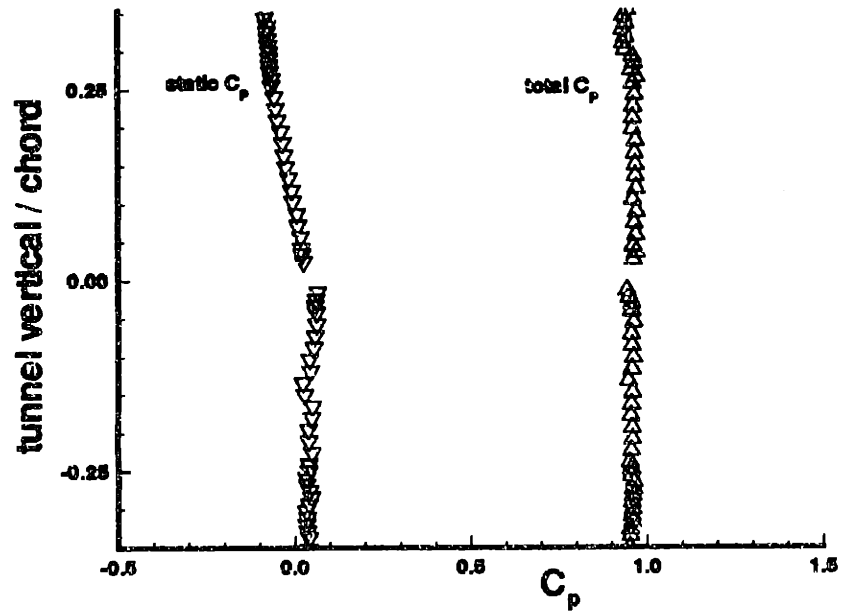

Figure 4-4: Pressure along downstream face of bounding box

4.2 Boundary Layer Measurements

Boundary layer measurements were taken along traverses normal to the local foil surface inclination at eight x/C locations. For each of the cuts, data were taken at between 9 and 14 normal distances from the surface, clustered toward the wall (figure 4-5). In order to confirm the laser measurements of normal distance from the surface, the mean velocity and standard deviation were compared to the steady flow values.

Recall that the acquisition of a time series of velocity at one location requires filling 180 "bins" with an average of 250 points. This process takes about thirty minutes. In separated regions, where the flow is very close to stagnant, getting a single data point can take as much as four hours! An example of the velocity history in the separated region is shown in figure 4-6. This figure shows the velocity over one flapper period at 0.34 mm from the foil surface, less than 0.1% of a chord length away. The once-per-flap tendency is very strong, with some higher harmonics an order of magnitude weaker.

An instructive way to view the boundary layer data is to consider only the unsteady part of the flow. To first order, the mean and the unsteady components are separable; since it is a small gust ($v/U_\infty = 0.022$) that is being convected, the decoupling can be done with confidence. By viewing only the unsteady part of the flow, phase information becomes prominent. The amplitude of the unsteady part of the velocity over a flapper period can be seen in figures 4-7 through 4-14.

Consider the velocity on the suction side, at $x/C = 0.388$ (figure 4-7). The abscissa represents time as a fraction of flapper period; the ordinate represents distance along a normal to the local surface inclination. The bottom horizontal is closest to the foil surface, and the top horizontal is near the edge of the boundary layer. A slight phase shift through the height of the boundary layer can be seen: the gust at the edge of the boundary layer is leading the gust inside the boundary layer. This is to be expected, since the gust at the edge of the boundary layer is being convected at a higher velocity than the gust inside the boundary layer. This behavior is more prominent at positions farther downstream. By $x/C = 0.612$ (figure 4-8), the gust at the edge of the boundary layer has moved even further ahead; at $x/C = 0.900$ (figure 4-9), the two regions are separated by over a quarter period in phase. By $x/C = 0.972$, something very interesting has occurred: the gust at the edge has essentially broken off from the gust deeper in the boundary layer (figure 4-10). There is a complete phase reversal between the two regions, with a region of attenuated unsteady velocity amplitude in between. This sheared gust structure continues over the rest of the chord (figures 4-11 and 4-12). At these locations there appears to be some phase shifting very close to the foil surface as well. Recall that in steady flow, separation occurs between $x/C = 0.950$ and $x/C = 0.972$. Unsteady separation would also occur near this region, but its location has not been determined. Recall that Moore, Rott, and Sears propose as conditions for unsteady separation the simultaneous vanishing of the shear and the velocity at a point within the boundary layer and in a frame of reference moving with separation. Extracting the movement of the separation point would require working in a Lagrangian frame of reference, and not the experimentally more tractable Eulerian frame.

This sort of phase shifting of the gust structure in the boundary layer also exists on the pressure side, but to a lesser extent. Near and at the trailing edge (figures 4-13 and 4-14), the gust at the edge of the boundary layer leads that inside, but there is not a complete reversal as on the suction side. The pressure gradient on the lower surface is considerably less adverse than that near the trailing edge on the upper surface.

Another way to view the phase shift of the velocity gust through the boundary layer is through Fourier analysis. The phase of the first harmonic can then be viewed explicitly (figures 4-15 and 4-16). Here the phase angle in degrees is referenced to some arbitrary angle and not to the position of the flappers in their rotation. The shearing of the two regions of the boundary layer is very well shown.

Fourier analysis also gives the magnitude of the harmonic content of each time series of velocity. Throughout the boundary layer, the velocity is essentially a clean first harmonic, with higher harmonics all an order of magnitude smaller. The disappearance of the gust between the phase-shifted regions of the boundary layer at

$x/C = 0.990$ is seen in figure 4-17. The five harmonic analyses are for the outermost five data points. In between the two regions, the magnitude of the first harmonic decreases by a factor of 10, to the same magnitude as the second harmonic.

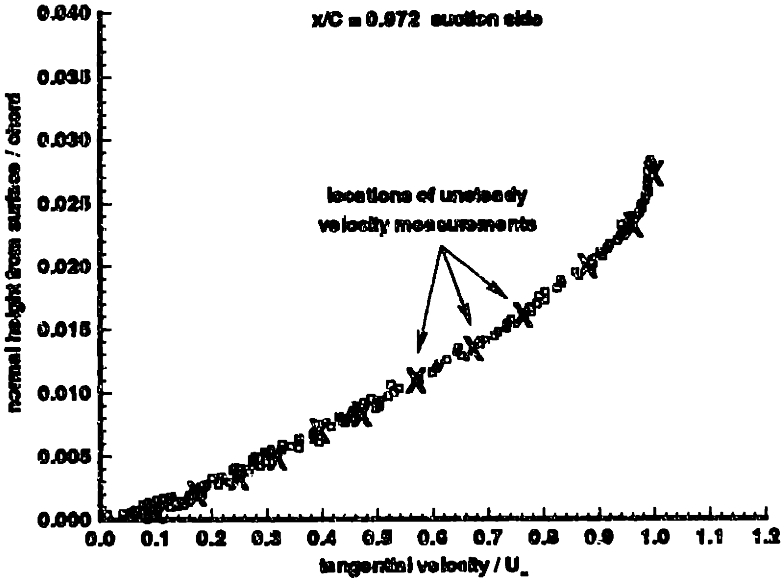

Figure 4-5: Location of boundary layer measurements within mean profile

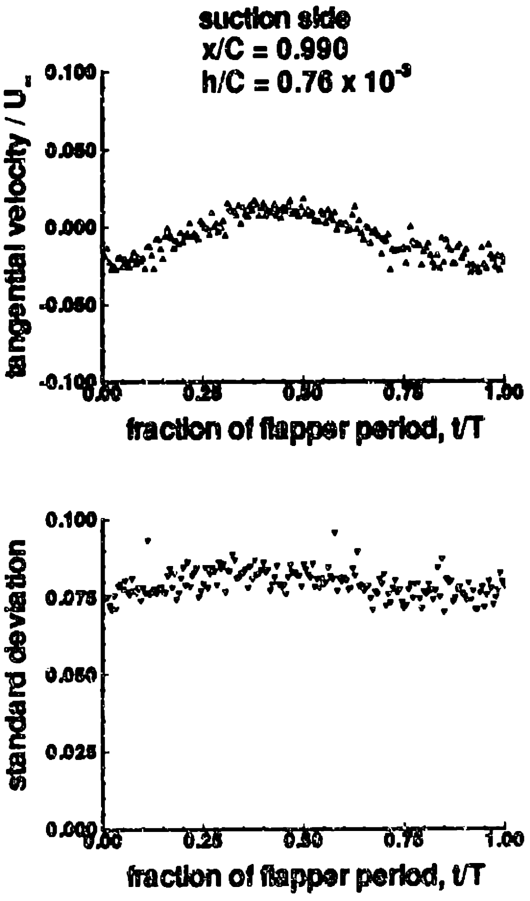

Figure 4-6: Time series of velocity very close to foil surface

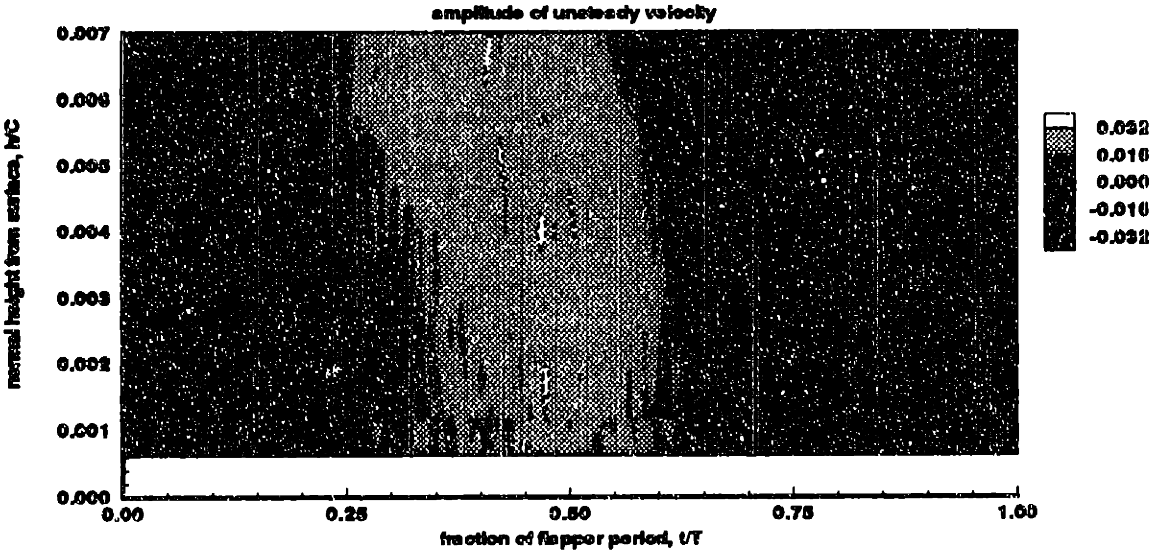

Figure 4-7: Time series of boundary layer velocity, $x/C = 0.388$, suction side

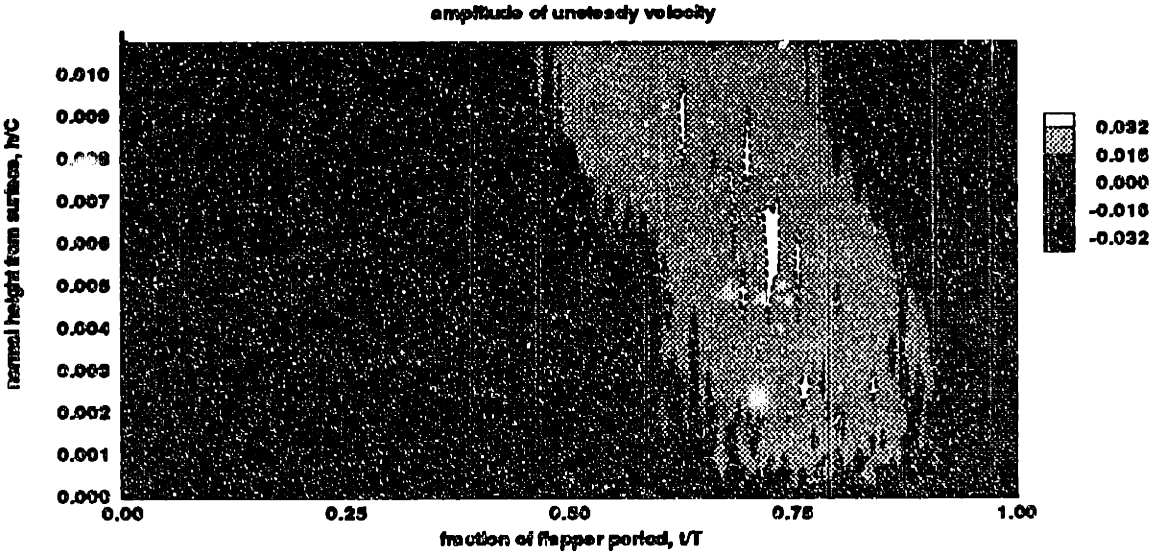

Figure 4-8: Time series of boundary layer velocity, $x/C = 0.612$, suction side

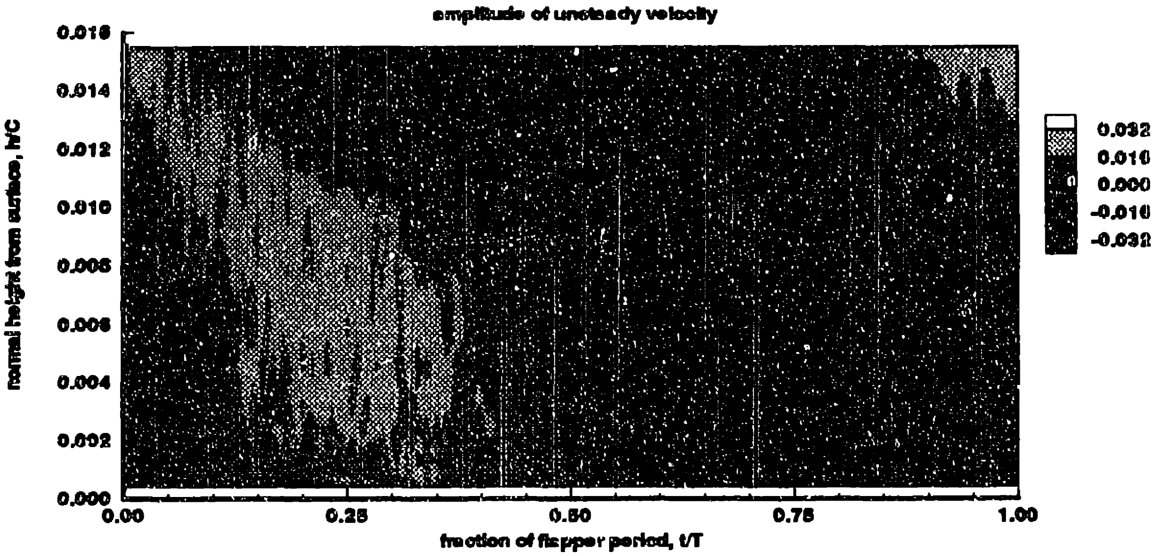

Figure 4-9: Time series of boundary layer velocity, $x/C = 0.900$, suction side

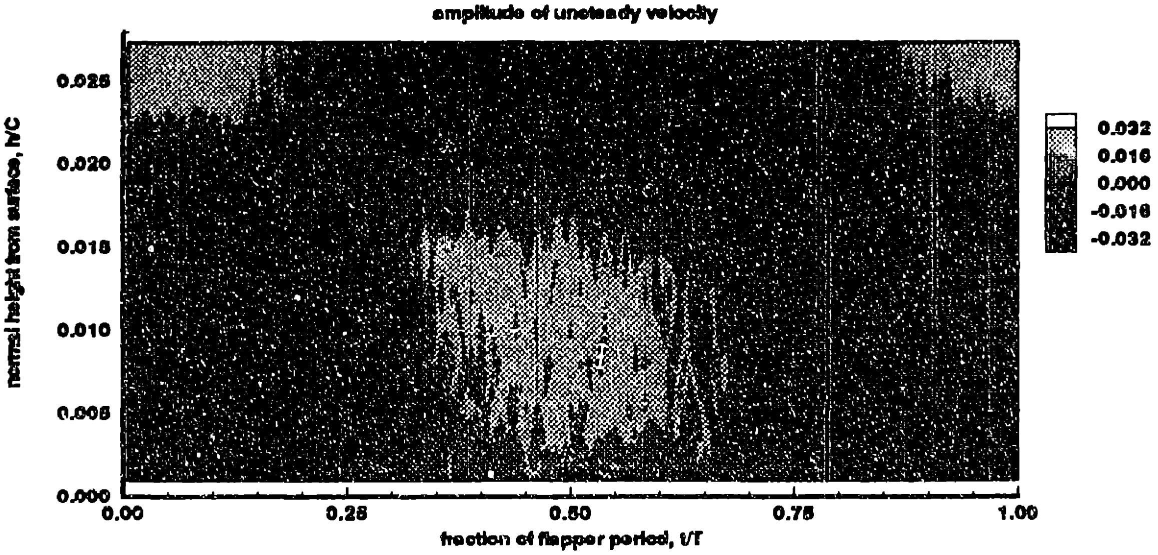

Figure 4-10: Time series of boundary layer velocity, $x/C = 0.972$, suction side

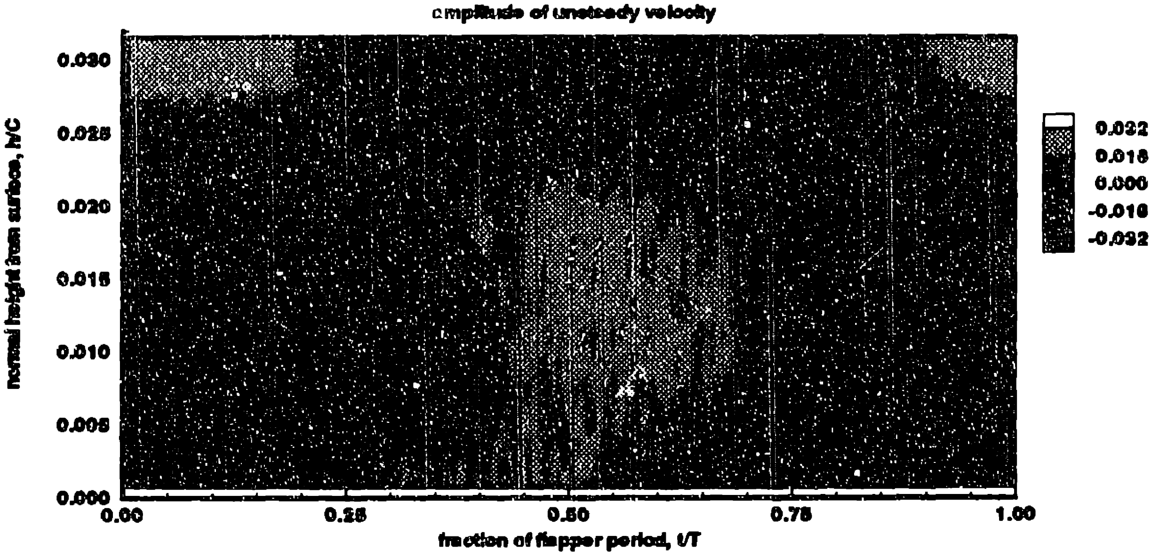

Figure 4-11: Time series of boundary layer velocity, $x/C = 0.990$, suction side

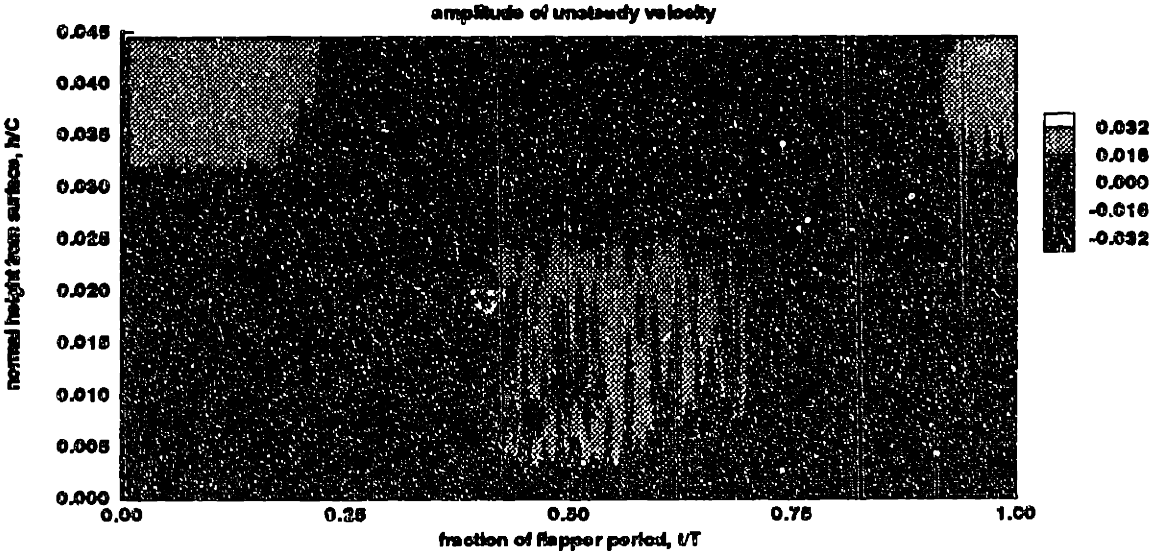

Figure 4-12: Time series of boundary layer velocity, $x/C = 1.00$, suction side

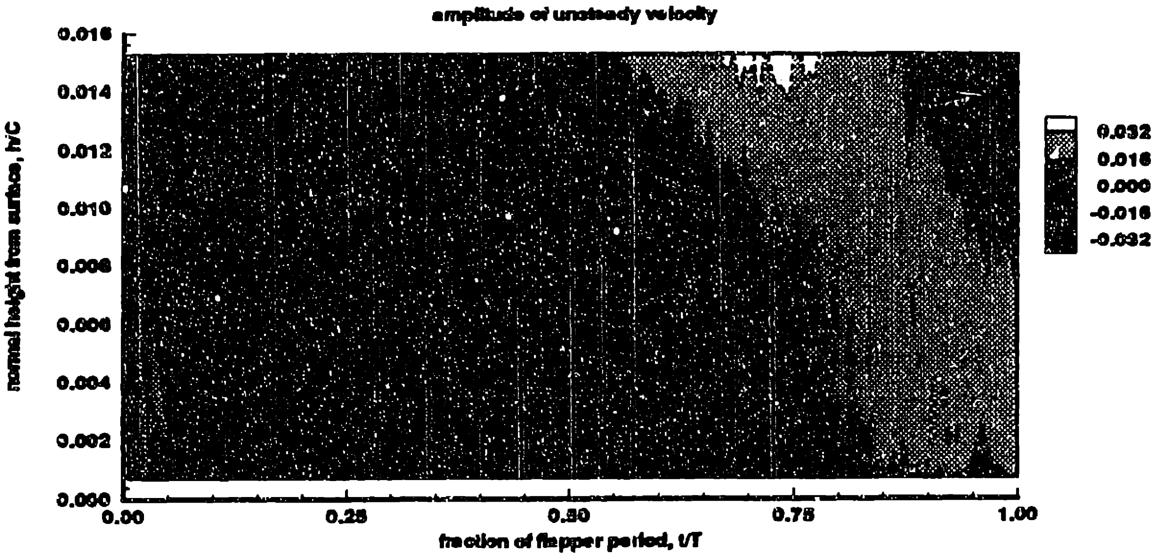

Figure 4-13: Time series of boundary layer velocity, $x/C = 0.972$, pressure side

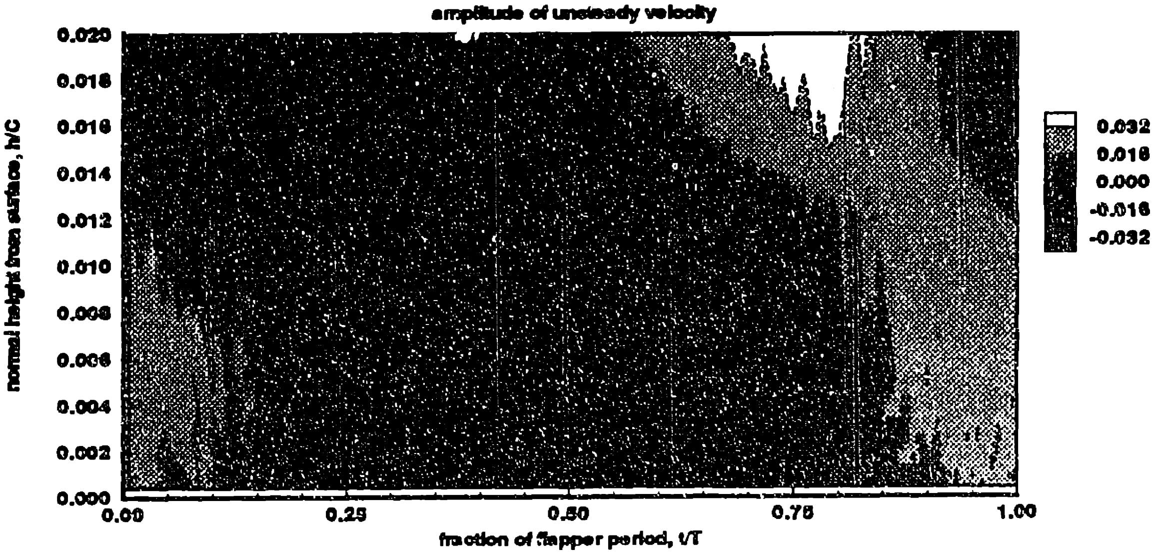

Figure 4-14: Time series of boundary layer velocity, $x/C = 1.00$, pressure side

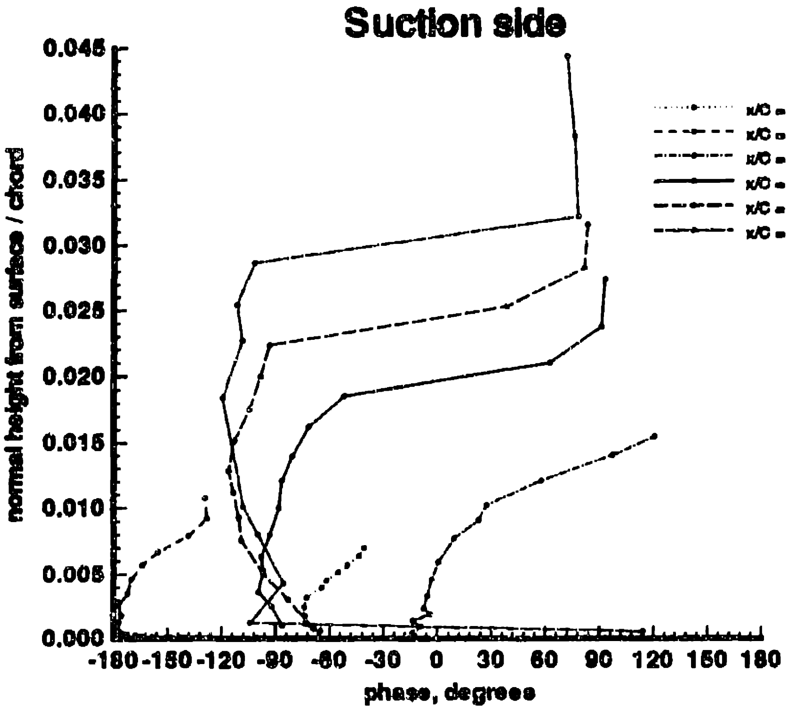

Figure 4-15: Phase of velocity gust through the boundary layer, suction side

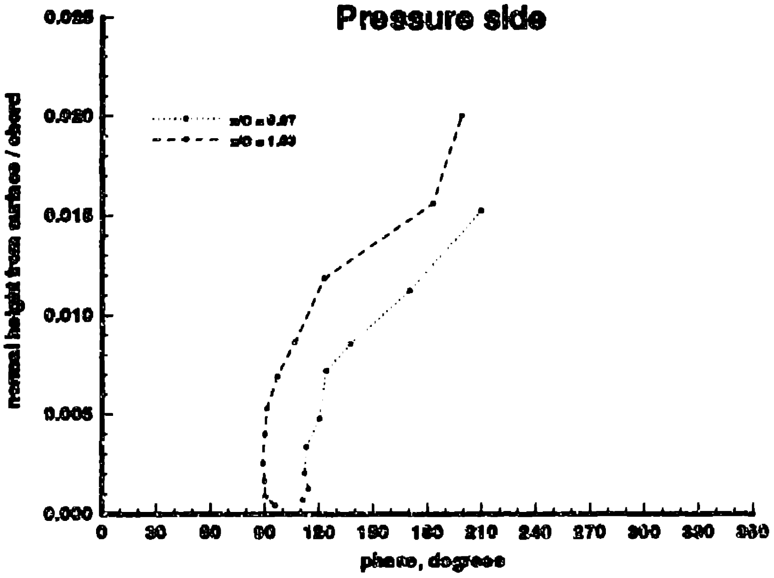

Figure 4-16: Phase of velocity gust through the boundary layer, pressure side

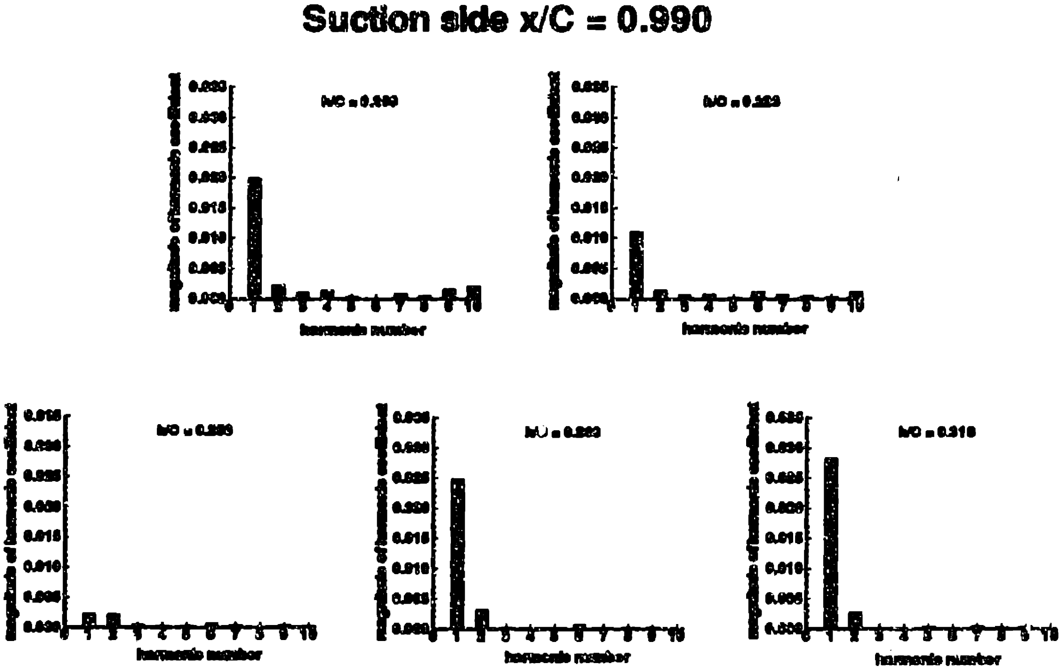

Figure 4-17: Harmonic content of boundary layer velocity at $x/C = 0.990$

The standard deviation of velocity through the boundary layer is an indication of turbulent activity. As in the steady flow case, there is an organized structure to the standard deviation everywhere. Not surprisingly, in some regions the standard deviation has some time dependence. Recall that a given velocity $u(t)$ can be decomposed into a mean component, $\overline{u}$, a periodic component, $\tilde{u}(t)$, and a random fluctuation, $u'(t)$; the ensemble average is then given by $< u(t) >= \overline{u} + \tilde{u}(t)$. The standard deviation of a set of N measurements is

$$\begin{aligned} \sigma^2 &= \frac{1}{N}\sum_{n=1}^{N}\left[u_n(t) - <u(t)>\right]^2 \\ &= \frac{1}{N}\sum_{n=1}^{N}\left[u'(t)\right]^2 \end{aligned} \tag{4.1}$$

Inspection of the unsteady data reveals that the standard deviation at some fixed point in space fluctuates with the same frequency as the outer flow; that is, the random disturbances tend to follow the periodic fluctuations of the outer flow fluctuations. In the upstream region on the suction side, $x/C = 0.388$ and $x/C = 0.612$, the time dependence is weak, and the largest deviations (or, largest amount of turbulent activity) take place near the foil surface (figures 4-18 and 4-19). Moving downstream, $x/C = 0.900$ through $x/C = 1.00$ on the suction side (figures 4-20 through 4-23), there is increased activity in a region somewhat displaced from the foil surface, as in the steady flow case. There is also a strong time dependence in this middle region and into the area where the gust amplitude has gone to zero. Close to the foil surface the time dependence is attenuated, as it is at the edge of the boundary layer.

Interestingly, the variation with time of the standard deviation is strongest on the pressure side (figures 4-24 and 4-25). Although the highest deviations are closest to the foil surface, there is a large time dependence throughout the boundary layer, except as the edge is reached.

The phase variation of the standard deviation through the boundary layer is not as large as the phase variation of the unsteady component of the total velocity (comparing figures 4-26 and 4-27 with 4-15 and 4-16). In those areas where the time dependence is very small, the measurement of a phase angle will not accurate, as is seen close to the foil surface.

Evidently there is a decoupling of the ensemble-averaged and random components of the boundary layer velocity: the amplitude of the random fluctutaions in unsteady external flow follows the same patterns as in steady external flow; that is, it is not affected by the imposed unsteadiness. Furthermore, the phase of the random fluctuations through the boundary layer does not vary with the phase of the unsteady part of the total velocity.

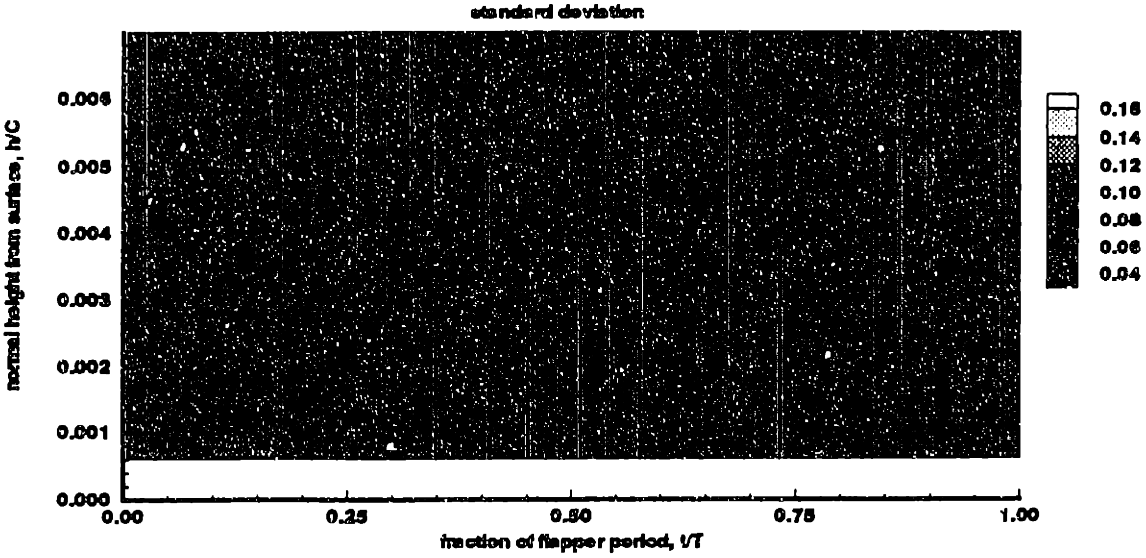

Figure 4-18: Standard deviation of velocity, $x/C = 0.388$, suction side

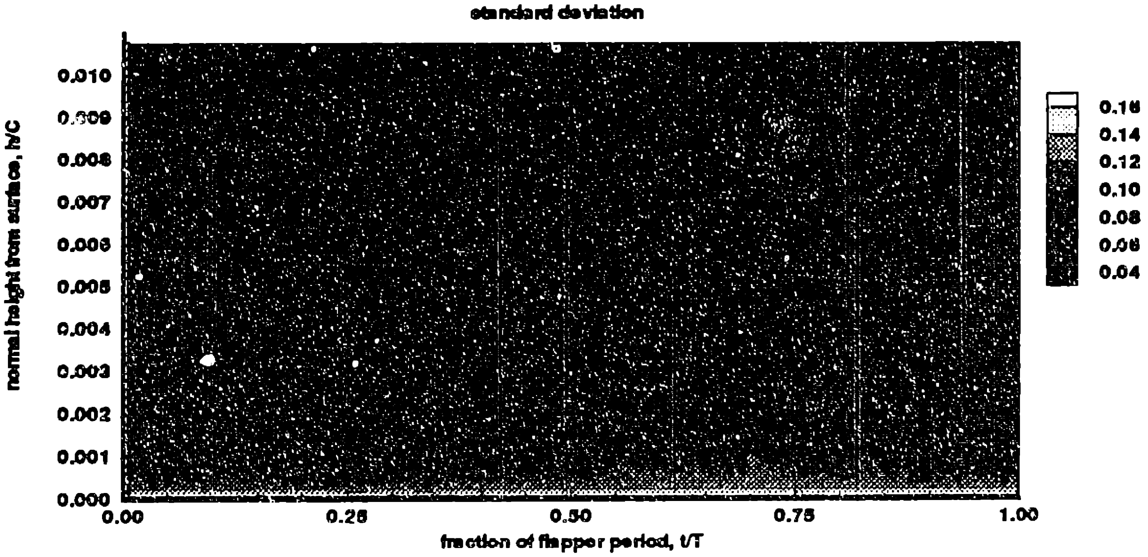

Figure 4-19: Standard deviation of velocity, $x/C = 0.612$, suction side

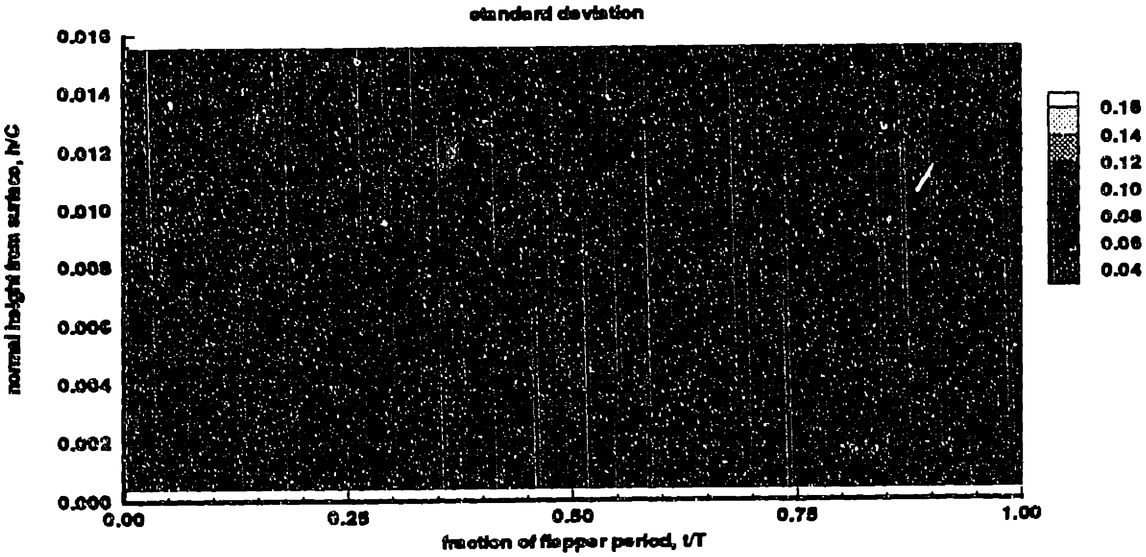

Figure 4-20: Standard deviation of velocity, $x/C = 0.900$, suction side

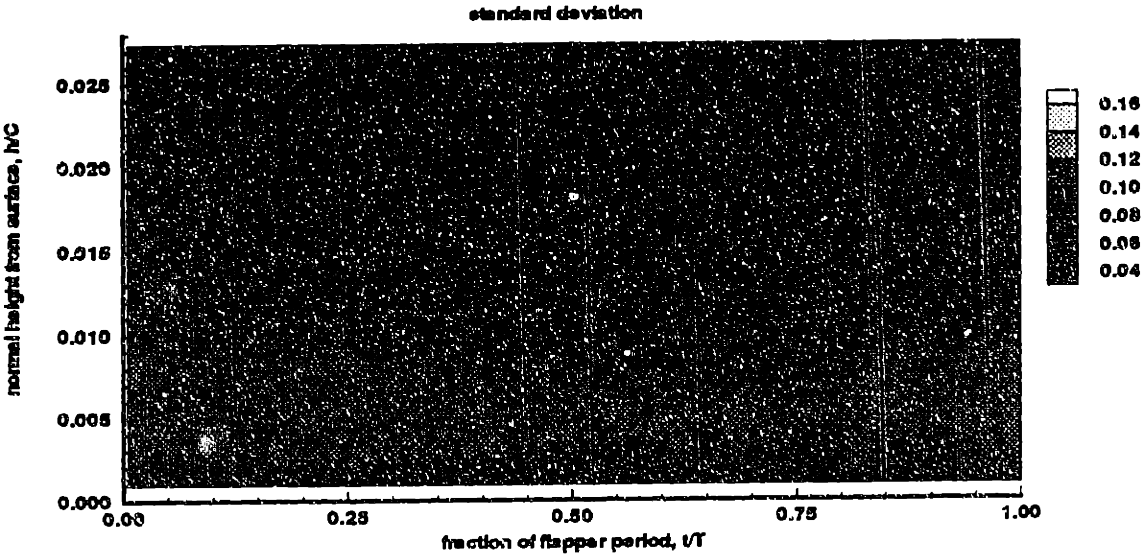

Figure 4-21: Standard deviation of velocity, $x/C = 0.972$, suction side

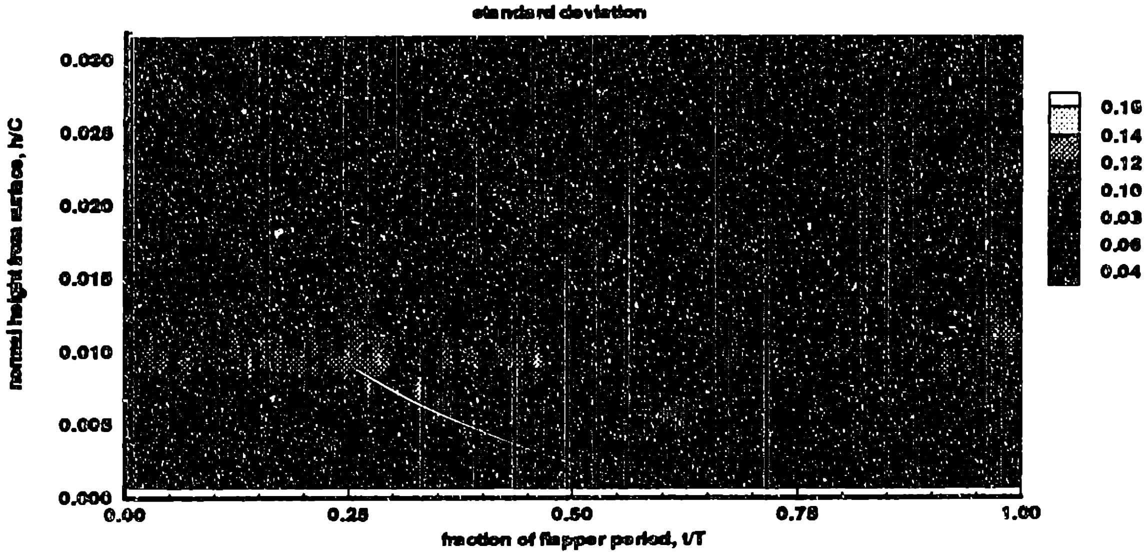

Figure 4-22: Standard deviation of velocity, $x/C = 0.990$, suction side

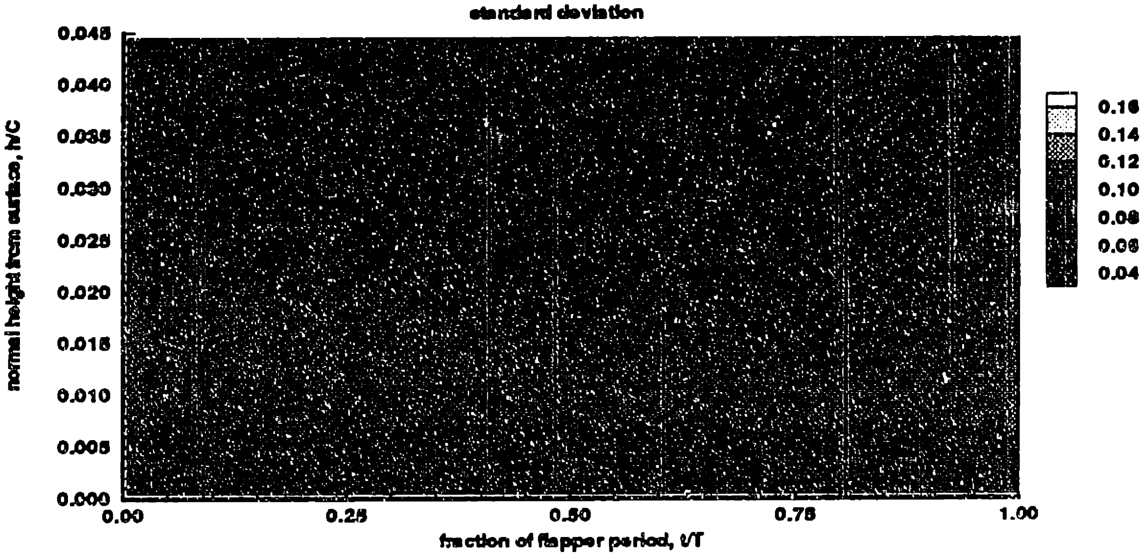

Figure 4-23: Standard deviation of velocity, $x/C = 1.00$, suction side

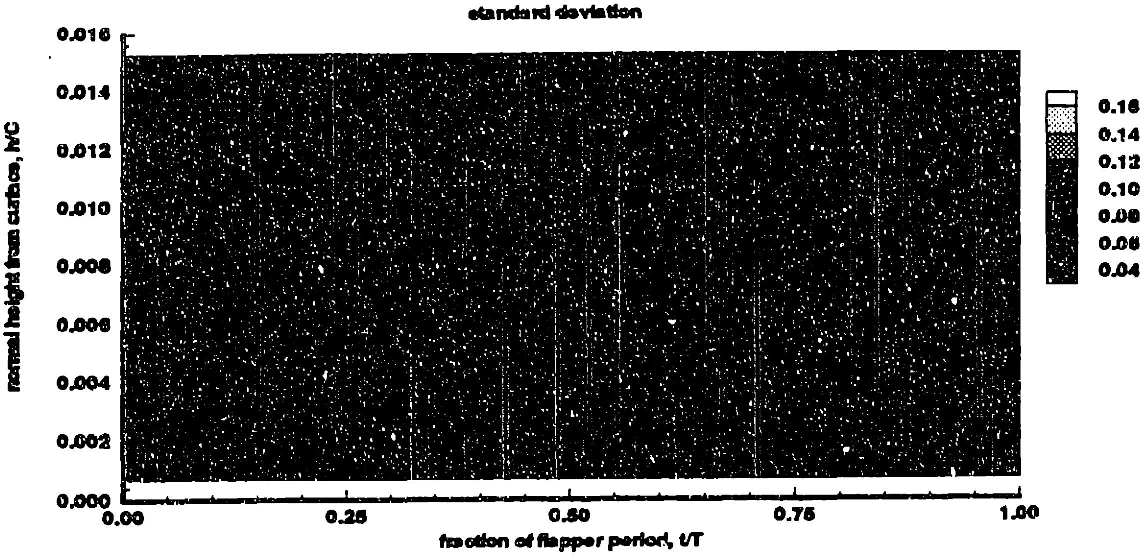

Figure 4-24: Standard deviation of velocity, $x/C = 0.972$, pressure side

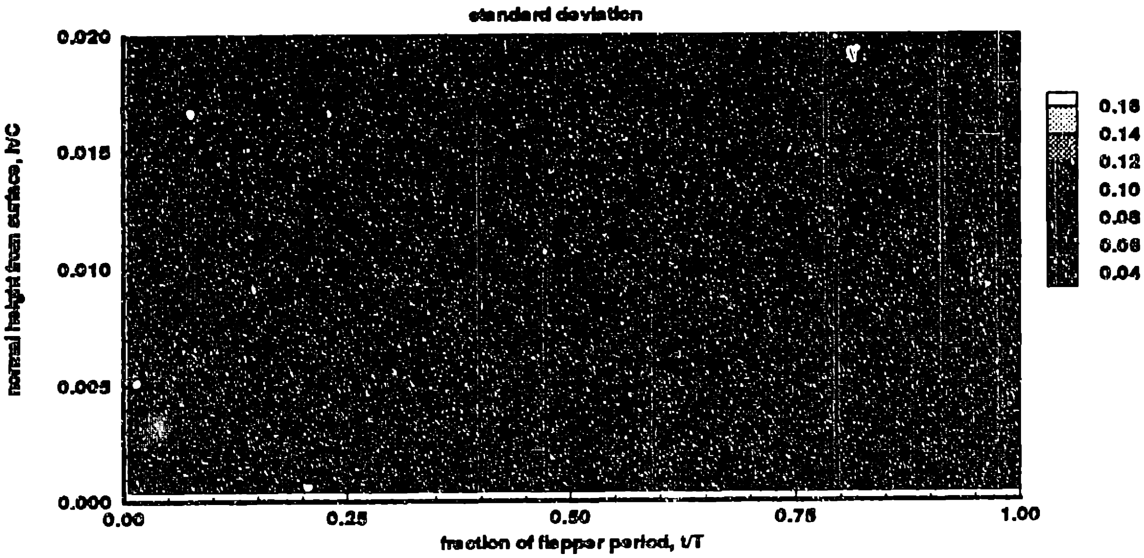

Figure 4-25: Standard deviation of velocity, $x/C = 1.00$, pressure side

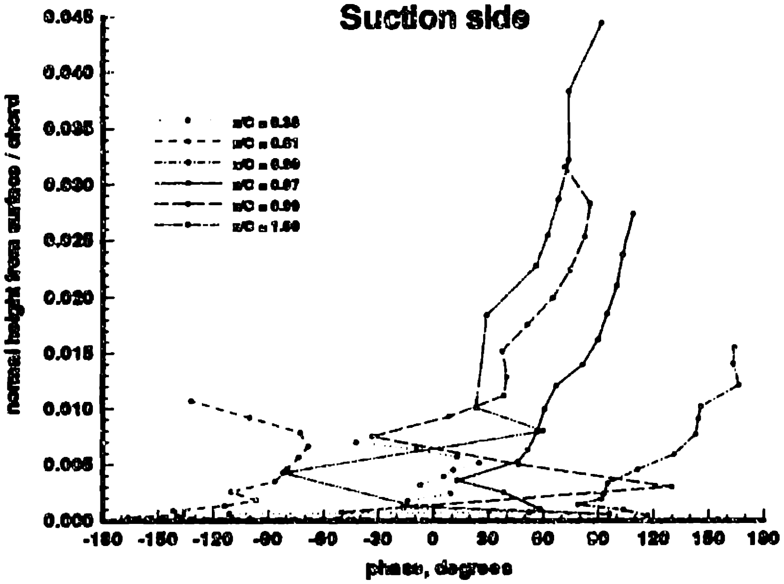

Figure 4-26: Phase variation of standard deviation through the boundary layer

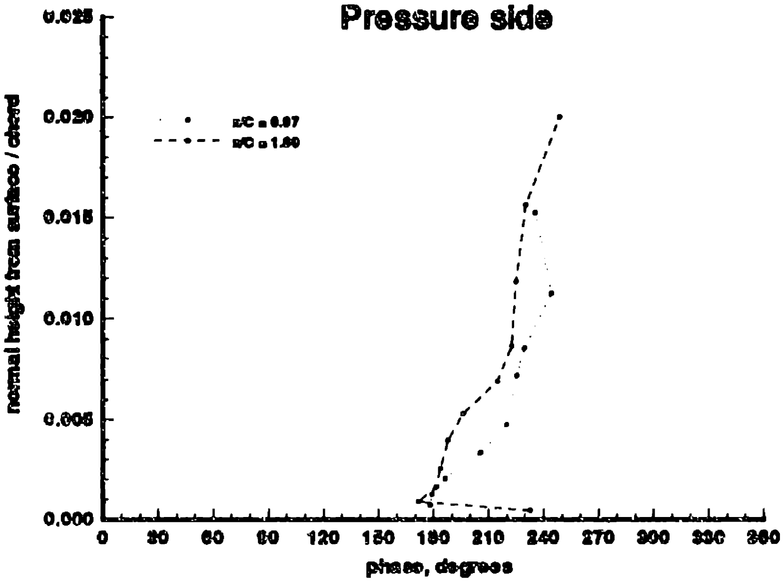

Figure 4-27: Phase variation of standard deviation through the boundary layer

4.3 Pressure Measurements

Surface pressure measurements were taken at four suction side and four pressure side locations. The time series can be seen in figures 4-28 through 4-35. What is interesting about the data is the strong presence of second harmonics. Given the smallness of the gust perturbation ($v/U_\infty = 0.022$) and the overwhelmingly first harmonic content of the boundary layer velocities, one might expect a primarily first harmonic surface pressure as well. Also, the harmonic content of the suction side trailing edge pressure data (figure 4-31) is filled with all sorts of higher harmonics. Recall that this is after separation in steady flow; in unsteady flow, the separated region is likely to be "walking" around this area.

The magnitude of the first ten harmonic coefficients of the surface pressure at the eight measurement locations are shown in figures 4-36 through 4-43.

Later experimentation was undertaken in order to determine if the source of the higher harmonic content of the surface pressure is mechanical, that is, is a resonance with the water tunnel, flapping foil drive system, or the like. Pressure data were taken with various parts of the system in operation: flappers on, tunnel impeller off; flapper motor on but flapper disconnected, impeller off; flapper motor off, impeller on; and so forth. None of these proved to be the pollutant. Later, an on-line Fourier analyzer was brought in in order to watch growth and decay of harmonic content while changing various parameters. Recall the definition of reduced frequency,

$$k = \frac{\omega c}{2U} = \frac{\pi f c}{U} \tag{4.2}$$

where, in this experiment, f is the flapper frequency and c is the chord length of the test hydrofoil. The reduced frequency was held constant by keeping the ratio f/U_∞ constant; the Reynolds number varied with U_∞. The harmonic content of the surface pressure is not significantly altered by changes in the Reynolds number, that is, by viscous effects. Pressure measurements were made while varying the flapper frequency and the freestream velocity through 25% of their original values.

A summary of this survey is shown in figure 4-44. The ratios of the magnitude of the second and fourth harmonic coefficient to the first peak around 15 Hz. In other words, the harmonic content of the surface pressure responds to the flapper or driving frequency, and not to the hydrodynamic parameter of reduced frequency. For this reason the possibility of the flappers exciting a mode of tunnel vibration seems the most likely source of the higher harmonics. One way to confirm this is to calibrate the pressure transducers in the water tunnel. This will be done in future experiments.

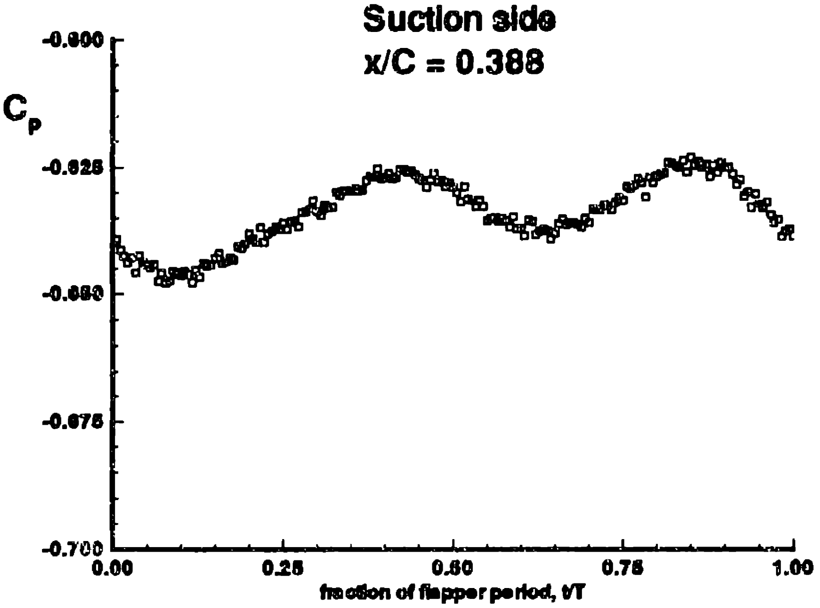

Figure 4-28: Time series of surface pressure, $x/C = 0.388$, suction side

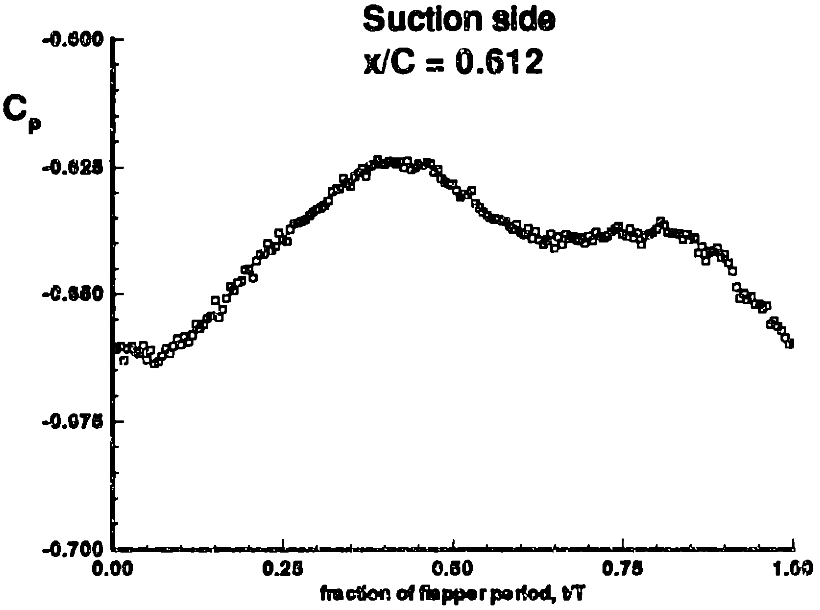

Figure 4-29: Time series of surface pressure, $x/C = 0.612$, suction side

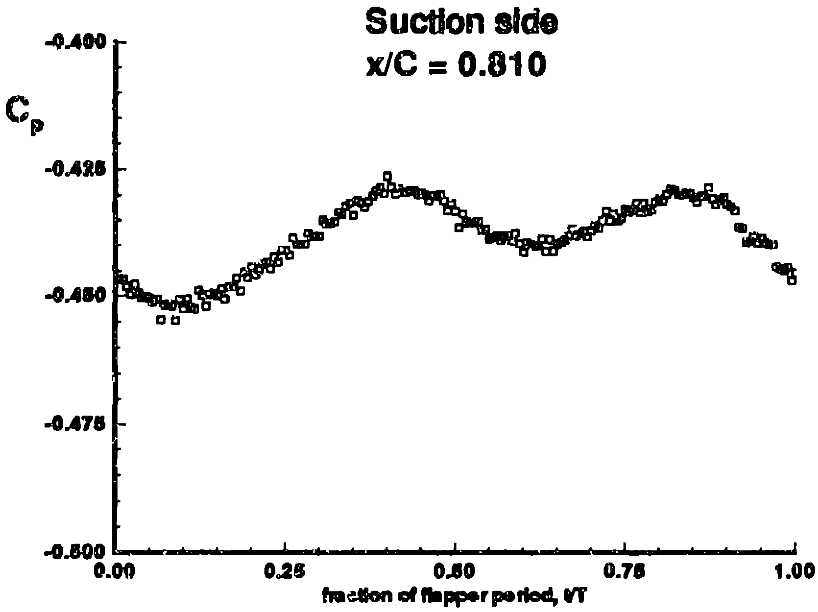

Figure 4-30: Time series of surface pressure, $x/C = 0.810$, suction side

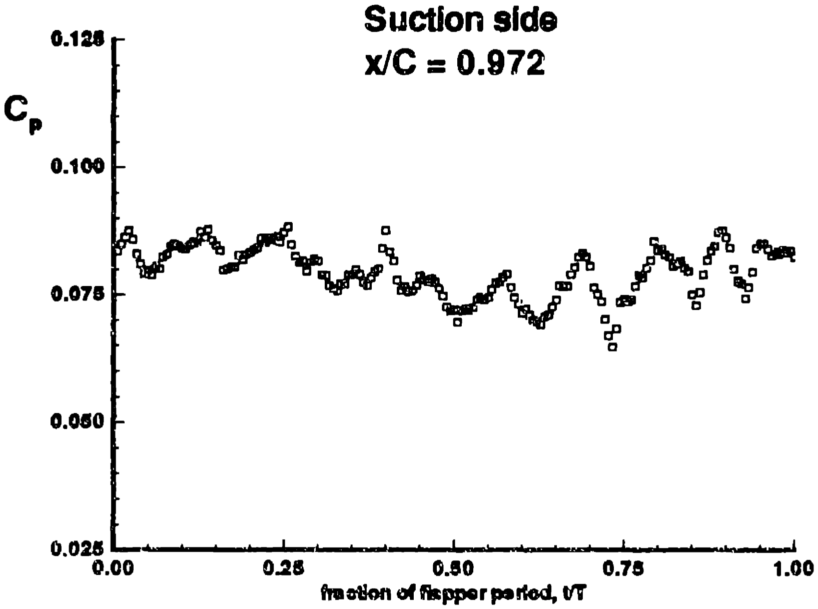

Figure 4-31: Time series of surface pressure, $x/C = 0.972$, suction side

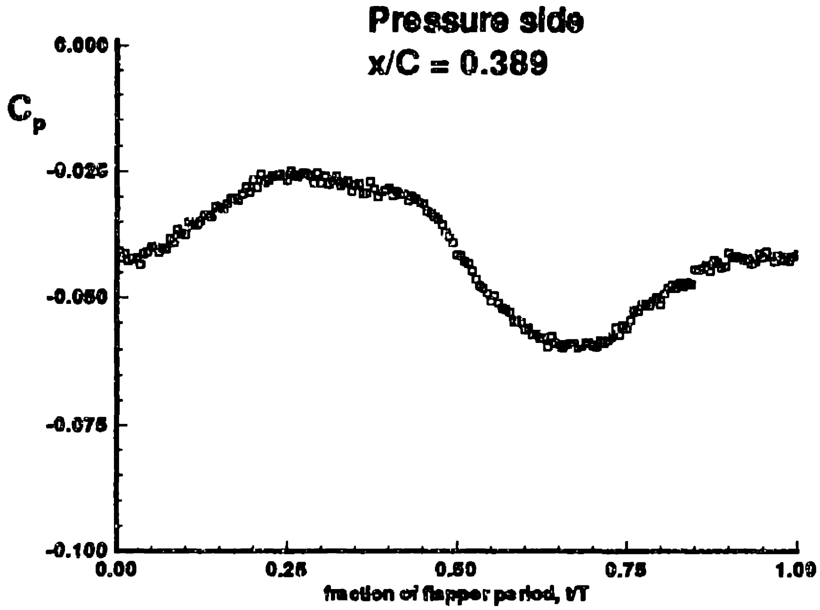

Figure 4-32: Time series of surface pressure, $x/C = 0.389$, pressure side

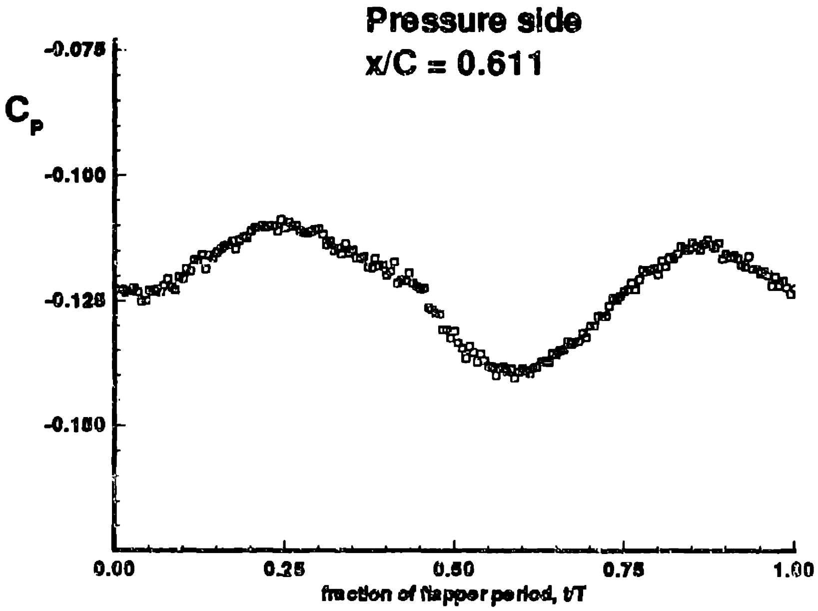

Figure 4-33: Time series of surface pressure, $x/C = 0.611$, pressure side

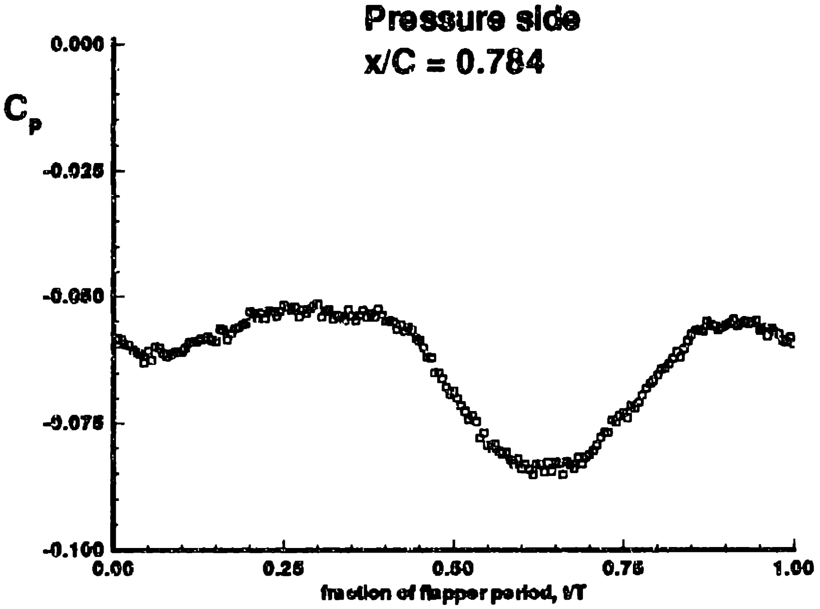

Figure 4-34: Time series of surface pressure, $x/C = 0.784$, pressure side

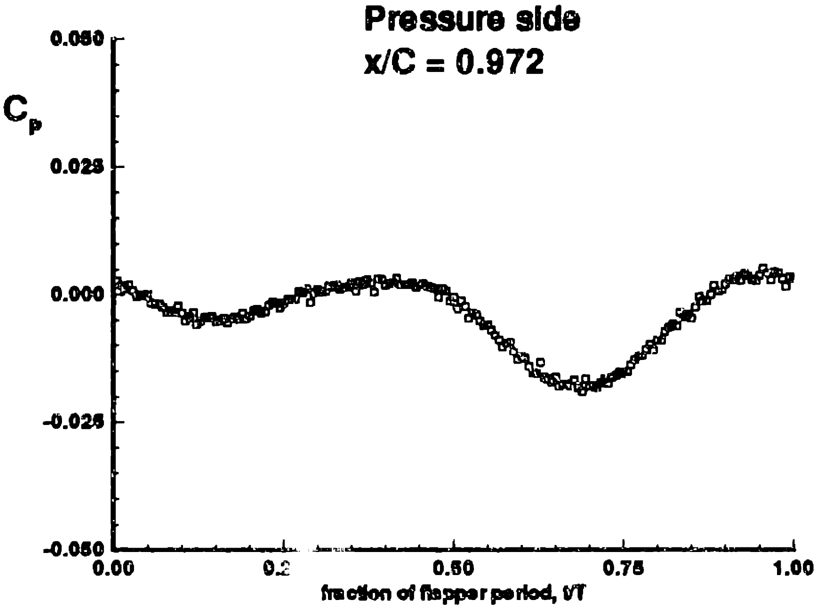

Figure 4-35: Time series of surface pressure, $x/C = 0.972$, pressure side

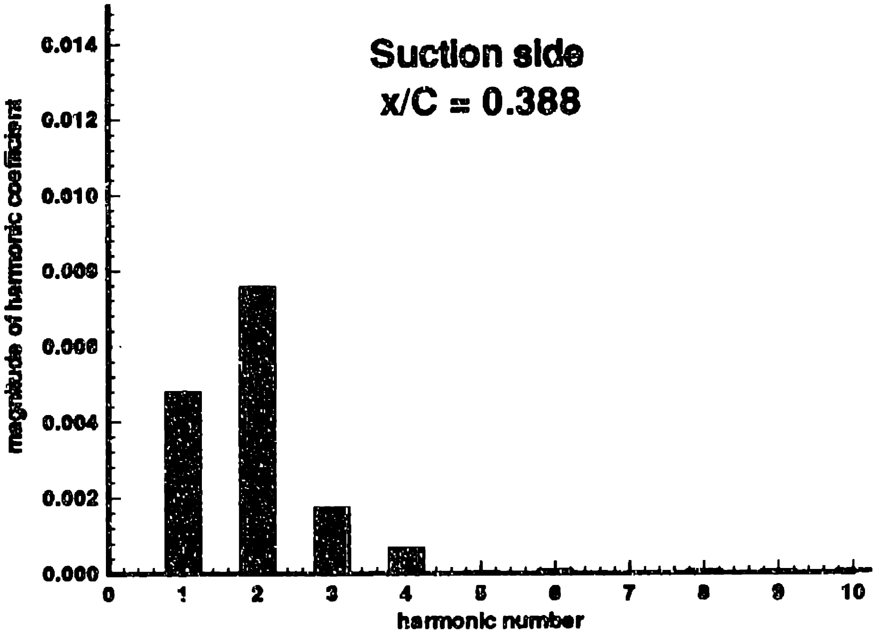

Figure 4-36: Harmonic content of surface pressure, $x/C = 0.388$, suction side

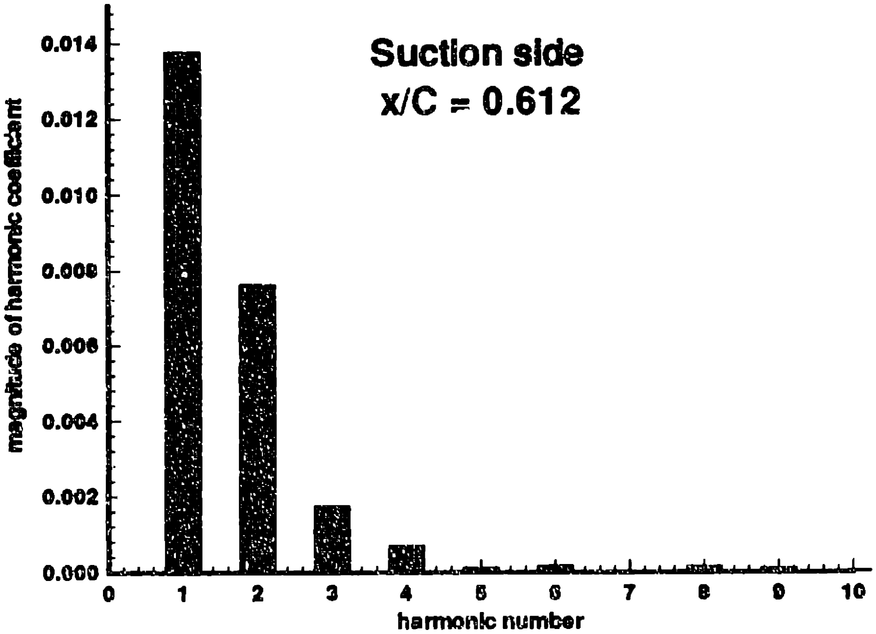

Figure 4-37: Harmonic content of surface pressure, $x/C = 0.612$, suction side

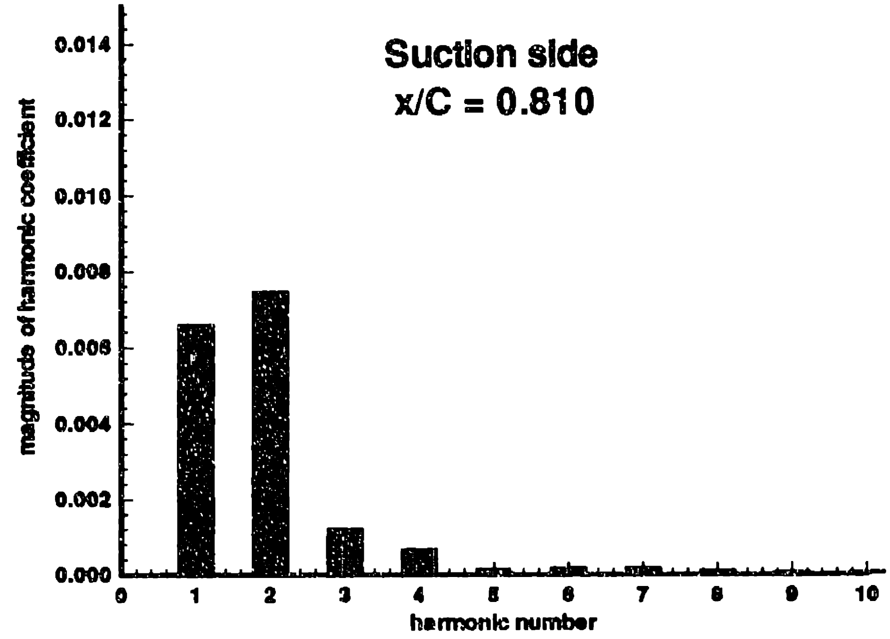

Figure 4-38: Harmonic content of surface pressure, $x/C = 0.810$, suction side

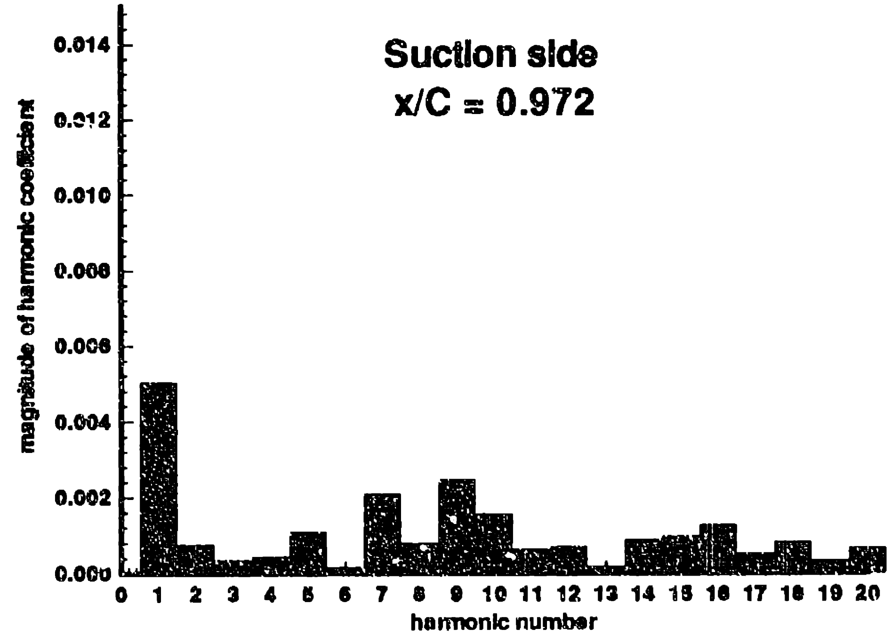

Figure 4-39: Harmonic content of surface pressure, $x/C = 0.972$, suction side

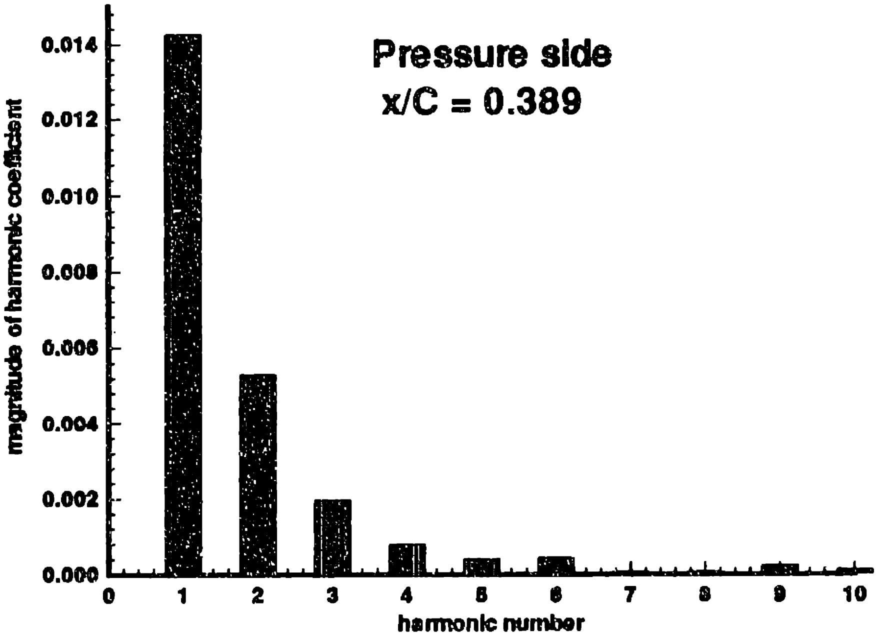

Figure 4-40: Harmonic content of surface pressure, $x/C = 0.389$, pressure side

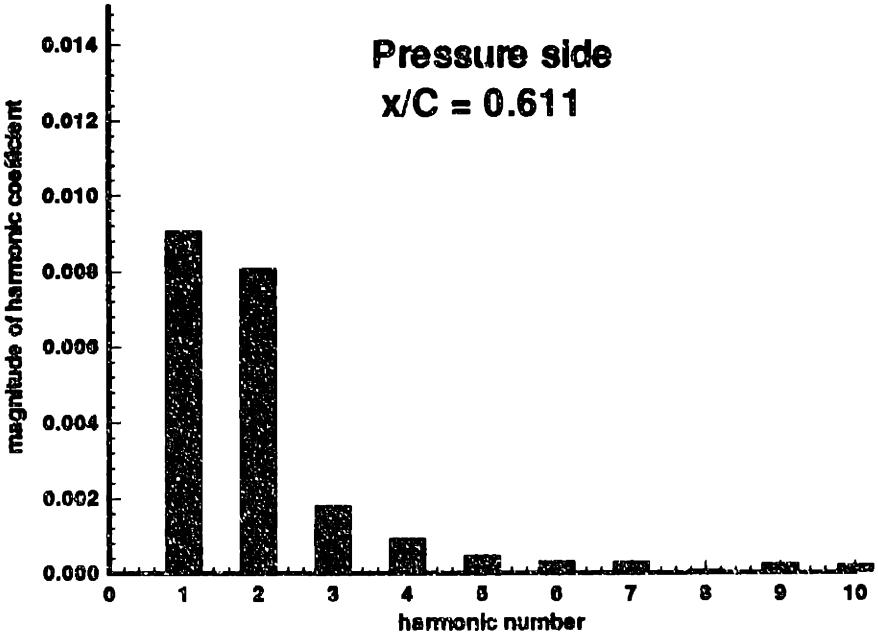

Figure 4-41: Harmonic content of surface pressure, $x/C = 0.611$, pressure side

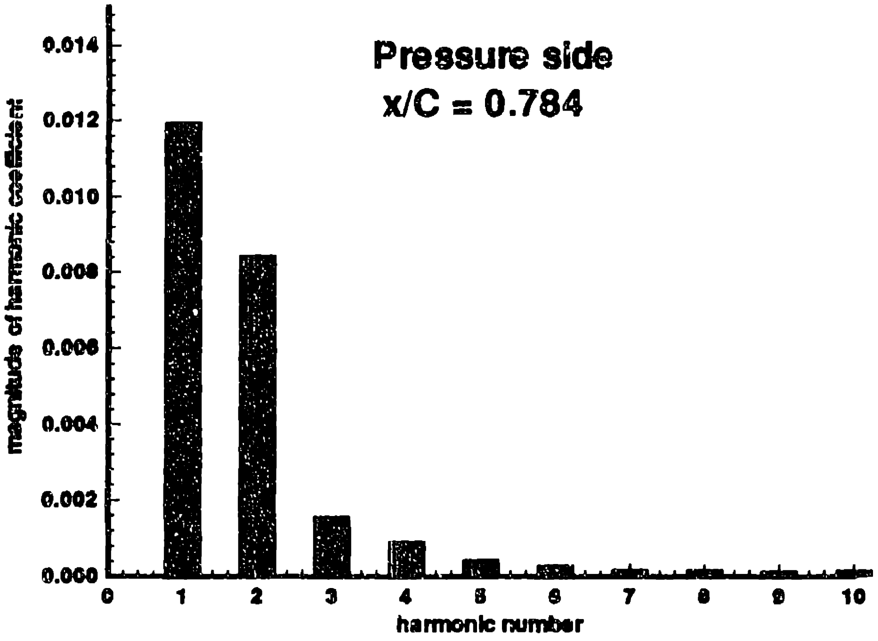

Figure 4-42: Harmonic content of surface pressure, $x/C = 0.784$, pressure side

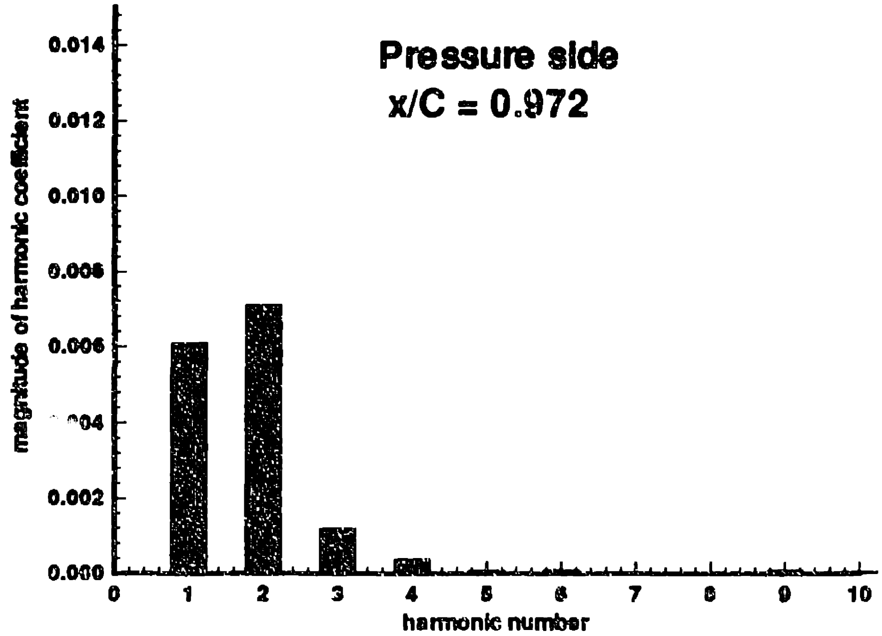

Figure 4-43: Harmonic content of surface pressure, $x/C = 0.972$, pressure side

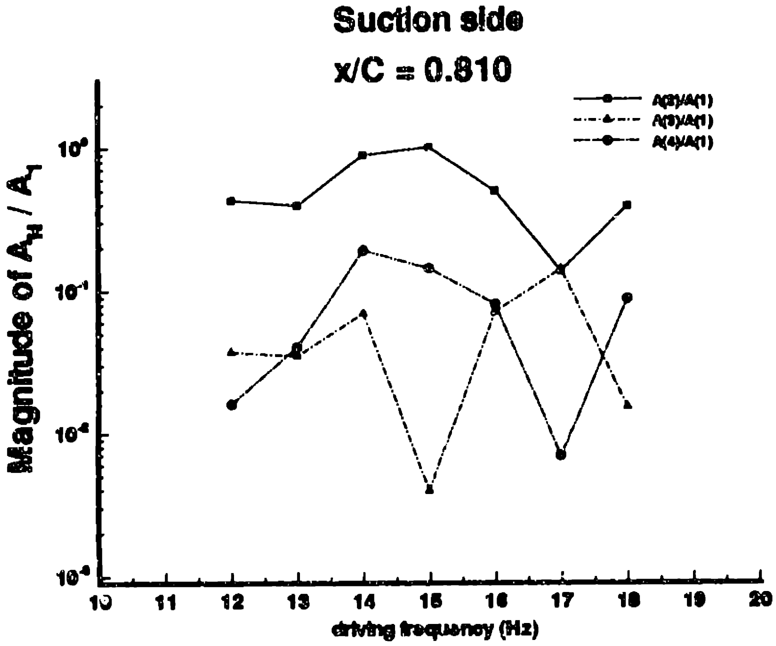

Figure 4-44: Survey of harmonic content of $C_p(t)$ with fixed $k = 3.6$

Chapter 5

Analysis and Discussion

In the previous chapters, detailed measurements of boundary layers, wakes, and surface pressures have been presented. In order to better understand the complex physics of the flow field, the measurements were analyzed along standard practices so that key properties would become evident. Also, comparisons were made between data and predictions from existing computational fluid dynamic codes in order to reveal the strengths and weaknesses of both the data and the numerical methods.

5.1 Steady Flow Boundary Layers

Inspection of the characteristic shapes of the steady flow boundary layer data revealed that the boundary layer trips were not successful on the pressure side for the case of $Re = 1.36 \times 10^6$ (figure 3-8). In order to confirm this observation, the data of the boundary layer profile at $x/C = 0.389$ were fit to a Falkner-Skan similarity profile. The Falkner-Skan similarity solution was developed for laminar boundary layers over wedges with constant pressure gradients; the edge velocity is given by $U_e \sim x^m$, where x is the streamwise coordinate and $\pi\left(\frac{2m}{m+1}\right)$ is the angle of the wedge [16, p. 152-157]. For example, flow over a flat plate has $m = 0$, and stagnation point flow has $m = 1$. The data were fit by choosing the value of m corresponding to a wedge of the angle corresponding to the slope of the test hydrofoil. The fit to the data can be seen in figure 5-1.

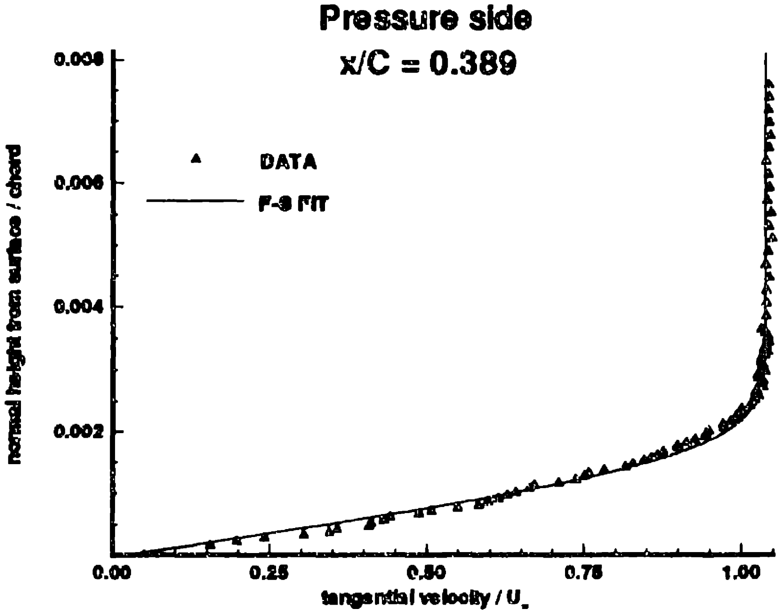

Figure 5-1: Falkner-Skan fit to boundary layer data, $x/C = 0.389$, pressure side

Comparison between boundary layers are often made in terms of integral parameters. The most common of these parameters are integral thicknesses based on the conservation of mass and momentum. Boundary layers act to displace the streamlines in the flow outside the boundary layer; the displacement thickness, δ^*, is defined as the distance by which the body surface would have to be extended in order maintain the same flow rate in a hypothetical inviscid flow. For steady, incompressible flow,

$$\delta^* = \int_0^\infty \left(1 - \frac{u}{U_e}\right) dy \tag{5.1}$$

where U_e is the velocity at the edge of the boundary layer. The displacement thickness is often used as a normalizing factor, since the actual boundary layer thickness is often difficult to measure. The momentum thickness, θ, represents the momentum loss due to the presence of the boundary layer and is proportional to the drag when no streamwise pressure gradient exists. Many empirical correlations use the momentum thickness. It is defined as

$$\theta = \int_0^\infty \left(\frac{u}{U_e}\left(1 - \frac{u}{U_e}\right)\right) dy \tag{5.2}$$

The shape factor, H, describes the shape of the velocity profile. It is defined as

$$H = \frac{\delta^*}{\theta} \tag{5.3}$$

Typical values for the shape factor based on approximate integral solutions of the boundary layer equations are H between 2.3 and 3.5 for laminar boundary layers, and H between 1.3 and 2.2 for turbulent boundary layers. Turbulent separation takes place at H near 2.2 [16, p. 212 and p. 675].

The integral parameters of the steady flow boundary layer data were obtained by integrating the data using a trapezoidal rule. For the turbulent boundary layers, the "missing" inner layer data were approximated by a $\frac{1}{7}$th power law,

$$\frac{u}{U_e} = \left(\frac{y}{\delta}\right)^{\frac{1}{7}} \tag{5.4}$$

Although this approximation is based on zero pressure gradient, it was found to contribute less than 2% of the displacement thickness in regions of adverse pressure gradient. Similarly, errors are introduced in trying to integrate at locations where sparse data were measured near the surface; for this reason, the data from the suction side, $Re = 3.78 \times 10^6$, $x/C = 0.700$, were not analyzed. For the one laminar boundary layer, the inner data were approximated by the Falkner-Skan fit. The resulting intgeral parameters can be seen in figures 5-2 through 5-5. Evidence that separation has occurred is found in the rapid growth in shape factor over the trailing edge (table 5.1).

x/C	$Re = 1.36 \times 10^6$	$Re = 3.78 \times 10^6$
0.900	1.612	1.574
0.950	1.973	1.891
0.972	2.438	2.444
0.990	3.138	3.250
1.000	3.535	3.835

Table 5.1: Change in shape factor H near trailing edge, suction side

Turbulent boundary layers also exhibit self-similar characteristics. Dividing a turbulent boundary layer profile into different regions, the innermost region is dominated by viscous shear and is self-similar for all turbulent boundary layers. This region is called the viscous sublayer and is described by

$$\frac{u}{u_\tau} = \frac{y\,u_\tau}{\nu} \tag{5.5}$$

where u_τ is the friction velocity, $u_\tau = \sqrt{\tau_w/\rho}$, and τ_w is the wall shear stress. Outside of the sublayer but still very close the the wall, the velocity is logarithmic with distance and is given by

$$\frac{u}{u_\tau} = \frac{1}{\kappa}\ln\left(\frac{y\,u_\tau}{\nu}\right) + \beta \tag{5.6}$$

where κ and β are emprical constants. Turbulent shear dominates viscous shear in the logarithmic region. Together the viscous sublayer, the logarithmic layer, and the buffer region between the two are called the "law of the wall." Generally this region exists over the inner 10% of the boundary layer thickness. Streamwise pressure gradients have no effect on this region. In order to confirm that the boundary layer had been tripped to turbulence, the steady boundary layer data was converted into the coordinates $u^+ = u/u_\tau$ and $y^+ = (yu_\tau)/\nu$ and compared with the universal profile. Discussion of the determination of u_τ will follow.

Lacking direct measurement, one can use empirical methods to determine the wall shear stress or its nondimensional counterpart, the skin friction coefficient $C_f = \tau_w/(\frac{1}{2}\rho U_e^2)$. One can attempt to use the slope of the velocity profile at the wall to evaluate τ_w, but this does not lead to accurate results; the profile has extremely large curvature for small y/δ [15]. Another method is to combine equation (5.6) and the definitions of the friction velocity and the skin friction coefficient in a parametric form with C_f as the parameter:

$$\frac{u}{U_e}\sqrt{\frac{2}{C_f}} = \frac{1}{\kappa}\ln\sqrt{\frac{C_f}{2}}\frac{U_e y}{\nu} + \beta \tag{5.7}$$

This equation is then plotted for a range of values of C_f, and the experimental data is overlaid. The shear stress is read off by examining the measurements close to the wall where the law of the wall is expected to apply. Such a graph is called a "Clauser chart."

Because of the error associated with knowing exactly where the hydrofoil surface is, it was felt that using a Clauser chart would not give accurate results. Instead, an empirical relation was used, given by Swafford [21, p. 451]. For turbulent boundary layers,

$$\begin{aligned} C_f &= 0.3\,e^{-1.33H}\left(\frac{\log_{10} Re_\theta}{2.3026}\right)^{-1.74-0.31H} \\ &\quad + 1.1\times 10^{-4}\left[\tanh\left(4.0-\frac{H}{0.875}\right)-1.0\right] \end{aligned} \tag{5.8}$$

where $Re_\theta = (U_e\theta)/\nu$. This empirical relation is considered accurate to ±3%. At locations where sparse data were measured near the surface, an empirical relation based on the integrated quantites θ and H will not give accurate results. For the one laminar boundary layer, the skin friction coefficient was extracted from the Falkner-Skan fit to the data. Figures 5-6 and 5-7 show the calculated values of the skin friction coefficient. Using Swafford's formula, separation is predicted between $x/C = 0.972$ and $x/C = 0.990$ for both Reynolds numbers. Discrepancies exist in the location of the separation point due to errors in estimates of the momentum thickness θ and the shape factor H.

Using the values of the skin friction coefficient predicted by Swafford's formula (5.8), the friction velocity u_τ is known, allowing the conversion of turbulent boundary layer data into typical u^+ versus y^+ coordinates. This can be done with confidence only in those places where both the location of the hydrofoil surface and the skin friction coefficient are known with confidence; that is, away from the separation region. A few representative profiles can be seen in figures 5-8 through 5-11. This verifies that the measured boundary layers are turbulent everywhere at the high Reynolds number; for the low Reynolds number experiment, only the pressure side $x/C = 0.389$ boundary layer is laminar; by $x/C = 0.611$ the characteristic turbulent profile is seen (figure 5-9).

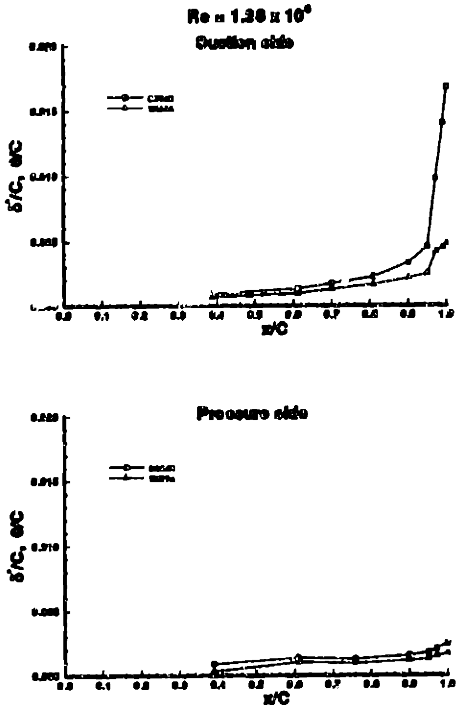

Figure 5-2: δ^*/C, θ/C vs. x/C, $Re = 1.36 \times 10^6$

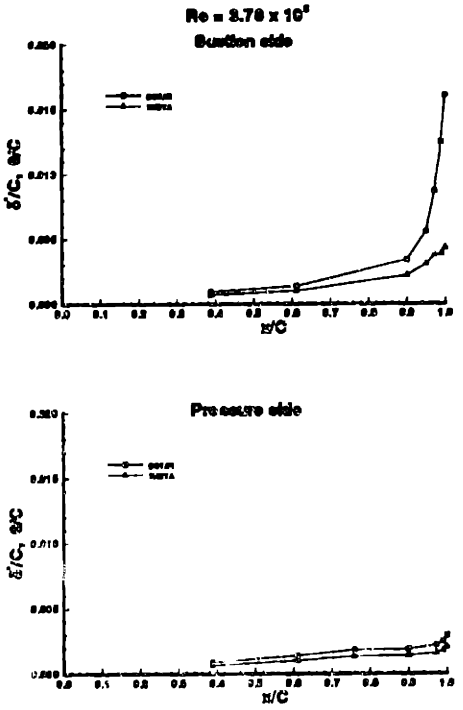

Figure 5-3: δ^*/C, θ/C vs. x/C, $Re = 3.78 \times 10^6$

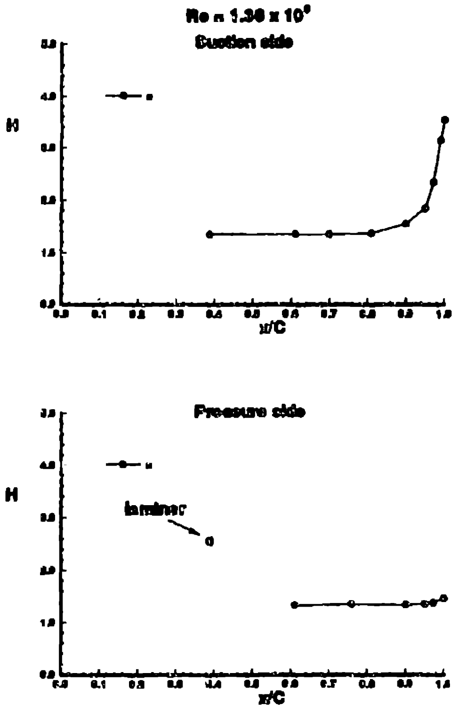

Figure 5-4: Shape factor H vs. x/C, $Re = 1.36 \times 10^6$

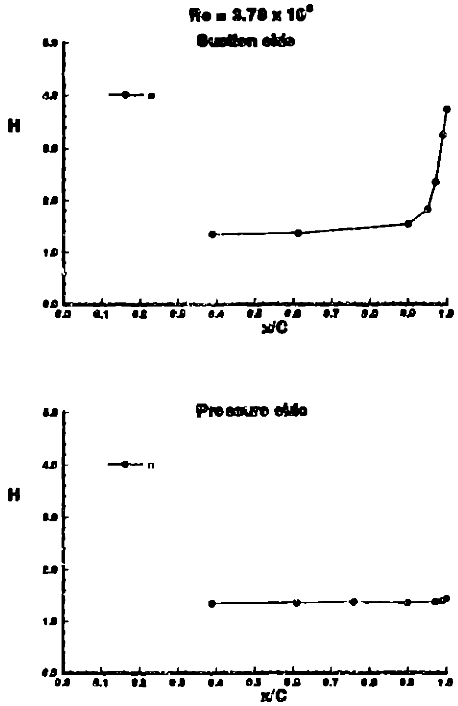

Figure 5-5: Shape factor H vs. x/C, $Re = 3.78 \times 10^6$

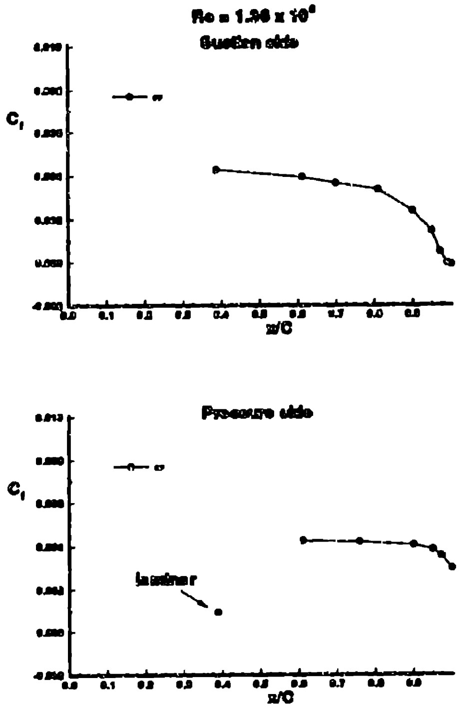

Figure 5-6: Skin friction coefficient vs. x/C, $Re = 1.36 \times 10^6$

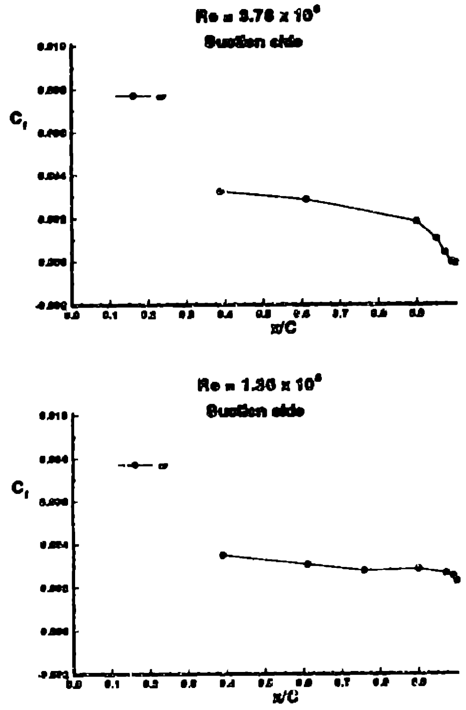

Figure 5-7: Skin friction coefficient vs. x/C, $Re = 3.78 \times 10^6$

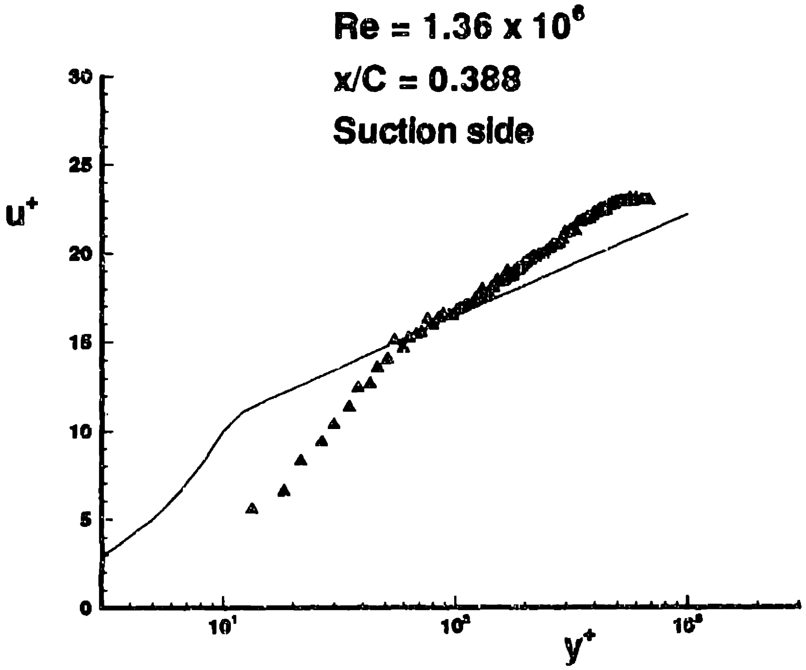

Figure 5-8: Boundary layer data in u^+, y^+ coordinates

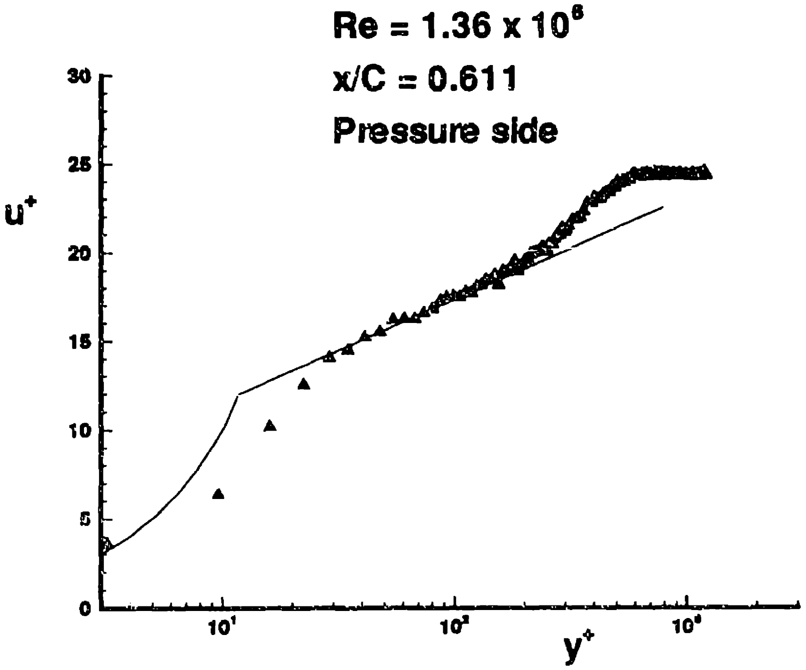

Figure 5-9: Boundary layer data in u^+, y^+ coordinates

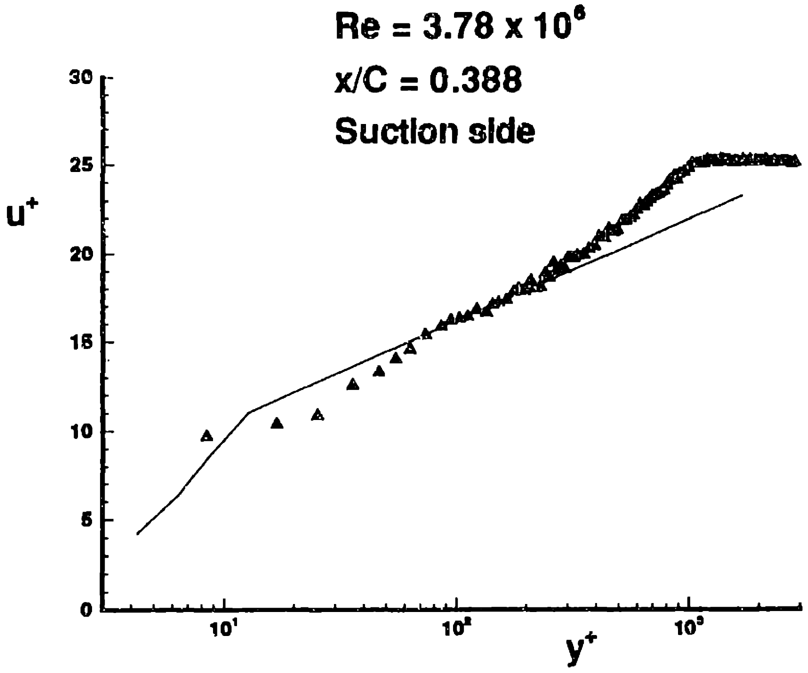

Figure 5-10: Boundary layer data in u^+, y^+ coordinates

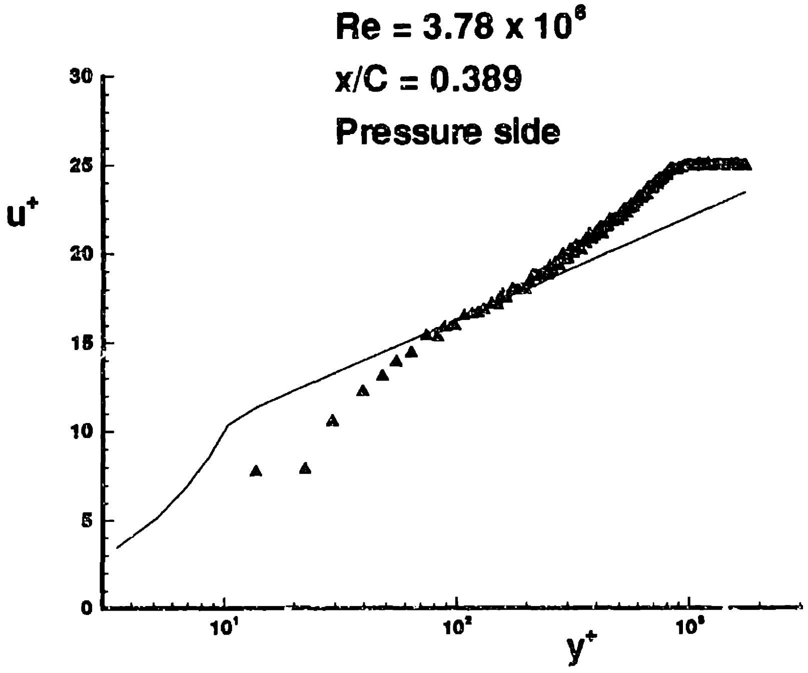

Figure 5-11: Boundary layer data in u^+, y^+ coordinates

5.2 Comparison with Steady Flow Panel Code

Data such as that collected in the Flapping Foil Experiment are valuable tools to those who develop computational fluid dynamics codes. Furthermore, comparison with well established numerical methods provides a "reality check" for the data.

P2D-BLWC is a two-dimensional strongly coupled viscous-inviscid solver [20]. The method is based on a low order perturbation potential formulation. Coupling of both the cavitating and viscous portions of the flow is implemented through the use of blowing sources. The viscous solver uses integral techniques developed by Drela [3]. The water tunnel walls are modelled using images.

Calculations for the $Re = 1.36 \times 10^6$ case steady flow case were not performed because P2D-BLWC did not converge without specification of the location of transition on the pressure side. For the $Re = 3.78 \times 10^6$ case, the boundary layer was assumed to have been tripped at $x/C = 0.105$, the same location as the trips on the test hydrofoil. The turbulence level of the freestream velocity was set as 1%. The tunnel walls were simulated by using twenty images. The comparison between measured and calculated lift and drag coefficients is given in table 5.2.

	C_L	C_D
experiment	0.466	0.0101
P2D-BLWC	0.644	0.00926

Table 5.2: Comparison of lift and drag coefficients, experiment vs. P2D-BLWC

P2D-BLWC tends to underpredict the edge velocities along the lower surface of the hydrofoil (figure 5-12), and as a result it overpredicts the surface pressure over the chord (figure 5-13) and the lift coefficient. Nevertheless, the comparison with integrated quantities is quite favorable (figures 5-14 and 5-15). P2D-BLWC calculates the separation point on the suction side to be at $x/C = 0.98$.

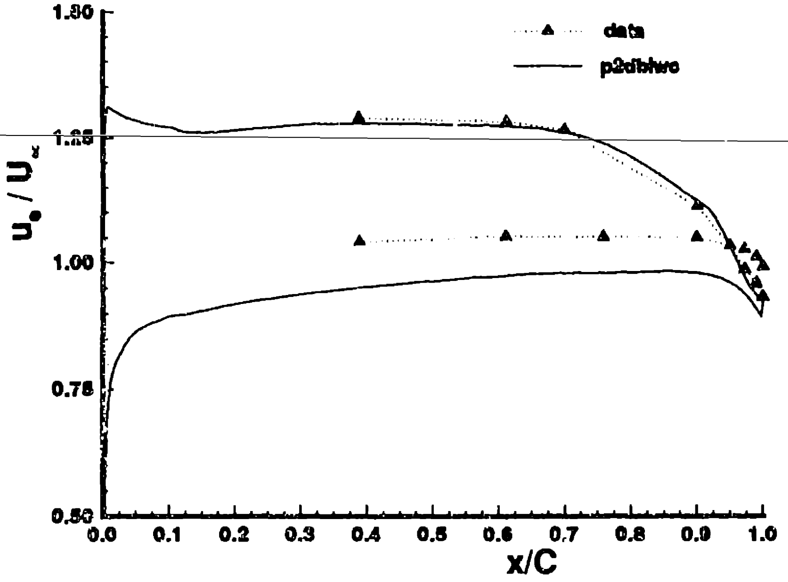

Figure 5-12: Comparison of edge velocities, experiment vs. P2D-BLWC

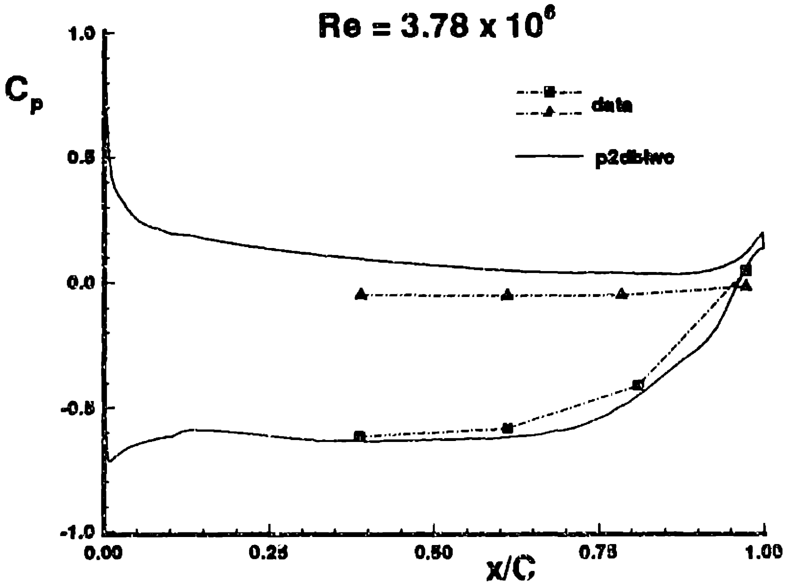

Figure 5-13: Comparison of surface pressure, experiment vs. P2D-BLWC

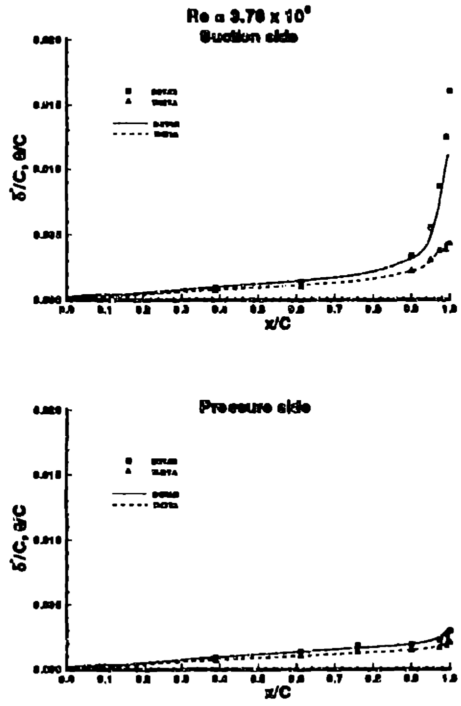

Figure 5-14: Comparison $\delta^*/C, \theta/C$, experiment vs. P2D-BLWC

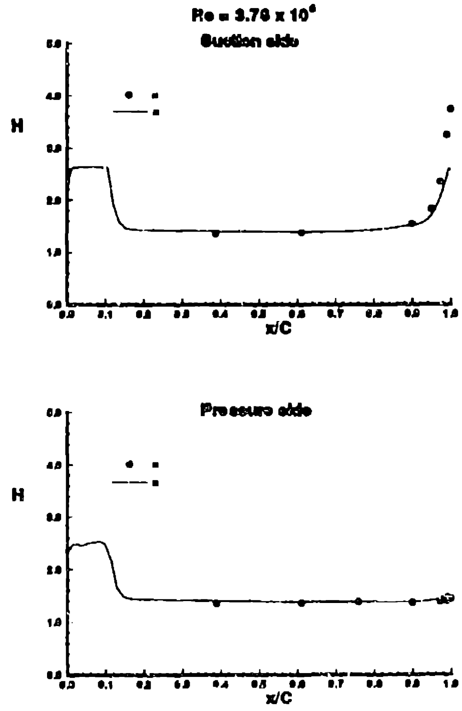

Figure 5-15: Comparison of shape factor, experiment vs. P2D-BLWC

5.3 Steady Flow Wakes

One of long range goals of the Flapping Foil Experiment is to study the local behavior of the flow field near the trailing edge. Steady flow wake measurements provide a base for later unsteady measurements. The streamlines emanating from the test hydrofoil in steady flow are shown in figure 5-16. Because only one component of velocity was measured at and upstream of $x/C = 1.00$, the streamline emanating from stagnation point near the trailing edge could not be found.

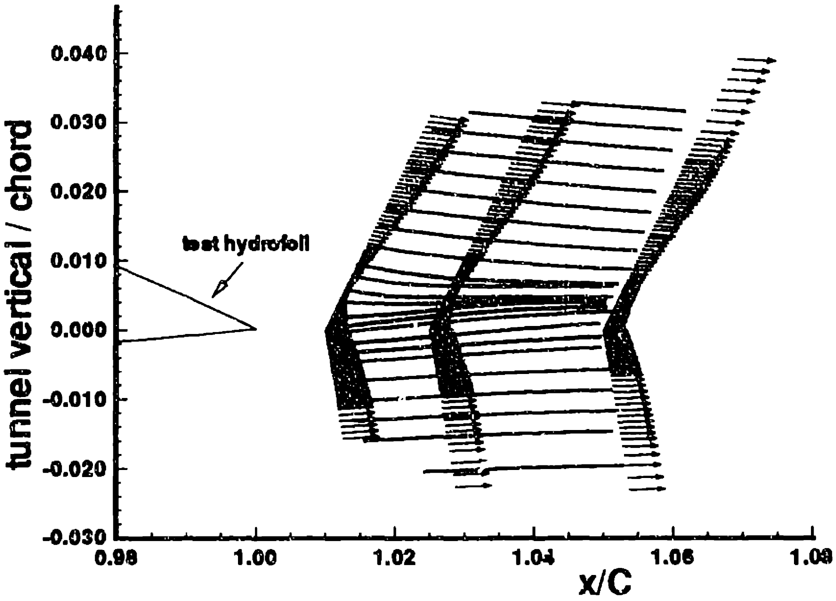

Figure 5-16: Wake streamlines in steady flow

5.4 Comparison with Unsteady Flow Panel Code

Measurements at reduced frequency $k = 3.6$ and Reynolds number $Re = 3.78 \times 10^6$ revealed the presence of a range of harmonic content in surface pressure over the entire chord. Despite the uncertain nature of the source of the higher harmonics, calculations by an unsteady panel code were compared to the measured data. Beyond the predictions of classical thin airfoil theory, panel methods contain the nonlinear effects of thickness.

US2D is a low order potential based panel method [7] that solves in the time domain. The wake geometry is fixed, with a linear distribution of vortex strength in the wake panels. The Kutta condition is imposed by requiring that $\Delta C_p(t) = 0$ across the trailing edge at every time step; that is, the magnitude and phase of the pressure wave are equal above and below the trailing edge. Because US2D does not contain the capability of modelling the tunnel walls, a different hydrofoil geometry must be used. The input foil geometry is one which matches the inviscid pressure distribution as the actual foil geometry has in the water tunnel when at the ideal angle of attack [12]. The magnitude of the input gust to US2D was determined by matching the magnitude of the unsteady part of the calculated and the measured vertical velocity along the upstream face of the bounding box.

The envelope of the mean pressure coefficient $\overline{C_p(t)}$ predicted by US2D is larger than that measured (figure 5-17); this is not surprising since US2D does not model viscous effects. The variation of the magnitude of the first harmonic of $C_p(t)$ over the chord is shown in figure 5-18.

The unsteady panel method does well in tracking the trends of the magnitude of the first harmonic of pressure coefficient, as seen in figures 5-19 and 5-20. But large differences occur in tracking the phase of the pressure wave. Recall that the data has its phase angle referenced to the position of the flappers in their rotation; US2D references phase to the leading edge. In order to reconcile the two, the phase of the vertical velocity just upstream bounding box just in front of the leading edge test hydrofoil was found from the bounding box data. Since the disturbance is a travelling wave, the phase at the leading edge would then be approximately $\phi_{box} + \omega(\Delta x/U_\infty)$, where ω is the rotational frequency of the flapping foils and Δx is the streamwise distance between the location of the measurement and the leading edge. This constant offset was then removed from the experimentally measured phase at the downstream locations. Although this provides only a rough estimate of the offset, the pattern of the phase angle over the chord would only be different by some constant amount.

Instead there is a large variation between measured and predicted phase (figures 5-21 and 5-22). Interestingly, the phase difference at the leading edge between the upper and lower surfaces is almost 180 degrees. On the pressure side, it appears that the phase at the panel before the trailing edge is being forced to match that on the suction side in order to satisfy the Kutta condition.

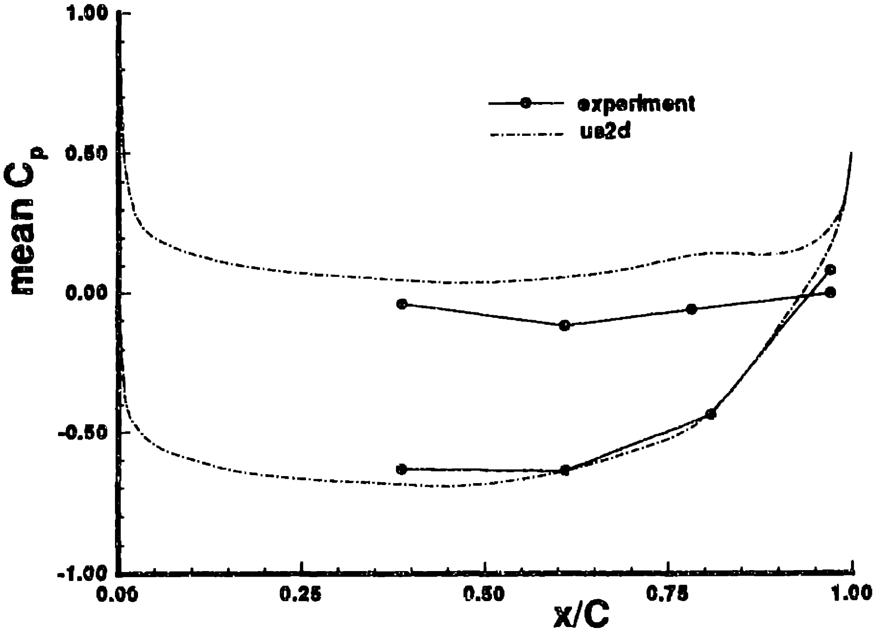

Figure 5-17: Comparison of mean pressure coefficient, experiment vs. US2D

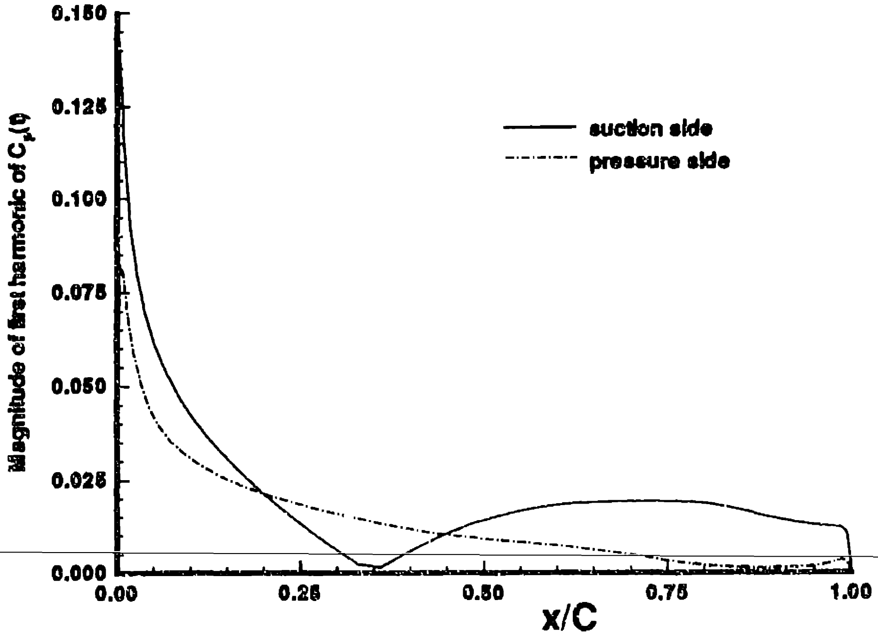

Figure 5-18: Magnitude of first harmonic of $C_p(t)$ vs. x/C, US2D

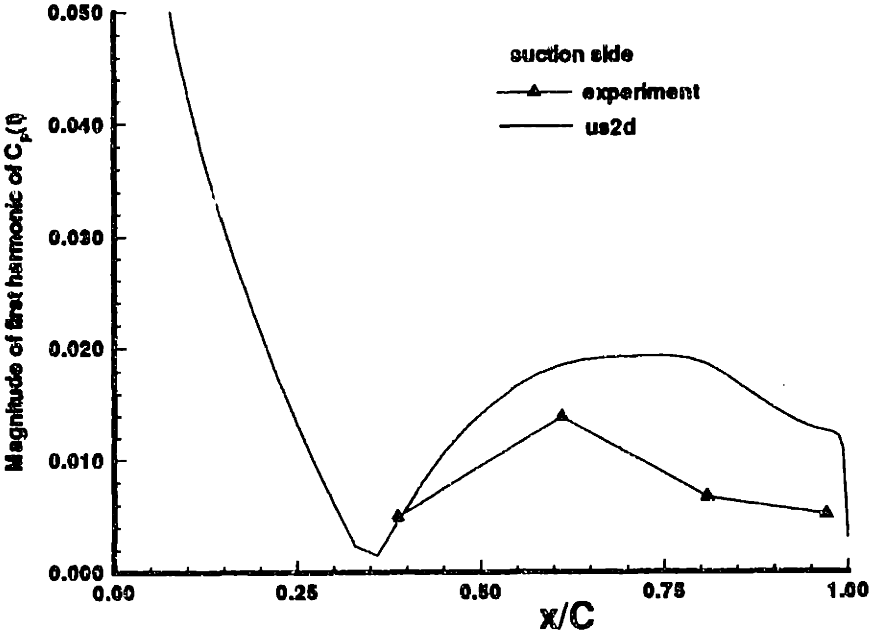

Figure 5-19: Magnitude of first harmonic of $C_p(t)$, experiment vs. US2D

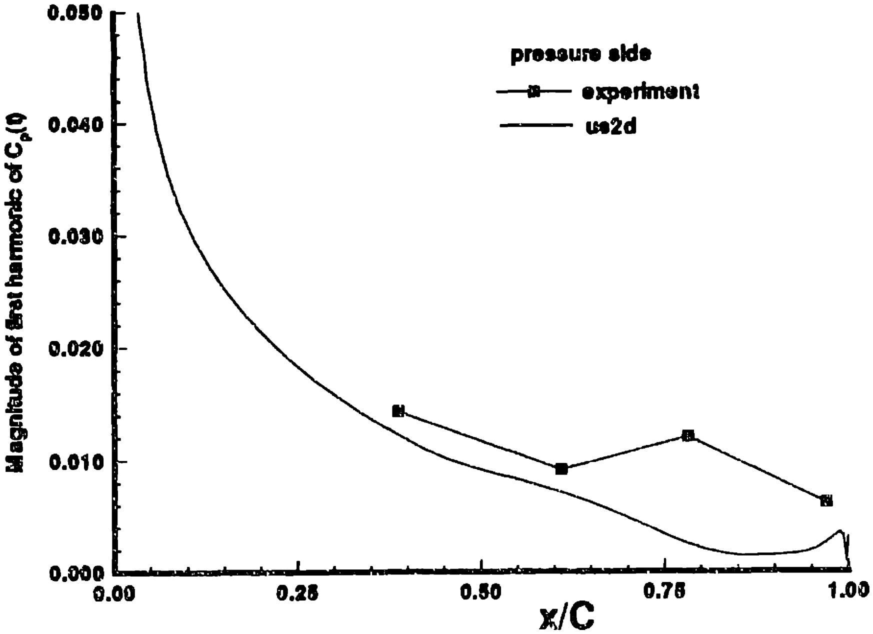

Figure 5-20: Magnitude of first harmonic of $C_p(t)$, experiment vs. US2D

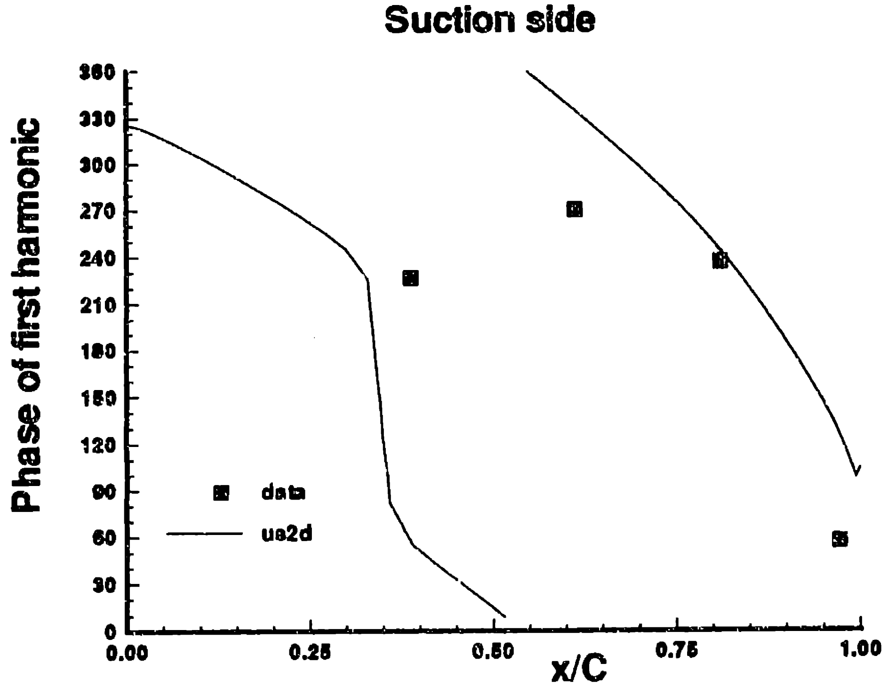

Figure 5-21: Phase of first harmonic of $C_p(t)$, experiment vs. US2D

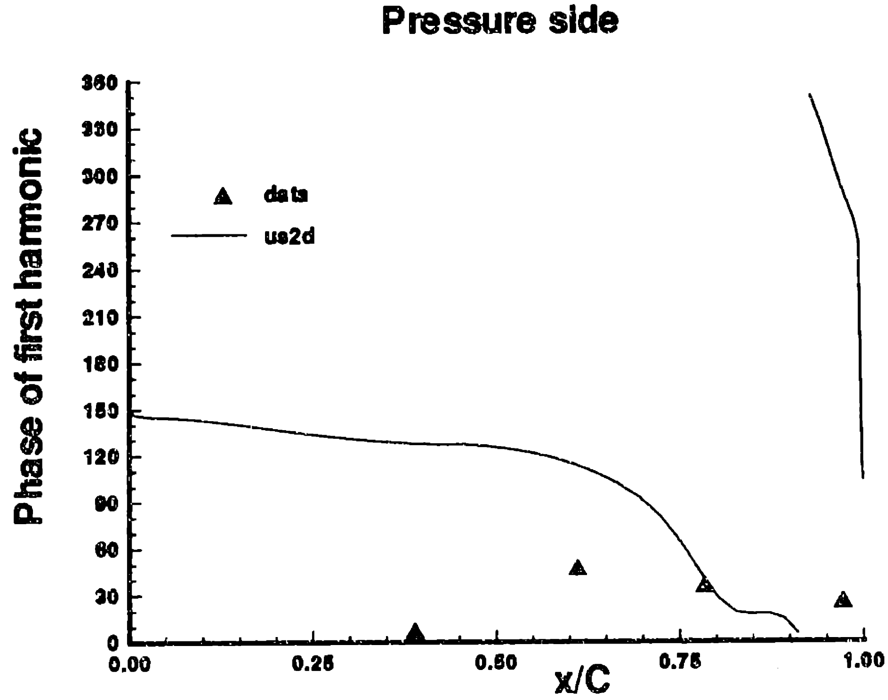

Figure 5-22: Phase of first harmonic of $C_p(t)$, experiment vs. US2D

Chapter 6

Conclusions and Recommendations

6.1 Conclusions

To date the Flapping Foil Experiment has produced highly detailed flow field measurements around an isolated two-dimensional hydrofoil at three operating conditions: steady flow, $Re = 1.36 \times 10^6$; steady flow, $Re = 3.78 \times 10^6$; and unsteady flow, $k = 3.6$, $Re = 3.78 \times 10^6$. The unsteady operating condition had not been previously achieved experimentally.

The steady flow measurements reveal well developed boundary layers over the hydrofoil, with flow separation within the last 5% of the chord on the suction side at both Reynolds numbers. Detailed steady flow wake measurements will provide a base for future unsteady experiments. Lift and drag coefficients were calculated by integrating the velocities measured around a rectangular contour surrounding the hydrofoil. Surface pressures were also measured.

Unsteady flow measurements brought many interesting features to light. The flapping foils create a single harmonic vertical gust along the centerline of the water tunnel of magnitude $v/U_\infty = 0.022$. Throughout the flow field, the velocity contains a mean and a single harmonic, with higher harmonic content an order of magnitude smaller. The boundary layers on the test hydrofoil exhibit a corresponding once-per-flap variation with time. The unsteady part of the boundary layer is convected with the local mean speed; a phase shifting occurs as the gust near the edge of the boundary layer is convected faster than the gust closer to the foil surface. Near the trailing edge on the suction side of the hydrofoil, two decoupled regions develop: the gust in the outer part of the boundary layer has been sheared from the gust in the inner region, with a complete phase reversal and attentuated magnitude between the two. Phase shifting of the gust also occurs close to the hydrofoil surface near the trailing edge on the suction side, where steady flow separation occurs.

In some regions, the standard deviation of velocity in the boundary layer exhibits the same periodic fluctuations as the outer flow. The mean structure of the standard deviation is the same as that in steady flow. The standard deviation does not exhibit the same phase variation through the boundary layer thickness as the unsteady velocity; the unsteady component of the standard deviation is not convected in the same way that the gust velocity is.

Unsteady surface pressure measurements reveal the existence of large harmonic components over the chord. Under suspicion that the source of the higher harmonic is not hydrodynamic, further experimentation was undertaken. For a fixed reduced frequency of $k = 3.6$, it was found that the magnitude of the second harmonic of surface pressure peaked at a flapper frequency around 15 Hz. For this reason the possibility of the flapper exciting a mode of tunnel vibration seems the most likely source of the large harmonic content.

Comparisons between the experimental data and results given by existing computational methods were made. Good agreement was found between steady flow measurements and predicted boundary layer integral quantities by P2D-BLWC, a coupled viscous-inviscid method with wall modelling capabilities. However, P2D-BLWC underpredicts the edge velocity distribution over the hydrofoil, leading to an overestimation of the lift coefficient.

Predictions made by US2D, an unsteady flow panel code, follow the measured trend of the magnitude of the first harmonic of the pressure coefficient over the chord. Large differences exist between the measured and computed phase of the pressure wave over the hydrofoil.

6.2 Recommendations

The experimental data produced to date is a valuable tool for those who develop computational fluid dynamics codes. Future experimentation at this operating condition or at a different combination of reduced frequency and Reynolds number should be undertaken with the following points in mind.

- Computational schemes, implemented at MIT and elsewhere, tend to overpredict the difference pressure coefficient and the lift coefficient. This leads to the question of what the freestream velocity in the water tunnel actually is. The normalizing velocity is measured by a differential pressure cell in the contraction section of the tunnel, while the upstream face of the bounding box shows that a quarter chord in front of the test section, the mean streamwise velocity is 4.4% greater (figure 3-1).

- One of the original goals of the Flapping Foil Experiment was to determine and locate the unsteady streamlines near and at the trailing edge. Due to time constraints, unsteady velocities in the wake have not yet been measured. Before doing so, it would be wise to plan carefully the location of closed paths in order to integrate for the streamfunction, instead of differentiating the velocity field, as was done in steady flow.

- The question of the higher harmonic content of the unsteady surface pressure has not yet been resolved. The pressure transducers should be calibrated while in the test hydrofoil; a dynamic shaker would then shake the entire test section in order to calibrate out the tunnel vibratory response.

Bibliography

[1] R.L. Bisplinghoff, H. Ashley, and R.L. Halfman. *Aeroelasticity*. Addison-Wesley Publishing Co., Reading, MA, 1955.

[2] G.L. Commerford and F.O. Carta. Unsteady aerodynamic response of a two-dimensional airfoil at high reduced frequency. *AIAA Journal*, January 1975.

[3] M. Drela. XFOIL: An analysis and design system for low Reynolds number airfoils. In C.A. Brebbia and S.A. Orszag, editors, *Lecture Notes in Engineering, Volume 54*. Springer-Verlag, 1989.

[4] J.S. Hilten, P.S. Leder, and J. Sethian. A simple hydraulic sinusoindal pressure calibrator. Technical Report 720, National Bureau of Standards, April 1972.

[5] C.M. Ho and S.H. Chen. Unsteady Kutta condition of a plunging airfoil. In R. Michel, J. Cousteix, and R. Houdeville, editors, *Unsteady Turbulent Shear Flows*. Springer, May 1981.

[6] L. Howarth. The theoretical determination of the lift coefficient for a thin elliptic cylinder. *Proceedings of the Royal Society of London*, 149A, 1935.

[7] C.-Y. Hsin. *Development and Analysis of Panel Methods for Propellers in Unsteady Flow.* PhD thesis, Massachusetts Institute of Technology, January 1991.

[8] X.L. Liu, A. Wo, and E.E. Covert. Unsteady streamlines near the trailing edge of NACA 0012 airfoil at Reynolds number of 125,000. *AIAA Journal*, January 1990.

[9] P.F. Lorber and E.E. Covert. Unsteady airfoil pressures produced by periodic disturbances. *AIAA Journal*, September 1981.

[10] J.N. Newman. *Marine Hydrodynamics.* MIT Press, Cambridge, MA, 1976.

[11] D.R. Poling and D.P. Telionis. The response of airfoils to periodic disturbances - the unsteady Kutta condition. *AIAA Journal*, February 1986.

[12] J.Q. Rice. Investigation of a two-dimensional hydrofoil in steady and unsteady flows. Master's thesis, Massachusetts Institute of Technology, June 1991.

[13] R.H. Sabersky, A.J. Acosta, and E.G. Hauptmann. *Fluid Flow: A First Course in Fluid Mechanics.* Macmillan Publishing Co., New York, 1989.

[14] B. Satyanarayana and S. Davis. Experimental studies of unsteady trailing-edge conditions. *AIAA Journal*, February 1978.

[15] J.A. Schetz. *Foundations of Boundary Layer Theory.* Prentice-Hall, Inc., Englewood Cliffs, N.J., 1984.

[16] H. Schlichting. *Boundary-Layer Theory.* McGraw-Hill, New York, 1987.

[17] W.R. Sears. Some aspects of non-stantionary airfoil theory and its practical applications. *Journal of Aeronautical Sciences*, January 1941.

[18] W.R. Sears. Some recent developments in airfoil theory. *Journal of Aeronautical Sciences*, May 1956.

[19] D.P. Telionis. *Viscous Fluid Flow.* Springer-Verlag, New York, 1981.

[20] R.A. Villeneuve. Effects of viscosity on hydrofoil cavitation. Master's thesis, Massachusetts Institute of Technology, June 1993.

[21] F.M. White. *Viscous Fluid Flow.* McGraw-Hill, New York, 1991.